NOTE TO USERS

Modeling Terrain Effects and Application to the Wind Loading of Low Buildings

Kai Wang

A Thesis

in

Department of Building, Civil and Environmental Engineering

Presented in Partial Fulfillment of the Requirements
for the Degree of Doctor of Philosophy at
Concordia University
Montreal, Quebec, Canada

November, 2005

Your file Votre référence
ISBN: 978-0-494-34794-2
Our file Notre référence
ISBN: 978-0-494-34794-2

ABSTRACT

MODELING TERRAIN EFFECTS AND APPLICATION TO THE WIND LOADING OF LOW BUILDINGS

Kai Wang, Ph.D
Concordia University, 2005

Conventional building design wind pressure p can be expressed as a product of the site's reference wind speed pressure q, exposure factor Ce, building pressure coefficient Cp and aerodynamic gust factor Cg. Although the evaluation of Cp and Cg values has progressed significantly in wind engineering, the Ce specifications, especially those for inhomogeneous terrain, were usually given by meteorologists who are mainly interested in predicting higher boundary-layer level winds that sense terrain roughness variations in a scale that may be so large that is not appropriate for building dimensions. Therefore, it is not surprising to see that a number of issues/discrepancies exist in the terrain-related provisions in the wind standards and codes of practice. Most recently, wind engineering studies found that terrain roughness patches of different distance to the site have different strengths of influence, and the building wind loads are very sensitive to small-scale roughness variations as well. Within this context, a systematic study on the development of the terrain exposure factor on building wind loads has been carried out.

Variations of wind speed and turbulence intensity (Iu) profiles, as well as low-rise building loads, above fetch with roughness changes have been investigated by using systematic wind tunnel measurements and numerical simulations (of a set of classic flow-

motion equations with a simple eddy-viscosity closure), with particular attention to the small-scale roughness changes close to the site. The numerical simulation is developed in order to ensure that the present wind-tunnel findings can be better than the standard numerical results that have been adopted into a number of wind standards and codes of practice. The velocity data are formulated into a new speed model and a new *Iu* model, and the low-rise building pressure measurements are analyzed in order to clarify a number of pertinent code issues/discrepancies. The proposed models and design classification have been compared with previous findings, including a limited amount of full-scale data, with satisfactory results. Thereafter, a number of conclusions are made as follows:

- The proposed speed model should be better than, or at least alternative to, the ESDU 82026 model, which has been adopted by the current British, Australian and American wind standards. The shortcoming of the ESDU 82026 model is due to the oversimplified homogeneous terrain assumptions that prevent this model from properly applying for fetch with multiple small-scale roughness changes.
- The proposed *Iu* model is more practical and predictive than the ESDU 84030 standard data sets that belong to the few data provisions for predicting *Iu* profile above inhomogeneous terrain.
- For low-rise buildings, it is found that the Suburban exposure factor should be increased from the ASCE 7-02 specification up close to the ASCE 7-95 level (the former is approximately 25% lower than the latter). In addition, the present results can be used to clarify the discrepancy among different national/international wind

standards and codes of practice on the minimum fetch length requirement for a patch to qualify as homogeneous terrain.

The present research findings will be suggested for updating the terrain-related provisions of the current wind standards and codes of practice.

Acknowledgements

The author wishes to express his sincere gratitude to Dr. T. Stathopoulos for his interest, inspiration and excellent guidance throughout the course of this study, in particular, for his timely encouragement at turbulent periods and for his helpful suggestions in writing.

The author is most grateful to Dr. P.J. Saathoff for his advice throughout the course of this study. Most sincere thanks are due to Mr. J. Zilkha, Mr. J. Hrib and Mr. L. Demers for their help in instrumentation. Most sincere thanks are also due to Mr. S. Bélanger for his timely solution of, and advice on, all computer-related problems and questions encountered by the author in this study.

The author is also indebted to Concordia University for the award of (full-scale) Concordia Graduate Fellowship.

My special thanks are due to Dr. Y. Uematsu, Dr. G. Bitsuamlak and Dr. F. Sadeghpour and for their help and fruitful discussions during the work. Further, I express my sincere thanks to all my friends for their excellent company and cooperation at Concordia University.

I wish to express my special appreciation to my wife Hui for her constant understanding, help and support. A special note of thanks is extended to my parents, sister and brother and all my friends for their help and encouragement throughout my research.

Table of Contents

List of Figures

List of Tables

Nomenclature

c,d	terrain coefficients, used in Eq. (2.42)
C	empirical constant, used in Eq. (2.12)
C_D	drag coefficient (Chapter 2)
Ce	terrain exposure factor
Cp	pressure coefficient
Cp'	pressure coefficient referencing to the mid-roof height velocity pressure above *local* terrain
Cg	aerodynamic gust factor
f	Monin (or similarity) coordinate
f_c	Coriolis parameter
f_{S-R}, f_{R-S}	terrain parameters, used in Eqs. (2.24) – (2.25), (2.27) – (2.30)
g	internal boundary layer total depth
g'	*IBL equilibrium sub-layer depth*
g_o'	gradient height (equivalent to G)
G	gradient height
Ho	average roof level
H	average roughness element height
Iu	turbulence intensity, longitudinal component
$Iu(10)$	longitudinal turbulence intensity at 10 m height
Iv	turbulence intensity, lateral component
k	Karman constant (≈0.4)
K_x	fetch factor accounting for distance of site downstream from sudden change in terrain roughness
L_u^x	integral scale of turbulence
n	frequency
N	total number of a counter
p	pressure

p_o	ambient (static) pressure
$\tilde{p}$	kinematic fluctuating pressure
q	reference speed pressure
$\overline{q^2}$	twice the local turbulent kinetic energy
R	roughness-change parameter, used in Eqs. (2.24) – (2.26) and (2.34)
$S(n)$	energy spectrum
u	fluctuating velocity, longitudinal component
u'	far-upstream (i.e. free stream) fluctuating velocity, longitudinal component
$u*$	surface-shear velocity
U	mean speed, longitudinal direction
$\tilde{U}$	mean speed $\tilde{U}$ outside boundary layer height, used in Eq. (2.3)
$U(G)$	gradient wind speed
w	fluctuating velocity component, vertical direction
W	mean speed, vertical (z) direction
x	patch length, or the length from the upstream end of a patch to the site
X	total patch length
z	vertical elevation, height
z_d	displacement length
z_o	roughness length
$z_{o1,2}$	the greater of z_{o1} and z_{o2}
$z_{o,r}$	the greater one of an upstream patch roughness length, or its adjacent downstream patch roughness length
$z_o^{(i)}$	roughness length at a grid point i along the speed profile 'marching' direction
α	power-law index
β	a parameter used in Eq. (2.26)
ε	rate of energy dissipation
κ	parameter in equation $Iu(z) = \kappa / \ln(z / z_o)$ (Section 2.3.2)

λ	plan area density, i.e., the ratio of plan area of ground obstacles to total ground area containing obstacles
λ_F	frontal area density, i.e. the ratio of frontal area of ground obstacles to total ground area containing obstacles
Ξ	a parameter used in Eqs. (2.27) – (2.30)
ξ	boundary layer parameter, used in Eqs. (2.37) and (2.38)
ρ	air density
σ	parameter of the three-point formula, used in Eq. (4.13)
τ	shear stress
ϕ	building volume ratio, the ratio of the total floor area of a building to the building lot area
ω	circular frequency
τ	turbulence stress
η	a parameter used in Eq. (2.22)
θ	wind attack direction, rotating counter-clock-wisely
Δx	grid length in x direction
Δz	grid length in z direction

Superscript

$\bar{}$	time average.

Subscript

0,1,2,3,4	relate to step changes in terrain roughness from upstream to downstream (note: ESDU convention starts with 1)
F.S.	full-scale
i,j,n	counter
m-rf	middle roof height
ref.	reference height

W.T.	wind tunnel

Abbreviation

ABL	atmospheric boundary layer
BL	boundary layer
ESDU	Engineering Sciences Data Unit
IBL	internal boundary layer
OC	open country
R-S	rough-to-smooth (roughness change)
Rf	roof
RSL	roughness surface layer
S	suburban
S-R	smooth-to-rough (roughness change)
TDMA	TriDiagonal-Matrix Algorithm
U	urban
UTF	upstream terrain factor, the ratio of wind load above local terrain to its counterpart above a reference terrain, typical OC
Wl	wall

Chapter 1 Introduction

1.1 Background

Wind loads, as a form of dynamic structural loads, may cause severe damage to buildings and structures. A rational structural wind-resistance design starts from understanding the global interacting system consisting of the Atmospheric Boundary Layer (ABL), the local wind pattern and the terrain roughness elements, e.g., buildings or structures (Cook 1985). Solar radiation is the source of the energy input into the atmosphere and this generates a global circulation through heating the Earth's surface more at the equator than at the poles. Energy is transferred into the weather systems by instabilities in the global circulation, assisted by the Earth's rotation and by local temperature differences. The wind of weather system is the source of energy that drives ABL that is dragged and perturbed by roughness elements above terrain. Since wind standards and codes of practice are mainly interested in strong winds, neutral stability is assumed for this study, i.e., effects of temperature and buoyancy are not presently considered.

In wind standards and codes of practice, design pressure p can be generally expressed as a product of the site's reference speed pressure q, the terrain exposure factor Ce, building shape (pressure) coefficient Cp and the aerodynamic gust factor Cg, namely,

$$p = qCeCpCg \tag{1.1}$$

Speed profile variation with exposure is essential for the Ce specifications, and turbulence intensity (Iu) profile variation is important for the Cg specifications (cf. ASCE 7-02), where $Iu = u/U(z)$, in which u is the fluctuating component of velocity and $U(z)$ is

the mean component of velocity (i.e. speed) at vertical elevation z. Appropriate modeling of the terrain effects on wind is important for formulation of code terrain-related provisions.

Terrain is presently confined to two-dimensional flat ground. Terrain may be geographically described in terms of the roughness element plan area density λ (or frontal area density λ_F), in which λ (or λ_F) is the ratio of the average roughness element plan area (or wall area) to the total site area per roughness element. Terrain roughness characterizes terrain aerodynamic drag and perturbation property. Homogeneous terrain has uniform roughness, while inhomogeneous terrain has roughness changes and can be broken down into terrain pieces of finite length and homogenous roughness, each of which is called a 'patch'. A patch may be described by three parameters: length, characteristic value of roughness, and distance to the site. Two adjacent patches of different roughness can form a smooth-to-rough (S-R) roughness change that has the smooth patch in upwind position, or a rough-to-smooth (R-S) roughness change that positions the rough patch upwind. Paving patches piecewise from the site to an upwind limit form a fetch. A pertinent fetch is the fetch section beyond which terrain roughness does not have (significant) impact on the wind loads of the building at the site.

Current wind code terrain-related provisions may work well just for simple terrain configurations, which are mainly classified into a few grades, namely, Coastal, Open Country (OC), Suburban-Urban, and/or Large-City-Center. However, terrain in reality usually features a great variety of roughness changes. The inhomogeneous terrain has not been well represented in wind standards and codes of practice.

Wind hazards are still common. It is found that 88% of the total insured property loss from U.S catastrophes during the period of January 1986 to October 1992 resulted from wind storms (Suresh Kumar 1998). Therefore, appropriate modeling of the terrain effects on wind loads should be of great interest.

1.2 The challenges

Although the evaluation of *Cp* and *Cg* values has progressed significantly in wind engineering recently, the *Ce* specifications, especially those for inhomogeneous terrain, remain those mostly developed by meteorologists who are mainly interested in higher (boundary-layer) level winds that sense terrain roughness variations in a scale that may be too large for building scales. Therefore, it is not surprising to see that a number of important issues/discrepancies exist in the code terrain-related provisions. Most recently, wind engineering studies found that terrain patches of different distance to the site have different strengths of influence, and the loads are very sensitive to small-scale roughness changes. These altogether encourage a systematic study on the variation of wind velocity (i.e. speed and *Iu*) and loads above terrain with roughness changes.

1.3 Objectives of this study

The prime objectives of this study are (a) to investigate, by wind tunnel experimentation and/or numerical simulation, the variations of wind speed and *Iu* profiles as well as the low-rise building wind loads above terrain with roughness changes, with particular attention to small-scale roughness changes close to the building, and (b) to formulate the experimental results into appropriate analytical/empirical/descriptive model or design

guideline for better characterization of the wind profiles and loads for design purposes. Development of such representation appears very important for better wind load assessment, and more specifically, the experimental results can be used to tackle the current issues/discrepancies presented in the next chapter.

1.4 Thesis outline

This thesis consists of eight chapters, a list of references and five appendices. Chapter 2 reviews the pertaining classic theories and previous research approaches and findings, and specifies the current issues/discrepancies. Chapter 2 also outlines the research methodology for this study.

Chapter 3 mainly presents the wind tunnel experimentation, namely, the general setting, the data acquisition, the scaling, and the fetch and building modeling. Chapter 3 also introduces the basic pressure presentation and analysis techniques.

Chapter 4 describes the numerical simulation, namely, the flow-motion equations, wall treatments, the control volume method for discretization, and the enhanced Tri-Diagonal Matrix Algorithm (TBMA) for solving the discretized linear equations of variable coefficients.

Chapter 5 proposes the speed model. This chapter describes the model's characteristics and application, then compares this model with the present wind tunnel and numerical results, the ESDU (82026) model, as well as a limited amount of full-scale data.

Chapter 6 proposes an *Iu* model. Similar to the layout of Chapter 5, this chapter first describes the characteristics and application of the proposed *Iu* model, and then compares

this model with the present wind-tunnel data, a ESDU (84030) dataset, and limited full-scale data.

Chapter 7 presents the wind tunnel low-rise building load measurements, and clarifies the pertinent code issues/discrepancies in terms of the minimum fetch length required for a patch to consider as fully developed/matured terrain, and the Suburban/Urban exposure (load-reduction) factor. A set of new specifications are proposed as a result.

Chapter 8 summarizes the findings, contributions of this study, as well as it provides recommendations for future work.

Chapter 2 Literature review

2.1 Overview

Studies on the terrain-wind relationship generally fall into the research category Boundary Layer (BL) theory that generally uses experimental, dimensional analysis and numerical approaches. The experiments have provided empirical correlations (e.g., power law). The dimensional analyses have formed theoretical relationship (e.g., log law) which is usually used as closure to flow-motion equations, or analytical model (cf. Fiedler and Panofsky 1972). Moreover, the numerical simulations have resulted in data that are in turn formed into empirical models (e.g. ESDU 82026).

A huge volume of literature has been found in this research area. The present review will narrow on just a few previous studies whose results fall onto a general procedure for the assessment of terrain effect on building wind loads. More specifically, the research pertaining questions are how to define an upstream fetch, and predict wind profile for a well-defined upstream fetch; in other words, the research topics are related to terrain characterization and wind profile/loading assessment.

Contents in this chapter are organized as follows: Section 2.2 presents the pertinent homogenous rough-wall BL theories, some of which are considered fundamental to the formulation of the current code terrain-related provisions. Section 2.3 presents the previous approaches/findings on speed and *Iu* profile estimations above homogeneous or inhomogeneous terrain. Section 2.4 accounts for the previous results on low-rise building

loading. Section 2.5 evaluates the previous findings to show the current issues. In the end, Section 2.6 proposes the research objectives and approaches of this study.

2.2 Pertinent boundary layer theories

Flow mean-motion equations

The classic *2-D* turbulence mean motion equations in steady condition can be written as,

$$U\frac{\partial U}{\partial x}+W\frac{\partial U}{\partial z}=-\frac{\partial p}{\partial x}+\frac{\partial \tau}{\partial z} \quad \text{(momentum)} \tag{2.1}$$

$$\frac{\partial U}{\partial x}+\frac{\partial W}{\partial z}=0 \quad \text{(continuity)} \tag{2.2}$$

where U, W are the mean velocities on the x (streamwise) and z (vertical) directions, respectively; p is pressure; $\tau = -\overline{uw}$ is turbulence shear stress, where u and w are the fluctuating velocity components on x and z directions, respectively, and the bar '-' denotes time-average. The laminar component of shear stress is much less than the turbulent component so that is not reflected in the equations. Prantl BL assumption (Wu 1983) says that streamwise pressure gradient is the same across the BL, and outside BL has the form,

$$\tilde{U}\frac{\partial \tilde{U}}{\partial x}=-\frac{\partial p}{\partial x} \tag{2.3}$$

It is assumed that the mean speed $\tilde{U}$ is constant across the BL, thus $\partial \tilde{U}/\partial x = 0$, both left-hand side and right-hand side of Eq. (2.3) are zero, so that the first term of the right-hand-side of Eq. (2.1) can be dropped off.

Turbulence statistics

Wind fluctuations may be considered to be caused by a superposition of (conceptual) eddies, each characterized by a periodic motion of circular frequency $\omega = 2\pi n$, where n denotes frequency (Simiu and Scanlan 1996). The total kinetic energy of the turbulent motion may correspondingly be regarded as a sum of contributions by each of the flow eddies. The function $S(n)$ representing the dependence of these energy contributions upon wave number is defined as the energy spectrum of the turbulent motion.

If the equations of motion of the turbulent flow (see Eqs. (2.1) and (2.2)) are suitably transformed, it can be shown that the inertia terms in these equations are associated with transfer of energy from larger eddies to small ones, while the viscous terms account for energy dissipation. The latter is affected mostly by the smallest eddies in which the shear deforms, and therefore the viscous stresses are large. In the absence of source of energy, the kinetic energy of the turbulent motion will decrease, i.e. the turbulence will decay, faster if the viscosity effects are large, more slowly if these effects are small. More precisely, in the latter case the decay time is long if compared to the periods of the eddies in the high wave number range. If the energy fed into them through inertial transfer from the larger eddies is balanced by the energy dissipated through viscous effects, the energy of these eddies may therefore be considered steady. The small eddy motion is then determined solely by the rate of energy transfer (or equivalently by the rate of energy dissipation ε, as denoted) and by viscosity. This is the so-called Kolmogorov's first hypothesis. It follows this assumption that, since small eddy motion is solely dependent upon internal parameters of the flow, it is independent of external conditions such as

boundaries and that, therefore, local isotropy – the absence of preferred directions of small eddy motion – occurs (Simiu and Scanlan 1996).

It may be further assumed that the energy dissipation is produced almost in its entirety by the very smallest eddies of the flow. Thus, at the lower end of the higher frequency range to which Kolmogorov's first hypothesis applies, the influence of the viscosity is small. In this inertial subrange, the eddy motion may be assumed to be independent of viscosity and thus determined solely by the rate of energy transfer (which, in turn, is equal to the rate of energy dissipation.) This is called the Kolmogorov's second hypothesis (Simiu and Scanlan 1996).

Raupach et al (1991) summarize this classic theory as two hypotheses: equilibrium layer hypothesis and wall similarity hypothesis. Equilibrium layer hypothesis says: in inner layer the local rates of turbulent kinetic energy production and dissipation are so large that some aspects of the turbulent motion concerned with these processes are independent of conditions elsewhere in the flow. Wall similarity hypothesis says: outside Roughness Surface Layer (RSL), the turbulent motions in BL must be independent of wall roughness and the viscosity, except for the role of the wall in setting shear velocity u_*, displacement length z_d and the BL thickness G.

Raupach et al (1991) showed that, if the two-dimensional time-average turbulent motion equation is properly transformed, it gives the turbulence kinetic energy budget,

$$U\frac{\partial \overline{q^2}/2}{\partial x}+W\frac{\partial \overline{q^2}/2}{\partial z}=\tau\frac{\partial U}{\partial z}-\frac{\partial(\overline{wq^2}/2)}{\partial z}-\frac{\partial \overline{w\tilde{p}}}{\partial z}-\varepsilon \qquad (2.4)$$

where w is the vertical (z-direction) fluctuating velocity, $\overline{q^2} = \overline{u^2} + \overline{w^2}$ is twice the local turbulent kinetic energy, $\tilde{p}$ is the kinematic fluctuating pressure, and ε is the average energy dissipation rate.

Eq. (2.4) may be reduced to,

$$\tau \frac{\partial U}{\partial z} - \varepsilon = 0 \tag{2.5}$$

and associated with Eq. (2.5), there may come,

$$\partial U / \partial z = u_* / \kappa z \tag{2.6}$$
$$\tau = u_*^2 \tag{2.7}$$
$$\varepsilon = u_*^3 / \kappa z \tag{2.8}$$

The derivation of Eqs. (2.5) – (2.8) is explained as follows. The equilibrium layer hypothesis implies three specific conditions. The first is that local equilibrium occurs when the advection terms (on the left-hand side of Eq. (2.4)) and transport terms (the second and third on the right-hand side of Eq. (2.4)) are negligible in comparison with local shear production and dissipation (the first and fourth terms on the right-hand side of Eq. (2.4)); this condition enables the reduction of Eq. (2.4) into Eq. (2.5). The second condition for an equilibrium layer is that the layer must be thin and independent of large-scale flow geometry. The third is that the shear stress variation across the layer must be small, to ensure stress be unimportant. This wall similarity hypothesis implies that detailed geometries of surface roughness elements are irrelevant. The second and third conditions of the equilibrium layer hypothesis and the wall similarity hypothesis enable the dimensional analysis that gives Eqs. (2.6) – (2.8) (Raupach et al 1991).

From Kolmogorov's second hypothesis (Simiu and Scanlan 1996), it follows that a relation involving $S(n)$ and ε holds for sufficiently high n:

$$F[S(n), n, \varepsilon] = 0 \tag{2.9}$$

The dimensions of the quantities within the brackets in Eq. (2.9) are $[L^3T^{-2}]$, $[T^{-1}]$ and $[L^2T^{-3}]$, respectively. Dimensional considerations with measurement results will show,

$$S(n) = 0.5\varepsilon^{2/3}n^{-5/3} \tag{2.10}$$

Taking $\varepsilon = \frac{u_*^3}{kz}$ into Eq. (2.10), and assuming

$$K = \frac{2\pi n}{U(z)}$$

it follows that

$$\frac{nS(n)}{u_*^2} = 0.26f^{-2/3} \tag{2.11}$$

where the non-dimensional quantity

$$f = \frac{nz}{U(z)}$$

is known as the Monin (or similarity) coordinate (Simiu and Scanlan 1996).

For low-frequency (called inactive) range, the above universal relation does not exist. The u-component spectra are proportional to n^{-1}. Between the low-frequency range and the inertial subrange, there is an overlap (called active) range, which cannot be described by a universal relation (Raupach et al 1991). The spectral models for engineering purposes are usually designed to represent the entire spectrum (Simiu and Scanlan 1996; Richards et al 2000). Furthermore, since the energy spectrum $S(n)$ shows the energy (power) of a velocity fluctuation at different frequencies n, the energy spectrum is oftentimes called the power spectral density in wind engineering practice.

The above shows that some turbulence closures for the motion equations are

established upon the homogeneous terrain/wall assumptions; however, these assumptions have been found also hidden in the code terrain-related provisions for inhomogeneous terrain. Recent studies have found that this assumption may be oversimplified for assessing wind profile/loading at a scale suitable for buildings.

2.3 Modeling of BL profiles above fetch with roughness changes

2.3.1 Considerations of large-scale roughness changes

Most of the current modeling efforts are found initiated in meteorological area that are mainly interested in high level BL winds that generally sense large-scale terrain variations. Presently, the terrain 'large-scale' implies that a terrain can be evaluated into grids of dimension of the order of 1 km. As a typical example, Wieringa (1986) considered a terrain-grid of 5×5 km^2 appropriate for estimating 60 m level BL wind.

Several subgrid roughness changes may occur in a terrain grid of dimension of order of 1 km; therefore, roughness changes considered in such a dimension may need to be treated by a grid average (i.e. roughness homogenization). A number of averaging methods (see review in Grimmond and Oke 1999) have been developed; some were formulated upon numerical results (e.g., Taylor 1987; Mason 1988), and the others are mainly empirical fittings of experimental data (e.g. Lettau 1969; Counihan 1971; Kondo and Yamazawa 1986; MacDonald et al 1998). The model of Lettau (1969), which has been discussed by Wieringa (1993), and Petersen (1997), is one of the few models derived from full-scale data; it has the form,

$$z_o = CH\lambda_F \tag{2.12}$$

where H is the grid-average roughness element height, and λ_F is the frontal area density, and C is a constant suggested as 0.5 by Lettau (1969), and as equal to 1 by Sill and Fang (1990) following their wind tunnel tests.

Modeling of the BL profile variation starts above homogeneous terrain of low-roughness. As illustrated by Fig. 2.1, the BL, starting from ground up to the boundary layer gradient height G, may be subdivided into 3 major layers: RSL, surface layer and outer layer, each of which has a set of unique scaling parameters. For homogenous fetch of low-roughness, the RSL may be neglected for its unnoticeable depth. Power law and log law are regarded as the successful models; therefore, the corresponding power-law index α, and/or log-law roughness length z_o, were widely used as the characteristic value of roughness.

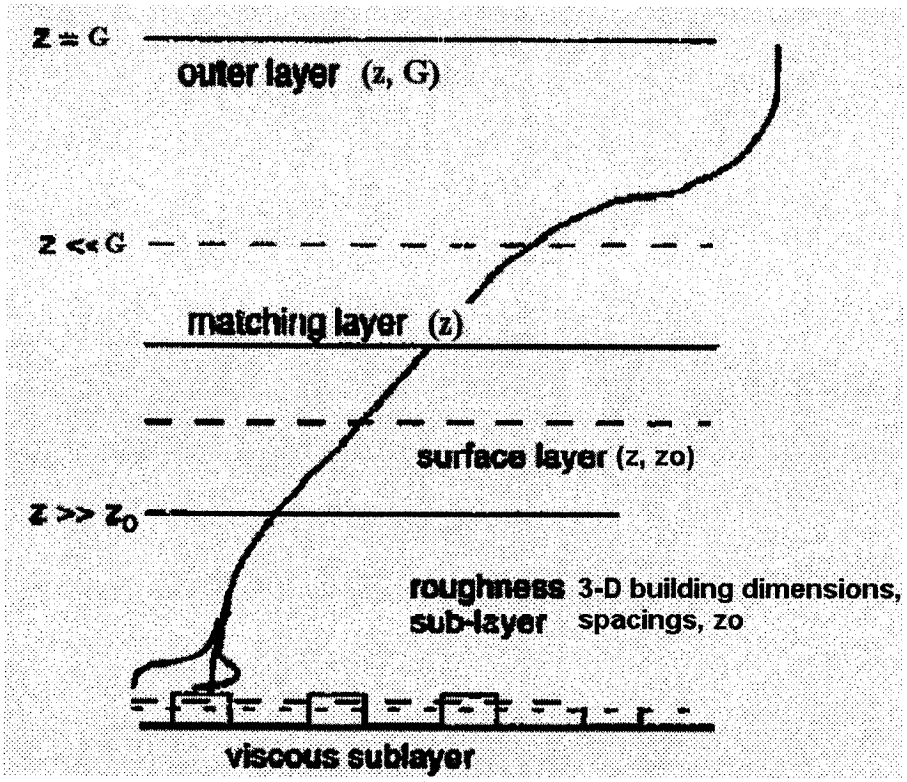

Fig. 2.1. BL structure in a wind tunnel simulation (adapted from Bottema 1996).

Above homogeneous terrain of high roughness, such as certain built-up region, the RSL may grow up with thickness greater than 2 building heights (Bottema 1996). Above the RSL, the power law or log law are assumed effective. Within the RSL, no successful model has been made, although few models (e.g., MacDonald 2000) maybe applicable for idealized laboratory conditions.

Homogeneous terrain was classified into a number of roughness grades. After the review work of Wieringa (1992 and 1993), Davenport et al. (2000) proposed an eight-grade classification as presented in Table 2.1. On the other hand, current wind standards and codes of practice (e.g. NBCC 1995; ASCE 7-02) simply classify homogeneous terrain into fewer grades.

Table 2.1. Davenport terrain classification scheme (Davenport et al. 2000).

Roughness	z_0 (m)	Terrain description
1. Sea	0.0002	open water, tidal flat, snow with terrain above several km
2. Smooth	0.005	featureless land, ice
3. Open	0.03	flat terrain with grass or very low vegetation, airport runway, ice with ridges across-wind
4. Roughly open	0.1	Cultivated area, low crops, obstacles of height *H* separated by at least 20 *H*.
5. Rough	0.25	high crops or crops of varying height, scattered shelter belts, obstacles separated by 8 – 12 *H* of low solid objects
6. Very rough	0.5	large obstacle groups (farms, clumps of forest) separated by 8 object *H*, low buildings with interspaces 3-7 building *H* & no high trees
7. Closed	1	Mature regular forests, densely built-up area without much building height variation
8. Chaotic	Over 2	City centre with mixture of low and high buildings, large forest of irregular height with many clearings

Above the fetch with a single roughness change, the BL may be viewed as stratified into an upper layer and an Internal Boundary Layer (IBL), divided by the IBL depth (g). Flow property under g is regarded as adapted with the patch after the roughness change (Garratt 1990). There may be a transitional layer just on top of the IBL, in which the

segment of the BL profile shows deformations (i.e. transitional feature), as shown in Fig. 2.2.

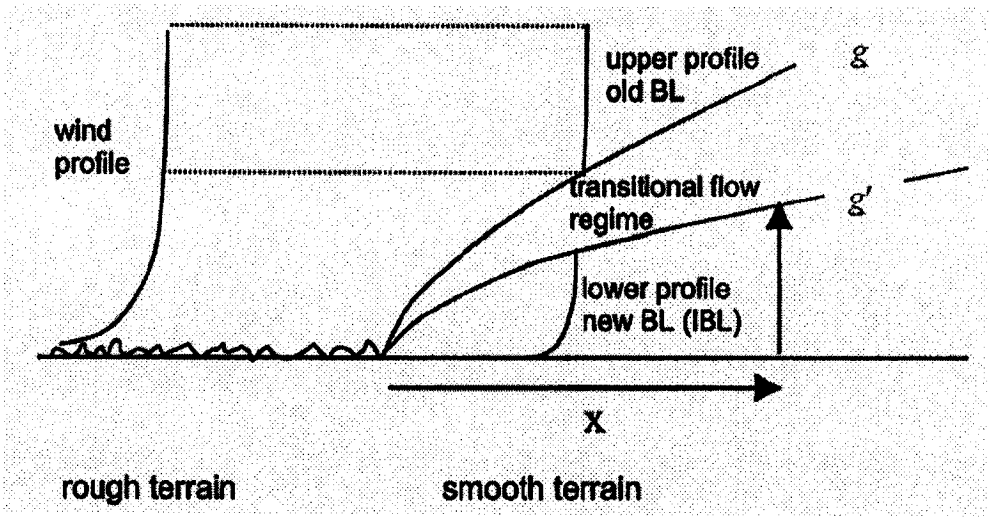

Fig. 2.2. Schematic IBL above fetch with an R-S change (after Letchford et al 2001).

IBL theories have been reviewed by Garratt (1990), where a number of findings on the IBL variation with fetch length are of interest and presented as follows. One of the models is,

$$g(x) \propto z_{o,r}^{0.2} x^{0.8} \tag{2.13}$$

where $z_{o1,2}$ is the greater of z_{o1} and z_{o2} and x is the fetch length from the roughness change to the site. Another is suggested by Antonia and Luxton (1971, 1972), that is, after S-R roughness change,

$$g(x) \propto x^{0.79} \tag{2.14}$$

and after R-S roughness change,

$$g(x) \propto x^{0.43}. \tag{2.15}$$

Previous studies have given findings on the variation of shear stress τ ($= u_*^2$) with fetch length (x). For instance, Bradley (1968) found that $\tau \propto x^{-0.2}$ (i.e. $u_* \propto x^{-0.1}$) after an S-R roughness change, and Garratt (1990) quantified that the shear stress initially increases to about twice the final value for an S-R roughness change, and the initial shear stress decreases to about half of the final value after an R-S change. Altogether those findings will be used in Chapter 4 in this study.

2.3.2 Models for engineering application

Homogeneous terrain speed, Iu model of log-law form

The log law speed model was proposed by using matching-theory (cf. Wieringa 1986) for homogeneous terrain. The log law assumes a mixing length correlation and can be derived from Eq. (2.6). Applicable for homogeneous smooth terrain, the log law has the form,

$$U(z) = \frac{u_*}{k} \ln(z / z_o) \tag{2.16}$$

Eq. (2.16) is often modified to be,

$$U(z) = \frac{u_*}{k} \ln \frac{z - z_d}{z_o} \tag{2.17}$$

where u_* is the surface-shear velocity; the universal Karman constant $k = u_* / (z(dU / dz))$ is approximately equal to 0.4 independent of roughness (see Raupach et al 1991); and the displacement length z_d - an empirical modification factor - is regarded as loosely correlated with z_o (Grimmond and Oke 1999).

Log law has been used as a closure to the turbulent flow motion equations, and was therefore regarded as a 'theoretical' equation, since it correlates the turbulence stress τ

($=u_*^2$) with mean speed U; however, the log law essentially comes from simplified assumptions.

Cook (1997) considered that the log law meets the lower boundary conditions, but has no upper boundary. Simiu and Scanlan (1996) considered that the log law is well applicable from ground up to about 100 m (for homogeneous terrain of low roughness).

For calculating *Iu* profile above homogeneous terrain of different roughness, Simiu and Scanlan (1996) provided the empirical equation $Iu(z) = \kappa / \ln(z/z_o)$, where the parameter κ= 1.0, 0.92 and 0.88, for z_o = 0.005, 0.30 and 1 m, respectively.

ESDU models for speed and/or Iu profiles

Full-scale study of Deaves and Harris (1978), and the numerical studies of Deaves (1981a and 1981b) which provided solutions to the flow-motion equations with simple eddy-viscosity closure above inhomogeneous roughness, resulted in the ESDU (family) models. Results of Deaves and Harris (1978) on equilibrium speed and *Iu* profiles were formulated into a component of the ESDU (82026) model for homogeneous roughness, as such the component is called the ESDU (82026) equilibrium model for convenience. Results of Deaves (1981a) were formulated into another component of the ESDU (82026) model for inhomogeneous roughness speed profile estimation, thus the component is called the ESDU (82026) transitional model. Results of Deaves (1981b) regressed into the ESDU (84030) datasets. The ESDU (82026) model was subsequently adopted into several wind standards and codes of practice, such as the British, and the Australian standards (Cook 1997), as well as ASCE 7-02. It should be noted that a track back into the numerical studies of Deaves (1981a and 1981b) reveals that the homogeneous terrain

assumptions (see Section 2.1) have been hidden in the results applied for inhomogeneous terrain.

Different from the two-parameter log law, the ESDU (82026) equilibrium (speed and *Iu*) model mainly has three scaling parameters, z_o, u_*, and G (gradient height), i.e.

$$\frac{U(z)}{u_*} = 2.5\left[\ln\left(\frac{z}{z_o}\right) + \frac{23}{4}\frac{z}{G} - \frac{15}{8}\left(\frac{z}{G}\right)^2 - \frac{4}{3}\left(\frac{z}{G}\right)^3 + \frac{1}{3}\left(\frac{z}{G}\right)^4\right] \tag{2.18}$$

which is valid up to G,

$$G = \frac{u_*}{6f_c} \tag{2.19}$$

where f_c is the Coriolis parameter depending on earth's self rotation and latitude. Eq. (2.18) can be simplified for speed profile up to 300 m as,

$$\frac{U(z)}{u_*} = 2.5\left[\ln\left(\frac{z}{z_o}\right) + \frac{34.5 f_c z}{u_*}\right] \tag{2.20}$$

and

$$I_u = \frac{u(z)}{U(z)} = \frac{u(z)}{u_*}\frac{u_*}{U(z)} \tag{2.21}$$

where u is the fluctuating velocity, and

$$\frac{u(z)}{u_*} = \frac{7.5\eta[0.538 + 0.09\ln(z/z_o)]^{\eta^{16}}}{1 + 0.156\ln(u_*/(f_c z_o))} \tag{2.22}$$

where $\eta = 1 - 6f_c z/u_*$ (2.23)

The ESDU (82026) equilibrium model, Eqs. (2.21) – (2.23), recognizes the gradient height G so that enables the translation of speed profiles among various terrain circumstances. This model is not a single curve but a family of curves depending on the wind speed (Cook 1997).

The ESDU (82026) transitional model is built upon the ESDU (82026) equilibrium model. For fetch with a single roughness change, the ESDU (82026) transitional model has the following calculation procedure (see Fig. 2.3):

a) estimate patch roughness lengths z_{o1} and z_{o2}, and friction velocities u_{*1} and u_{*2}.

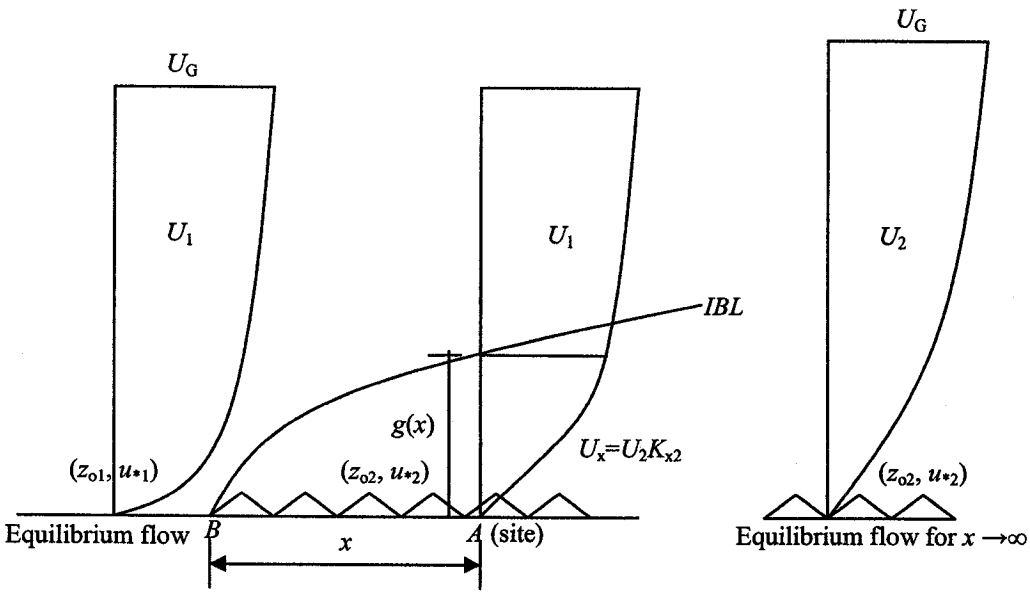

Fig. 2.3. Schematic of the ESDU (82026) transitional model application procedure for a fetch with a single roughness change.

b) calculate the equilibrium speed profiles $U_1(z)$ and $U_2(z)$ respective to patch (z_{o1} and u_{*1}) and patch (z_{o2} and u_{*2}).

c) estimate a terrain dependent coefficient K_{x2} by,

$$K_{x2} = 1 + 0.67R^{0.85} f_{S-R} \qquad \text{(S-R)} \qquad (2.24)$$

$$K_{x2} = 1 - 0.41Rf_{R-S} \qquad \text{(R-S)} \qquad (2.25)$$

$$R = \frac{\left|\ln(z_{o1}/z_{o2})\right|}{\left[u_*/(fz_o)\right]_2^{\beta}} \qquad (2.26)$$

where $\beta = 0.23$ and 0.14 for S-R and R-S roughness change respectively, and

$$f_{S-R} = 0.1143\Xi^2 - 1.372\Xi + 4.087 \qquad \text{(for } \Xi \leq 5.5\text{)} \qquad (2.27)$$

$$f_{S-R} = 0 \qquad \text{(for } \Xi > 5.5\text{)} \qquad (2.28)$$

$$f_{R-S} = 0.0192\Xi^2 - 0.550\Xi + 2.477 \quad (\text{for } \Xi \leq 5.6) \tag{2.29}$$

$$f_{R-S} = 0 \quad (\text{for } \Xi > 5.6) \tag{2.30}$$

where $\Xi = \log_{10} x$ meters.

d) estimate the IBL depth $g(x)$ by the continuity requirement, i.e. $K_{x2}U_1(z) = U_2(z)$; thus,

$$K_{x2}[2.5u_{*2}\ln(g/z_{o2})] \approx 2.5u_{*1}\ln(g/z_{o1}) \tag{2.31}$$

$$g(x) = \exp\left[\frac{K_{x2}(u_{*2}/u_{*1})\ln z_{o2} - \ln z_{o1}}{K_{x2}(u_{*2}/u_{*1}) - 1}\right] \tag{2.32}$$

In fact, the above continuity requirement implies that one can tailor two profiles into a continuous one instead of using Eqs. (2.31) and (2.32).

e) use K_x factor to correct the equilibrium profile with respect to the *IBL*.

The ESDU (82026) procedure for a fetch with three roughness changes is illustrated in Fig. 2.4 and described as follows (in fact that same principle is applicable for fetch with any number of roughness changes).

Speed profile over site (A) would be given by,

$$U(z) = U_1(z) \qquad g_1 \leq z \leq G \tag{2.33a}$$

$$U(z) = K_{x2}U_2(z) \qquad g_2 \leq z \leq g_1 \tag{2.33b}$$

$$U(z) = K_{x2}K_{x3}U_3(z) \qquad g_3 \leq z \leq g_2 \tag{2.33c}$$

$$U(z) = K_{x2}K_{x3}K_{x4}U_4(z) \qquad z \leq g_3 \tag{2.33d}$$

where U_1, U_2, U_3 and U_4 are the mean speed profiles in idealized equilibrium conditions of the patches of roughness z_{o1}, z_{o2}, z_{o3} and z_{o4}, respectively. For a roughness change $z_{o,j-1}$ to $z_{o,j}$, where patch counter j starts from 2, the value of $K_{x,j}$ is calculated using Eqs. (2.24) – (2.33) with,

$$R_j = \frac{\left|\ln(z_{o,j-1}/z_{o,j})\right|}{[u_*/(fz_o)]_j^{\beta}} \tag{2.34}$$

$$x = x_2 + x_3 + \cdots + x_j \tag{2.35}$$

The patch-respective curves can be also tailored into a continuous one by the continuity principle.

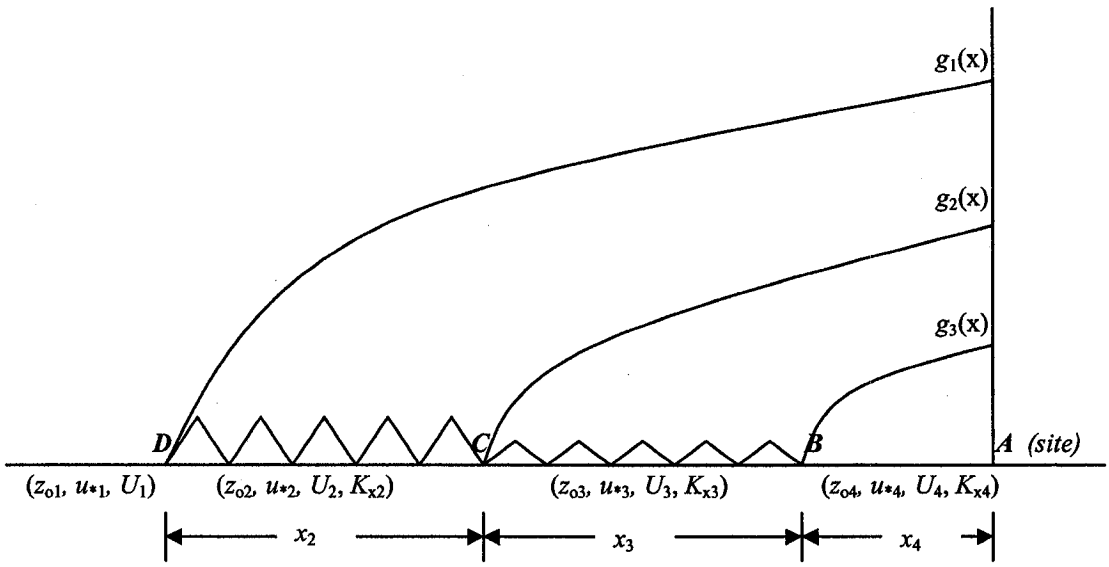

Fig. 2.4. Schematic IBL inputs for the ESDU (82026) transitional model for a terrain with three roughness changes.

Theoretically, the ESDU (82026) model can predict speed profile for inhomogeneous terrain with any number of roughness changes. Practically, ESDU (82026) says that "this procedure (ESDU 82026) can obviously be extended to even more roughness changes but it is unlikely that more than three roughness changes will be considered". This implies that ESDU (82026) was mainly developed considering terrain of simple roughness changes. In addition, the ESDU (82026) model may lack sufficient experimental validation (cf. Letchford et al. 2001).

ESDU (84030) provides transitional *Iu* datasets for typical inhomogeneous fetch cases. ESDU (84030) datasets mainly came from the results of Deaves (1981b) who presented the following equations,

$$I_u(x) = \frac{u(x)}{u}\frac{u}{u_*}\frac{u_*}{U(z)}\frac{U(z)}{U(z,x)} \tag{2.36}$$

where $\frac{u(x)}{u}$ is estimated by,

$$\frac{u-u(x)}{u-u'} = \cos^2\left[\frac{\pi}{4}\left(\frac{\xi-0.25}{0.8}\right)\right] \quad (0.25\leq\xi\leq1.85) \qquad \text{for S-R} \tag{2.37}$$

$$\frac{u-u(x)}{u-u'} = \cos^2\left[\frac{\pi}{4}\left(\frac{\xi-0.1}{0.8}\right)\right] \quad (0.1\leq\xi\leq1.7) \qquad \text{for R-S} \tag{2.38}$$

where u', u and $u(x)$ are the upwind, far-downwind and local values of the fluctuating velocities, and x is the fetch length from the roughness change to the site.

$$\xi = \frac{\ln x - \ln g'}{\ln g - \ln g'}$$

$$\frac{g'}{z_{o1,2}} = \left(\frac{z}{10z_{o1,2}}\right)^{5/3}$$

$$g/z_{o2} = (z/0.36z_{o2})^{4/3} \qquad \text{for S-R} \tag{2.39}$$

$$g/z_{o2} = (z_{o1}/z_{o2})(z/0.07z_{o2}) \qquad \text{for R-S} \tag{2.40}$$

where z_{o1} and z_{o2} are respective to the upwind and downwind patches, and $z_{o1,2}$ equal to z_{o1} or z_{o2}, whichever is greater; g and g' are the IBL and the equilibrium sub-layer heights, respectively (see Fig. 2.2); $\frac{u}{u_*}$ is from Eq. (2.22); $\frac{U(z)}{u_*}$ and $\frac{U(z,x)}{U(z)}$ are the outputs of the ESDU (82026) transitional model.

Homogeneous terrain power-law speed and Iu models

For estimation of speed profile in equilibrium with homogeneous terrain, power law was proposed by Hellman (Simiu and Scanlan 1996). Power law uses two independent parameters, the reference speed U_{ref} and the power law index α,

$$\frac{U(z)}{U_{ref}} = \left(\frac{z}{z_{ref}}\right)^{\alpha} \tag{2.41}$$

where U_{ref} is the mean wind speed at reference height, typically 10 m or *G.* Cook (1997) said that the power law remains a good model for the mean speed profile for the range $30 < z < 300$ (m) and compares well with ESDU (82026) equilibrium model for this range. Both NBCC-1995 and ASCE 7-02 adopt the power law for homogenous terrain. Power law may take different α values depending on wind strength (see Tamura 2001b; Farrugia 2003).

The power law is empirical and easy to use, and seems to be working well. Although Cook (1997) said that the power law may not work well for wind speeds at close-to-ground levels, these levels should fall actually into the RSL, an area where no model has been made working well. Moreover, full-scale findings by Tamura et al (2001b) showed that the power law works well for suburban/urban environment, where the majority of low-rise buildings reside (Ho 1992).

Power law has not been considered applicable for inhomogeneous terrain.

Zhou and Kareem (2002) reviewed the inverse power-law *Iu* model of ASCE 7-98 (the same as ASCE 7-02), and some current or early editions of national building codes into the generic form,

$$Iu(z) = c\left(\frac{z}{10}\right)^{-d} \tag{2.42}$$

where *c* and *d* are terrain dependent coefficients, which are summarized in Table 2.2.

Table 2.2. *Iu* profile parameters for Eq. (2.42) (Zhou and Kareem 2002).

ASCE 7-98 (Zhou and Kareem 2002)					SAA (Zhou and Kareem 2002)			AIJ (1996)		
	ASCE 7-98		Zhou and Kareem (2002)							
Terrain α	c	d	c	d	Terrain α	c	d	Terrain α	c	d
0.33	0.45	0.17	0.45	0.33	0.28	0.42	0.28	0.35	0.40	0.40
0.25	0.30	0.17	0.30	0.25	0.20	0.24	0.20	0.27	0.36	0.32
0.15	0.20	0.17	0.20	0.15	0.16	0.18	0.16	0.20	0.26	0.25
0.11	0.15	0.17	0.15	0.11	0.13	0.16	0.13	0.15	0.20	0.20
								0.10	0.16	0.15

2.3.3 Minimum fetch length pertinent to wind loading

Some of the most recent studies (Schmid and Bunzli 1995; Zhang and Zhang 2001) found that local, small-scale roughness changes are more important for winds at the scale of building height. The term 'local' implies that the patch distance to site should be considered a factor for building wind load estimation, and the term 'small-scale' stands for a terrain dimension of the order of 100 meters.

A limited fetch length has been found pertinent to the site of interest. Regarding the effect of roughness on wind speed, Zhang and Zhang (2001) suggested that roughness changes have significant effects if within a fetch length of 2 km. Tamura et al (2001b) found the pertinent fetch length in the order of 1 km. AS/NZS (1170.2 2002) suggests that a fetch of 1 to 4 km (depending on the building height) is considered significant. For lower buildings (height < 50 m), a 1 km upstream fetch may be adequate for exposure evaluation. Regarding *Iu* profile, Letchford et al (2001) pointed out that wind turbulence takes a shorter fetch to 'forget' the upwind patch influence than does mean wind speed.

Small-scale roughness variation has been found significant to the loading estimation. Schmid and Bunzli (1995) indicated that overlooking the subgrid roughness inhomogeneity can lead to significant error. Zhang and Zhang (2001) found that small-

scale roughness changes closer to the site have stronger impacts and suggested to evaluate terrain with a grid of 500×500 m^2.

2.3.4 Full-scale findings

Full-scale findings are considered of 'classic' values and can be used as 'ruler' for engineering model validation. Full-scale speed data include those from Bradley (1968) and Tamura et al (2001a, 2001b), as well as Letchford et al (2001). Full-scale equilibrium *Iu* data can be found in Kato et al (1992), Cermak and Cochran (1992), Tieleman (1996), Schroeder et al (1998) and Baker (2004). Limited spectral findings were given in Panofsky et al (1992).

Bradley (1968) measured the speed profile for an S-R roughness change case (with downwind patch length limited within 26 m) and two R-S roughness change cases (with downwind patch length limited within 250 m), in which the test heights were all limited within the lowest 3 m BL level above ground.

Tamura et al (2001b) simultaneously measured the speed profiles at an upwind and a downwind site in three independent projects; some findings of that study have already been mentioned, and some more detailed descriptions are given herein. The fetch details shown in Fig. 2.5 are further explained as follows. Project 1 saw wind travel 8 km from a seaside ("Seaside-1") to a residential area ("Res-1"). Project 2 saw wind travel 23 km from the same seaside ("Seaside-1") to another residential terrain ("Res-2"). In the areas between "Seaside-1" and "Res-1" or "Res-2", there are condensed residential areas (e.g. low-rise houses, factories, middle-rise apartments) with scattered agricultural sites in

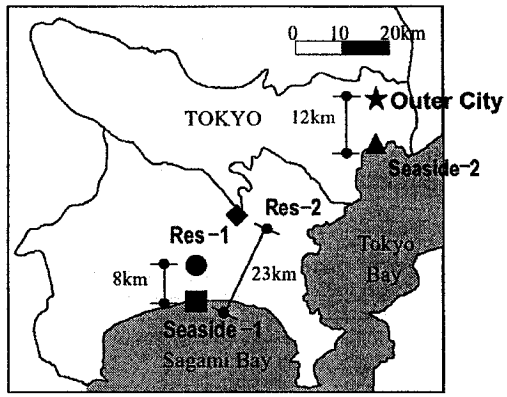

Fig. 2.5. The observational sites of Tamura et al (2001b).

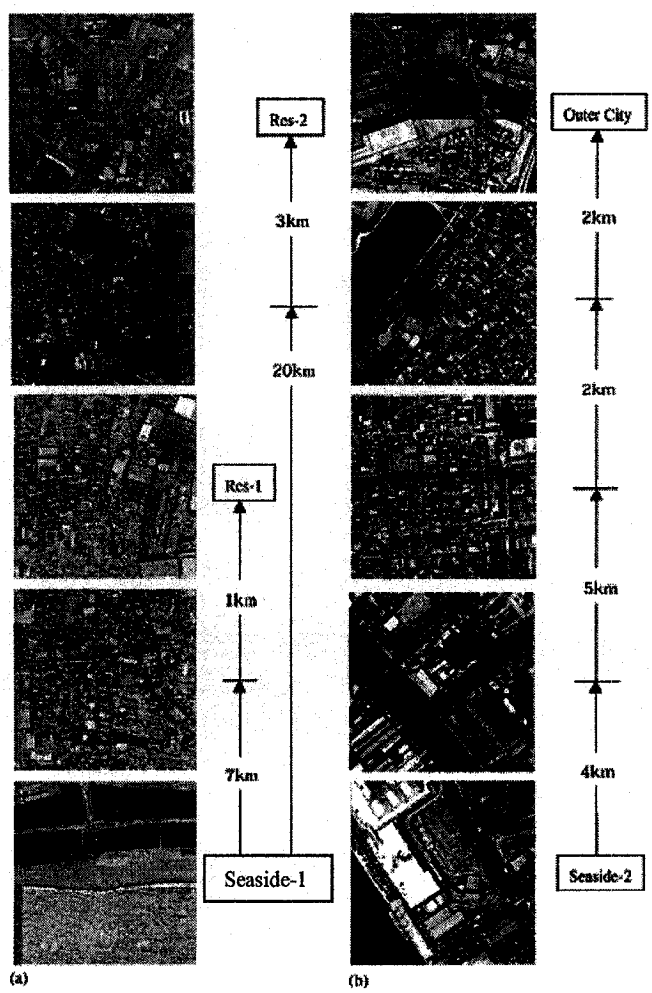

Fig. 2.6. Aerial photos between observational sites of Tamura et al (2001b): (a) "Seaside-1" to "Res-1" to "Res-2"; (b) "Seaside-2" to "Outer City".

between. Project 3 saw wind travel 12 km from a seaside ("Seaside-2") to the north-east region of Tokyo city ("Outer City") with more complex terrain features/changes on the fetch. Aerial photos shown in Fig. 2.6 depict the fetch circumstances; however, the information is somewhat blur. All speed profiles – see Fig. 2.7 - show strong power law features with reference speeds between 15 and 20 m/s (the strongest winds in the study). Since the power law feature is perceived as the property of homogeneous terrain, all these three patches closest to their respective downwind sites, which have length of 1 km, 3 km or 2 km respectively, can be regarded as matured homogeneous terrain. Therefore, patches of length of the order of 1 km can be regarded sufficient to generate a matured homogeneous terrain. In other words, roughness changes further upwind such a length may not be relevant to the wind effects at the site. Therefore, the pertinent fetch length is considered in the order of 1 km as afore-mentioned.

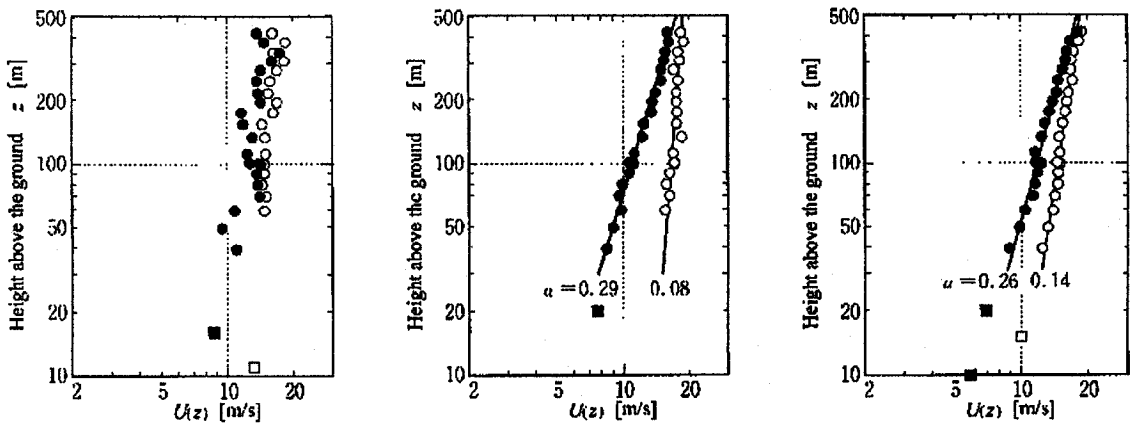

(a) (b) (c)

Fig. 2.7. Mean wind speed profiles at two sites during the same storms: (a) "Seaside-1" to 'Res-1'; (b) "Seaside-1" to "Res-2"; and (c) "Seaside-2" to "Outer City" (Tamura et al 2001b), where the hollow symbols (○; □) are data measured at upwind site, and the solid symbols (●; ■) at downwind site.

The hurricane field study of Letchford et al (2001) asserted that the ESDU (82026) transitional model may tend to overestimate, as much as around 20%, after they measured the increase in speed at 10 m height about 500 m downwind of an R-S roughness change.

2.4 Results on low-rise building wind loading

Annotations

All of the studies reviewed in this section were conducted in wind tunnels and investigated low-rise buildings, except for Tsutsumi et al (1992) for medium-rise buildings.

Hussain and Lee (1980) tested the *mean* loads on rectangular prisms of different side-wall ratios and heights, embedded within identical prisms, except for testing the parameter of height difference of neighboring buildings to the test building. The roughness cubes were arranged with different λ in either normal or staggered layout. Hussain and Lee (1980) compared drag coefficients (C_D) of a cube (12.6 m side-length full-scale) in a set of λ*'s* of 5%, 10%, and 20% in normal layout, and 10%, 20% and 25% in staggered layout. The value of C_D decreases gradually when λ becomes ≥ 0.2. In test case with an S-R roughness change, the wind loads reduce with the increase of fetch length x before leveling off, and the reduction is more abrupt for higher λ but more gradual for lower one. Fig. 2.8 shows that C_D reduces with the increase of x and/or λ. For the normal layout of $\lambda = 5\%$ and the staggered layout of $\lambda = 10\%$, the reductions almost complete within fetch length $x = 25H$, i.e., 315 (= 25×0.036×350) m full-scale, where H is the roughness element height. For the normal layout of $\lambda = 20\%$ and the staggered layout of $\lambda = 25\%$, the reductions are almost complete within $x = 10\ H$, i.e., 126 m full-

scale. Generally speaking, majority of the load changes can be attributed to the near-site roughness configuration within a short fetch length. Building shape difference may not cause significant wind load change. Roughness-element normal layout may induce more severe mean loads than the staggered layout.

Wiren (1983) measured the proximity effect on the pressures on a building that is surrounded by identical buildings in regular arrays of various λ values, the arrays having one, two or three rows of buildings. Pressures are nearly constant in any vertical section along the building walls for all wind directions and fetch configurations, except at the end bays of the windward and gable walls of the building in isolation at oblique wind attack. The change of λ and the number of rows of the surrounding buildings affect the wind loads on the test building.

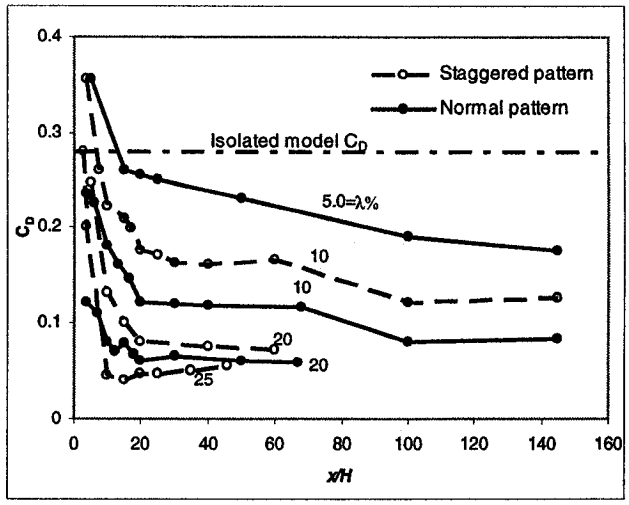

Fig. 2.8. Variation of drag coefficient C_D with fetch length x for cubes of height H, (Hussain and Lee 1980).

Keeping the average height constant, Sill and Fang (1990) studied the variation of individual roughness element heights, and found insignificant pressure changes.

Ho et al (1991) and Ho (1992) measured the flat-roof wind loads in more realistic proximities with upwind terrain as OC or Suburban. Upwind terrain has less load effects than the immediate surrounding; the upwind fetch has effects on the overall load level while the immediate surroundings affect both the overall load level and the streamline pattern and wind direction. Difficulties were found in accurate prediction of low-rise building wind loads even for simple surroundings; the large load variability suggests that it is not necessary to give separate treatment of partially exposed buildings. Design loads may be increased to account for the potentially well-organized aerodynamic behavior, e.g. roof corner suction for buildings in exposed conditions. Average reduction in peak loads due to the rougher Suburban exposure may reach approximately 40%.

Tsutsumi et al. (1992) studied the pressure characteristics of a building in a group, compared a staggered layout with a normal layout, and examined the wind directional effects. The building layout controlling parameter was the building volume ratio ϕ, which is the ratio of the total floor area of a building to the building lot area. The horizontal drag coefficients vary drastically with additions of upwind buildings in row. The drag coefficients rapidly level off after the 2 or 3 rows of shielding buildings, slightly depending on the layout pattern. The open space immediately upstream to the building greatly influences the drag coefficients. If ϕ is constant and the intervals between taller buildings become larger, the drag increases. Roughness elements in normal layout cause more severe loads than staggered layout.

Holmes (1994) examined houses in grouping with up to 4 rows of houses in Suburban. The pressure coefficients were calculated referencing to a common reference pressure. The pressures are largely insensitive to the number of upwind rows of buildings, but are

very sensitive to the geometry of the frontal open space. The frontal building reduces the wind loads; the shielding effect is large when the frontal open space gets small, but gradually reduces as it increases. If the open space is kept constant, the pressures stabilize after a number of rows of shielding buildings.

Tieleman et al (1994) studied the magnitudes and distributions of pressures on roof corners and edges of rectangular prisms immersed in various BL's. The extreme pressures locate just below the axis of the corner vortex. The mean pressures decrease rapidly with increase of length of the ray, or with increase of *Iu*. The root-mean-square (r.m.s.) pressures are insensitive to *Iu* in excess of 10%. Lateral (*v*-component) turbulence intensity (*Iv*), which can be obtained by altering the spire-roughness arrangement, changes the higher peak suctions in edge and near corner.

Kawai and Nishimura (1996) measured the flat-roof suctions and the velocities simultaneously. The fluctuation is amplified remarkably by the approaching turbulence, especially the low-frequency *v*-component turbulence.

Sitheeq et al (1997) measured mean and rms pressure on all faces of a cube normal to wind direction under three different BL's, which are described by Table 2.3. Considering the drastic differences in the approach flows, the mean pressures referencing to a common reference pressure are nearly the same for BL 1 and BL 2, and are somewhat larger in absolute value on all faces for BL 3. Change of the integral scale of longitudinal turbulence L_u^x does not cause significant changes in the mean and rms pressure distributions.

Keifer and Plate (1998) examined the effects of accurate modeling of upwind proximity geometries, and the test-building geometries by investigating the "influence of

Table 2.3. The boundary simulation parameters of Sitheeq et al (1997).

BL	G (m)	Power law α	Iu (%)	L_u^x (m)	U_{roof}/U_G
1	1.2	0.28	18	0.69	0.66
2	0.8	0.27	15	0.48	0.74
3	0.5	0.27	10	0.22	0.87

stepwise-added surroundings" on the roof peak suctions. Roughness changes at upwind further than 9 H (21 m) have insignificant effects on mean pressure coefficients, even when a high-rise building is added onto a fetch location 29 H (609 m) upwind from the site. However, in the latter condition, the rms pressure coefficients are affected considerably.

Case and Iysumov (1998) compared local loads and selected structural loads of three buildings with a common roof slope (4:12) and common gable wall length, in OC and Suburban. The wind tunnel had a dimension of 3.4×2.5×39 m (width×height×length) and had spires mounted at the inlet, which augmented the BL depth and accelerated the BL growth. All pressure coefficients were defined with respect to a constant OC speed pressure in that study. The findings included that (a) buildings located within a Suburban terrain experience lower loads than if located in an OC terrain, (b) no significant trend difference exists for the three buildings, and (c) building experiences lower loads as it becomes embedded in its surroundings, the reduction in local peak suctions may be as high as 30% from OC to Suburban and this reduction is most apparent on wall and roof loads.

Young and Vickery (1998) found that the roof-joist loads level off rapidly with the length increase of the frontal open space (within 100 m), approaching the loading level in OC.

Jia and Sill (1998) examined the surface pressure changes on a cube surrounded by identical cubes distributed with various λ, in order to examine the shielding effects on cladding loads, and the speed profile variation with λ. The wind loads decrease rapidly with the increase of z_o, until λ reaches about 0.2, and the loads appear almost constant and z_o decreases afterwards. This phenomenon indicates the limit of the shielding effect of upstream roughness elements.

Banks et al (2000) visualized the conical vortex behavior on flat roofs, with pressures simultaneously measured beneath the vortex visualization plane for worst wind directions. The greatest suction follows directly beneath the moving vortex core. For smooth flow, the suction beneath the core varies inversely with the vortex size. For turbulent flow, no clear relationship between vortex size and suction was found.

Comparisons

Above homogeneous terrain, the wind loads reduce significantly while terrain becomes rougher (Hussain and Lee 1980; Tsutsumi et al 1992; Ho 1992; Case and Iysumov 1998; Jia and Sill 1998). The reductions of the actual peak suctions from OC to Suburban can be as high as 40% (Ho 1992), or 30% (Case and Iysumov 1998). In general an isolated building in Suburban terrain exposure experiences approximately 15-25% lower wall loads and 13% lower roof suctions than the building in OC (Case and Iysumov 1998). When $\lambda \geq 0.2$, the loads are close to constant and do not decrease further (Jia and Sill 1998).

If the general roughness remains constant but individual roughness element geometries vary, the loads may not change significantly. Individual roughness element

height variation may not have significant load effects (Sill and Fang 1990). Normal layout of upwind roughness elements of the same amount may induce somewhat higher loads than staggered layout (Hussain and Lee 1980; Tsutsumi et al 1992; Ho 1992).

Roughness conditions upstream and near site affect the loads more than those far from site (Hussain and Lee 1980; Ho et al 1991; Ho 1992; Tsutsumi et al 1992; Holmes 1994; Young and Vickery 1998; Keifer and Plate 1998). A very rough fetch may take a length of the order of 100 m (Hussain and Lee 1980; Young and Vickery 1998), or 2 or 3 rows of shielding buildings (Tsutsumi et al 1992), or a number of rows of shielding buildings (Holmes 1994), to form a fully matured upstream terrain. On the other hand, a pertinent fetch may take longer length from the rms load perspective (Keifer and Plate 1998); to the contrary, it may take shorter wind-tunnel length from the flow turbulence perspective (Letchford et al 2001). The loads increase rapidly with the length of the frontal open space before leveling off (Holmes 1994; Young and Vickery 1998).

BL turbulence variation, especially the *Iv* variation, causes significant change in the roof corner and edge suctions (Tieleman et al 1994; Kawai and Nishimura 1996; Banks et al 2000). Roof corner mean suctions under corner vortex decrease rapidly with the distance from the apex, or with the increase of *Iu*, while the fluctuating pressures are insensitive to *Iu* in excess of 10% but sensitive to the low-frequency *v*-component spectrum (Tieleman et al 1994). Furthermore, *Iv* varies with the wind tunnel entrance spire setting and/or the fetch roughness arrangements (Tieleman et al 1994).

Building shape variation may not have significant loading effects (Hussain and Lee 1980; Case and Isyumov 1998), and L_u^x does not have significant effects on the overall

loads (Sitheeq et al 1997). However, according to Wiren (1983) building shape can strongly stabilize the wall loads for various surroundings.

2.5 The current issues

A number of important issues have been found from the previous results and are summarized as follows.

The assessment of terrain effects with the large-scale consideration may not be appropriate for estimating the wind profiles/loads for building levels which mostly sense small-scale roughness changes close to the site (Zhang and Zhang 2001). It is of great interest to investigate the wind profiles/loading above fetch with small-scale roughness changes close to the site.

It is found that the experimental validation for the ESDU (82026) model (for inhomogeneous terrain) may not be sufficient. However, the ESDU (82026) model has been adopted into a number of wind standards and codes of practice. Moreover, the ESDU (82026) model for inhomogeneous terrain may not be fully compatible to the power law model for homogeneous terrain, both models coexisting in ASCE 7-02; i.e. a conflict exists in this wind standard.

Discrepancy is found among different national/international wind standards and codes of practice on the specification of the minimum fetch length requirement for a patch to qualify as matured homogeneous terrain. Table 2.4 has shown that the minimum fetch length of a Suburban(-type) patch to qualify as Suburban homogeneous terrain is specified as 1500 m by NBCC 1995, 100 m by in BS 6399-2 (1997), and 800 m (or 10 building heights) by ASCE 7-02.

Discrepancy is also found in the standard specifications on the terrain *Ce* factor. The design load estimated by ASCE 7-02 for above Suburban-Urban terrain is 25% less than that by ASCE 7-95 for the same type of terrain. In detail, ASCE 7-95 specified a 0.85 Suburban-Urban exposure factor (cf. ASCE 7-95's Figs. 6-4 – 6-8) for building cladding loads, i.e. the cladding loads above Suburban/Urban is about 85% of their OC counterpart, but ASCE 7-95 did not specify a directionality factor or a reference velocity pressure reduction factor. Different from ASCE 7-95, ASCE 7-02 adopts both the velocity-pressure reduction factor approximately equal to 0.75 (cf. ASCE 7-02 Table 6.3), and a directionality factor of 0.85 (cf. ASCE 7-02 Table 6.4). It is found that the ASCE 7-95 specification is supported by the work of Ho (1992) and Case and Isyumov (1998), while justification for the change of standard is at the very least questionable. In other words, it is still needed to justify which should be the most appropriate specification as the Suburban exposure (*Ce*) factor.

Table 2.4. Roughness length z_0 and min. fetch length specifications of wind standards and codes of practice.

Terrain class		NBCC: 1995	ASCE 7-02: 2003	AS/NZS 1170.2: 2002	BS 6399-2: 1997
Coastal	z_0 (m)	0.02	0.005	0.002	0.003
	min. fetch	-	Max (1524 m, 10*H*)	Variable*, dependent on *H*	1000 m
OC	z_0 (m)	0.02	0.02	0.02	0.03
	min. fetch	1500 m	-	Variable*, dependent on *H*	-
Suburban/Urban	z_0 (m)	0.3	0.3	0.2	0.3
	min. fetch	1500 m	Max (800 m, 10*H*)	Variable*, dependent on *H*	100 m (with $H_o \geq 5$ m)
Large-city-centre	z_0 (m)	~1	-	2	-
	min. fetch	1500 m	-	Variable*, dependent on *H*	-

H : *Building height;*
Ho : *Average roof level;*
* : *= 1000 (for H < 50); = 2000 (for 50 ≤H < 100); = 3000 (for 100 ≤H < 200); = 4000 (for H ≥ 200) (unit: m).*

2.6 General comments

The code specifications on the exposure (*Ce*) factor, especially those for inhomogeneous terrain, were mainly developed with the meteorological assumptions that should be more appropriate for predicting higher boundary-layer level but not for winds at building heights. As a result, this literature review has revealed that a number of grey areas exist in the code/standard terrain-related provisions. A systematic study should be carried out to tackle the issues pertaining to the terrain exposure (*Ce*) factor for more appropriate (or accurate) design specifications.

Most recently, wind engineering studies found that terrain roughness patches of different distance to the site have different strengths of influence, and the building wind loads are very sensitive to small-scale roughness variations. Therefore, variations of wind speed and *Iu* profiles, as well as low-rise building loads, above fetch with roughness changes should be investigated in experiments in great detail.

Presently, the wind tunnel approach appears feasible and promising, and particular attention should be given to small-scale roughness changes close to the site. Because available full-scale data are limited, and previous numerical modeling efforts have been recognized as the present standard, this study will also develop a numerical simulation to ensure that the present wind-tunnel findings can be at least as good as the current numerical results.

Chapter 3 Wind tunnel methodology

3.1 Overview

This chapter presents the general wind tunnel configuration, the data-measurement equipment consisting of the LabVIEW-controlled hotwire velocity system and the DSM 3000 pressure system, the wind-tunnel scaling determination, the fetch design, the low-rise building pressure test model, and the pressure-data extreme value determination methods. The similarity principles, ASCE wind tunnel testing standard (1999), as well as established work have been used as guideline in the present wind tunnel experimentation.

3.2 General setting

The wind tunnel of Building Aerodynamics Laboratory at Concordia University was used for this study. Its working section is 12.2 m long and 1.8 m wide. It has an adjustable roof height around 1.8 m, providing negligible pressure gradient along the test section. The traditional floor setting, carpet roughness, is appropriate for Open Country (OC) terrain simulation. Its adjustable ceiling system is kept unaltered throughout this study in order to make the floor roughness as the sole variable. More details about this wind tunnel were given by Stathopoulos (1984). This wind tunnel with the test model on the turntable is depicted in Fig. 3.1.

The inlet screen was installed behind 6 horizontal rods (pipes) of different diameters. A board mounted with egg boxes was placed adjacent to the inlet screen. These formed the inlet setting, depicted in Fig. 3.2. The inlet setting intended to regulate the entrance

flow profile and allowed the boundary layer profile to develop as naturally as possible along the floor downstream.

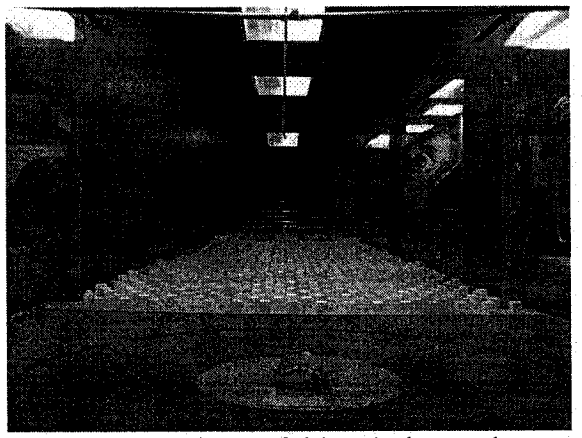

Fig. 3.1. Photo of this wind tunnel.

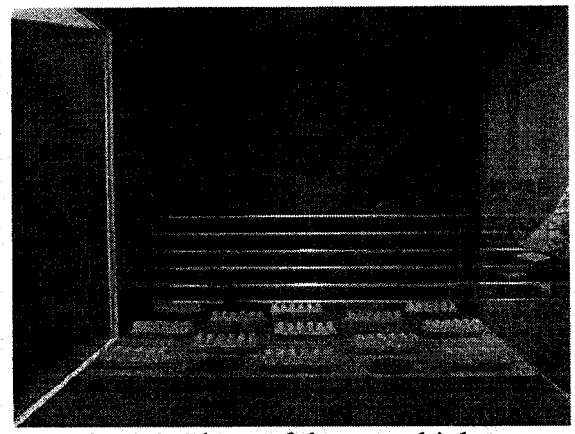

Fig. 3.2. Photo of the tunnel inlet.

A general-purpose program was developed in LabVIEW environment with G computer language in a host PC computer that controlled the scan frequency and duration of a hotwire device via a multiplexer. Figure 3.3 shows the frontal panel and block diagram of this program. This LabVIEW program reported data statistics on-line, and recorded data for off-line process. The scan frequency was set at 1000 Hz, and the scan duration was set routinely at 32.768 seconds. Velocity time histories were recorded for z = 25 mm (full-scale 10 m elevation), z = 38 mm (15.2 m, the mean-roof height of the present low-rise building model) and z = 250 mm (100 m) for each test case.

Scanivalve's DSM 3000 system (see Fig. 3.4) was connected to two ZOC-33 pressure transducers, each of which has factory-made capacity of scanning 64 pressure taps simultaneously. The DSM 3000 system was controlled by a host computer via the Internet. The scanning frequency was set at 250 Hz. Altogether 13500 frames of data scans were measured in each run which took a 54 second scan duration, i.e. a single tap's

pressure time history consists of 13500 data points. A manual has been written and presented in Appendix 1 for installation and operation of this system.

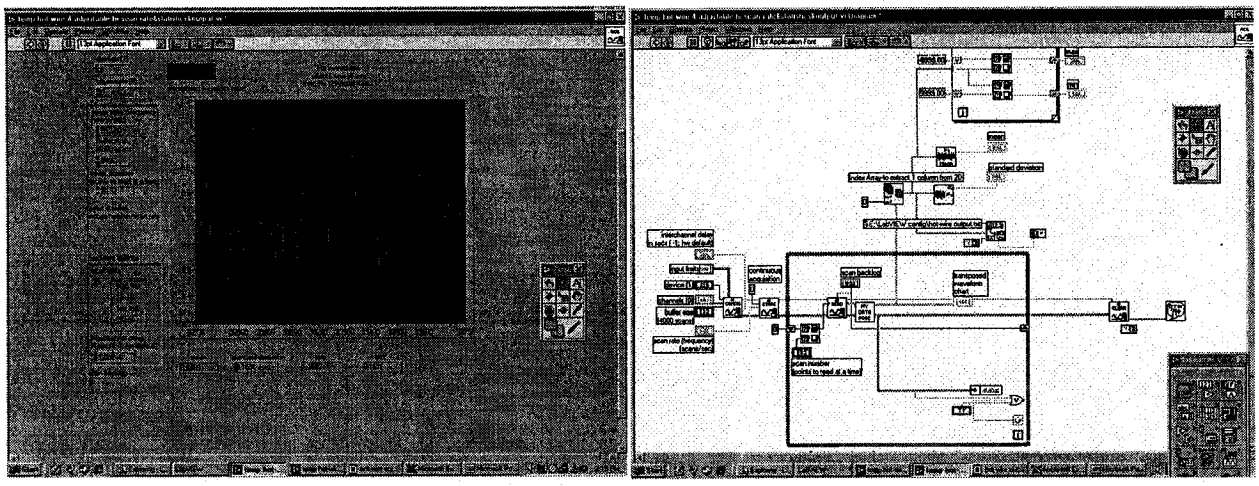

Fig. 3.3. Frontal panel and the block diagram of the present LABVIEW program.

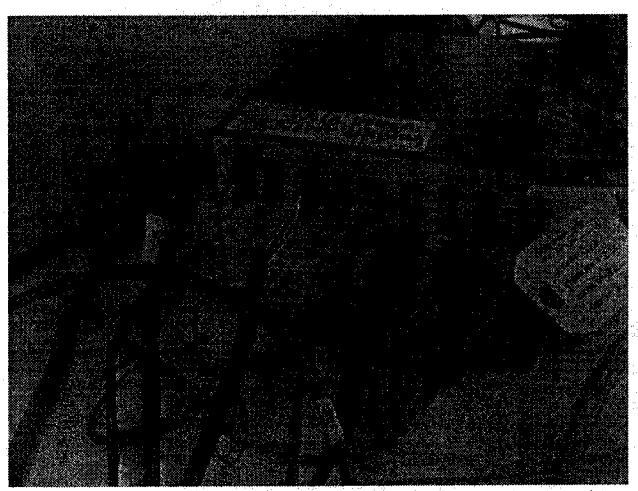

Fig. 3.4. Photo of DSM 3000's frontal panel.

3.3 Homogeneous terrain testing

Carpet roughness was used to simulate the OC as afore-mentioned. The gradient height was around 600 mm above the turntable, and the gradient speed was about 12.5 m/s. The

wind tunnel longitudinal scale of turbulence $(L_u^x)_{W.T}$ is determined as 0.4 m by fitting the actual velocity spectrum to the von Karman equation. The result is shown in Fig. 3.5. As seen in this figure, the high-frequency range of the present spectrum is lower than that of Stathopoulos (1984), measured in the same wind tunnel. The reason is not clear; however, this energy drop should not significantly affect the subsequent data analysis. Similar high-frequency energy drop was also found in Tieleman (1992). For OC terrain, the wind tunnel length scale, $(L_u^x)_{W.T.}/(L_u^x)_{F.S.}$, was determined as 1/400 by assuming $(L_u^x)_{F.S.}$ as 160 m. The gradient speed (~12.5 m/s) was regarded as 1/2 to 1/3 of the corresponding full-scale value. The wind tunnel time scale is determined by similarity principle, i.e. $(L/UT)_{W.T.} = (L/UT)_{F.S.}$, thus the time scale $T_{W.T.}/T_{F.S.} = (L_{W.T.}/L_{F.S.})/(U_{F.S.}/U_{W.T.}) = 1/400 \times 2$ or $3 = 1/200$ or $3/400$. This study decided to take the time scale as 3/400. A MATLAB program developed for the present spectral calculation is given in Appendix 2.

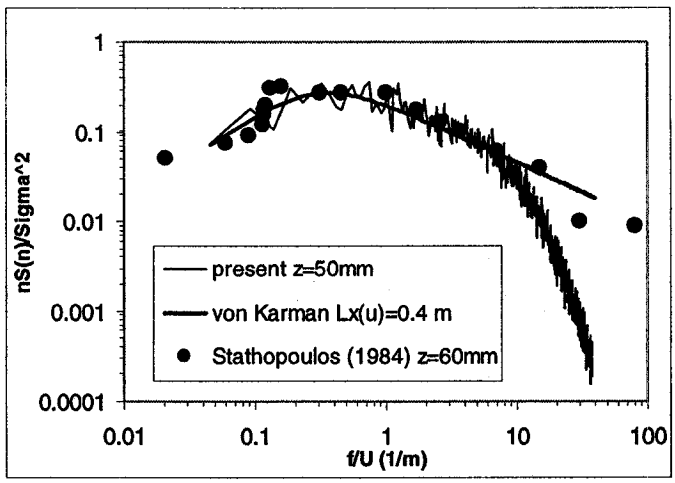

Fig. 3.5. Wind speed spectra measurements for OC terrain at 50 mm above the turntable.

Suburban and Urban terrain models were expected to simulate the Class 5 (z_o = 0.25 m) and Class 7 (z_o = 1 m) in the Davenport terrain roughness classification (Table 2.1),

corresponding to power law α values of 0.25 and 0.33 (cf. ASCE 7 1999). The z_o values can be translated into roughness element dimension by Eq. (2.12).

Suburban and Urban fetches were mainly simulated by using "S" and "U" types of roughness panels, respectively. Figure 3.6 depicts the configurations and dimensions of two types of roughness panels. The "S" type panel was distributed with Styrofoam cubes in staggered pattern. The Styrofoam cubes were cut by hot string-cut, having dimension of 1-by-1-by-1 inch^3 (2.54^3 cm^3). The "U" type panel is the same as the "S" type panel, except that the cubes on the "U" type panel are of dimension of 1.5-by-1.5-by-1.5 inch^3 (3.81^3 cm^3). In addition, this study also employed a "CB" type panel mounted with egg boxes to assist in the floor setting (see Stathopoulos 1984).

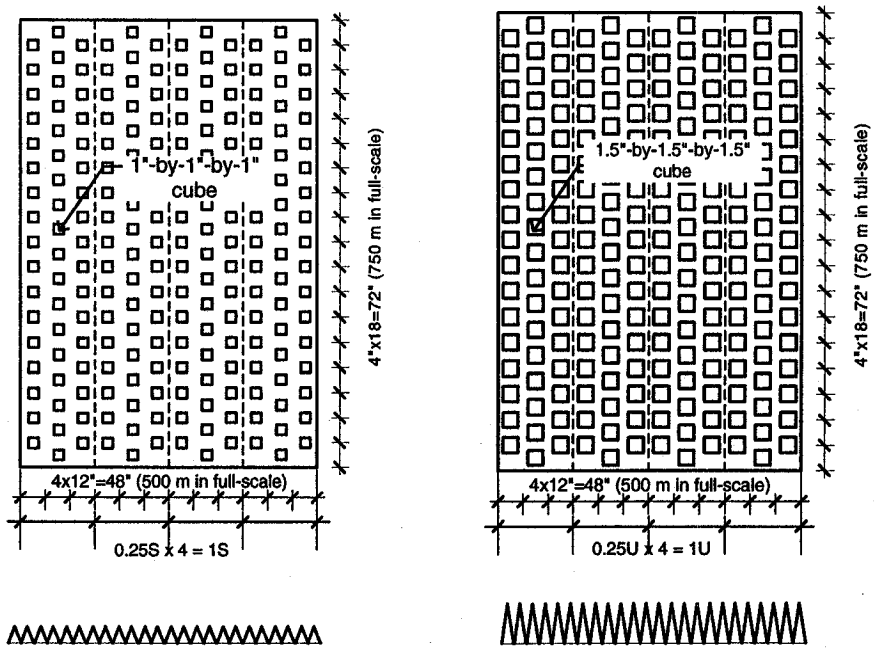

S-type U-type

Fig. 3.6. Suburban (S-type) and Urban (U-type) panels, fabrication and representation.

It would be ideal to simulate each of these basic Suburban or Urban fetch cases by a single type of roughness elements. In reality, the present Suburban fetch employed both "S" and "U" type panels, the latter of which were placed close to the tunnel inlet, and the Urban fetch used both "U" and "CB" type panels with the latter close to the tunnel inlet. The larger roughness elements placed at the far-upwind floor section were intended to absorb the extra momentum in the wind tunnel entering flow. Figures 3.7 and 3.8 depict details of the fabrication and presentation of the Suburban and Urban fetches, respectively. The power law index α, roughness length z_o, and the friction velocity u_* have been evaluated for the wind tunnel OC, Suburban and Urban speed profiles as shown in Table 3.1. The values of α match well with their corresponding values recommended in the wind tunnel testing standard ASCE (1999). The resultant z_o values are generally satisfactory, except that the Suburban z_o value of 0.42 m is higher than the value of 0.25 m recommended in Davenport et al (2000); however, this difference has been found insignificant in the subsequent data analyses. It is worth noting that the value of z_o is very sensitive and its determination depends on a number of factors that include wind tunnel scaling errors, testing approach, etc.

Table 3.1. Full-scale correspondences of the modeled speed profile parameters.

	α	z_o (m)	u_* (m/s)
OC	0.14	0.024	1.52
Suburban	0.26	0.42	2.13
Urban	0.32	1	2.40

3.4 Inhomogeneous terrain testing

In this wind tunnel, patches of different roughness and length can be combined piecewise to form various upstream fetch cases that represent different terrain configurations up to a

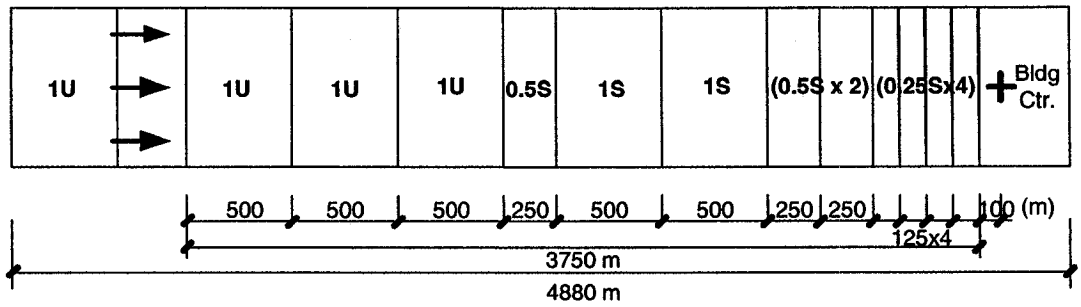

(a) Dimensions (m) full-scale

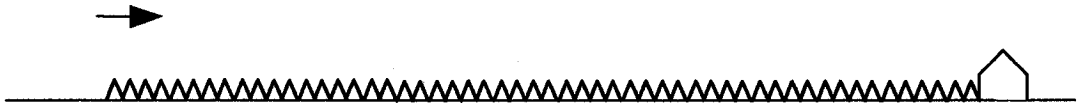

(b) Schematic of Suburban terrain for presentation

Fig. 3.7. Suburban fetch fabrication, testing and representation.

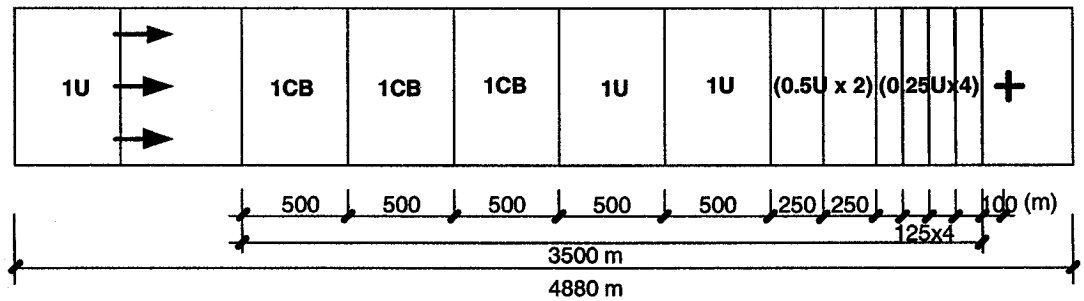

(a) Dimensions (m) full-scale

(b) Schematic of Urban terrain for presentation

Fig. 3.8. Urban fetch fabrication, testing and representation.

maximum fetch length about 4 km. A quarter of the standard panel of an along-wind length of 1 foot (30.3 cm, or about 125 m full-scale) is the present module patch length, i.e. the minimum fetch resolution of this study.

Design of the number of fetch cases took into account resources and uncertainties such as those due to screen dust accumulation, temperature change, facility aging. As a result, this study tested 69 fetch cases, out of which 58 cases were tested with both pressure and velocity, with another 8 cases dedicated to pressure test, and 3 cases to velocity test. Fig. 3.9 depicts all fetches tested in this study.

As expected, the gradient height varied from case to case. Also, the gradient speed varied from about 11.5 to 13.5 m/s.

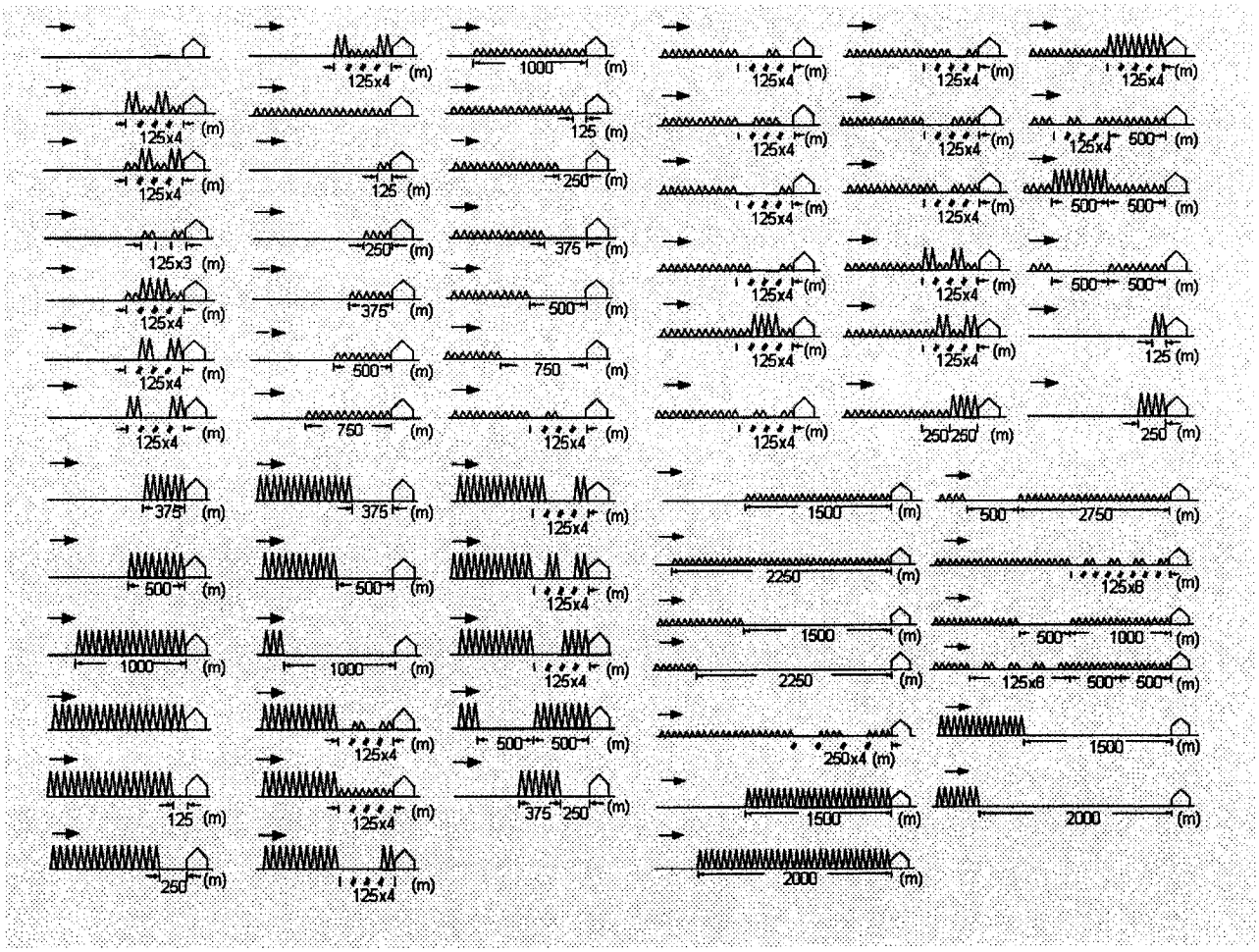

Fig. 3.9. All fetch cases examined in this study.

3.5 Low-rise building test model and testing

A pressure model of 4:12 roof-slope has been used in this study; such a building is considered typical for residential constructions (Case and Isyumov 1998). Figure 3.10 shows the pressure model on the wind tunnel turntable. Figure 3.11 presents the tap locations on the model surface. The dimensions of the model and the test wind azimuths are shown in Fig. 3.12. For each fetch case, pressure data are scanned for 13 wind azimuths (θ), namely, 0°, 35°, 40°, 45°, 50°, 55°, 90°, 125°, 130°, 135°, 140°, 145° and 180°.

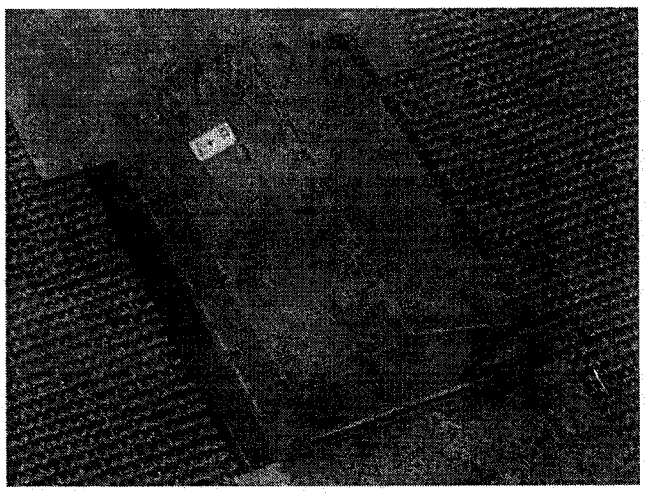

Fig. 3.10. Photo of the pressure model.

Usually, low-rise building surface is divided into a number of roof and wall aerodynamic zones in wind standards and codes of practice. This study follows the convention and defines the low-rise building surface into zones depicted in Fig. 3.13.

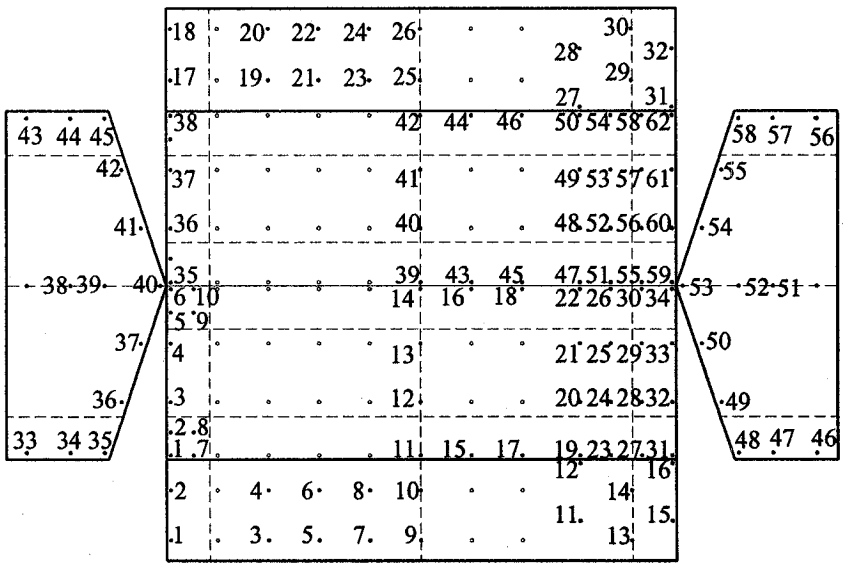

Fig. 3.11. Unfolded view of the pressure model with the tap locations (•: in use; o: dummy).

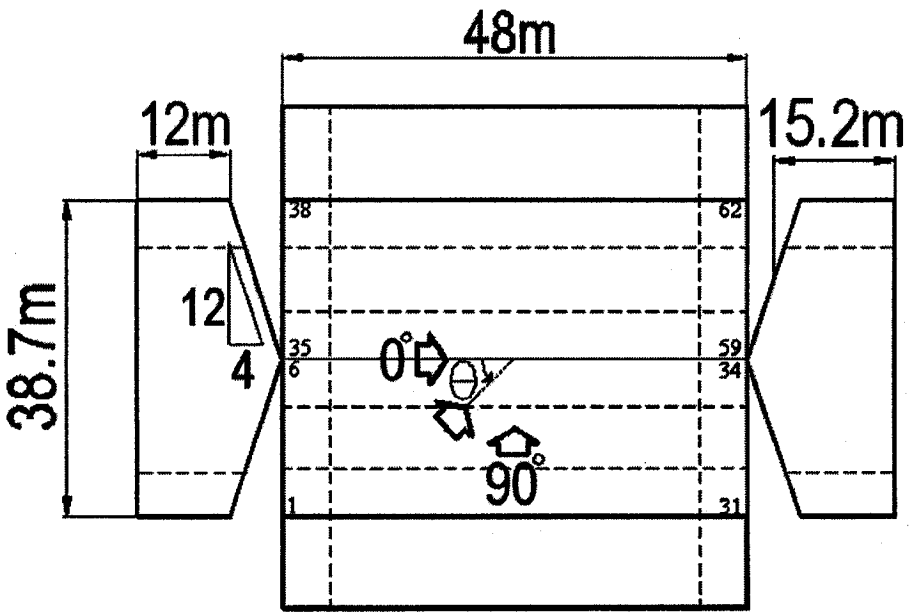

Fig. 3.12. Model dimensions and the wind azimuths (θ).

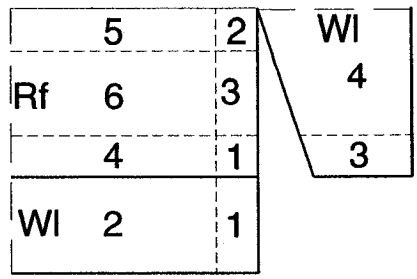

Fig. 3.13. Building surface zones (following the ASCE 7-02 definition).

3.6 Basic pressure data presentation

This study defines pressure coefficient (*Cp*) in two forms with different reference speed pressures as denominator. The first *Cp* definition is referencing always to a constant OC velocity pressure at building mid-roof height,

$$Cp = (p - p_o)/(0.5\rho U^2_{m-rf,OC}) \tag{3.1}$$

where p_o = static pressure, ρ = air density, and '*m-rf*,*OC*' = mid-roof height above OC terrain. Another definition is the traditional pressure coefficient Cp' that is referencing to the mid-roof height above *local* terrain speed pressure $U_{m\text{-}r,localTerrain}$,

$$Cp' = \Delta p/(0.5\rho U^2_{m-rf,localTerrain}) \tag{3.2}$$

Conversion between *Cp* and Cp' for one actual pressure can be made by the following relationship,

$$\Delta p = 0.5Cp'\rho U^2_{m-rf,localTerrain} = 0.5Cp\rho U^2_{m-rf,OC} \tag{3.3}$$

In this study, for Suburban terrain, $Cp'_{m-rf,suburban}$ is equal to $1.84\times Cp_{m-rf,OC}$, and for Urban terrain, $Cp'_{m-rf,urban}$ is equal to $2.26\times Cp_{m-rf,OC}$, i.e. the conversion coefficients are equal to 1.84 and 2.26 for Suburban and Urban against OC, respectively. Fig. 3.14 presents the conversion coefficients for a number of selected fetch cases, which show

considerable differences for different cases. Conversion coefficients for an additional number of cases are presented in Appendix 3. The differences indicate that the wind tunnel velocity pressures, as well as the static pressures, may change from case to case in this study. A computer program has also been developed to post the pressure coefficients onto drawing template, as presented in Appendix 4; this technique is applied for some results in Chapter 7.

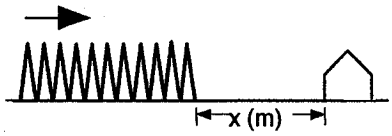

x(m)	125	250	375	500	1000	1500	2000
Coeff.	2.20	1.82	1.67	1.59	1.30	1.43	1.24

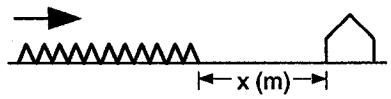

x(m)	125	250	375	500
Coeff.	1.70	1.52	1.36	1.30

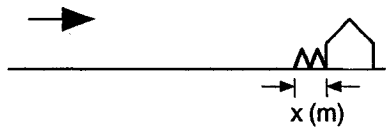

x(m)	125	250	375	500	750	1000	1500	2250
Coeff.	1.30	1.55	1.58	1.62	1.72	1.78	1.84	1.84

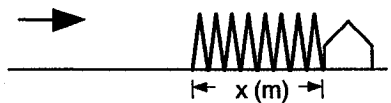

x(m)	125	250	375	500	1000	1500	2000
Coeff.	2.06	2.08	2.12	2.14	2.16	2.26	2.26

Fig. 3.14. Selected fetch cases and the corresponding conversion coefficients.

3.7 Extreme value analysis

This study has attempted mainly two methods for determining the pressure peaks. As an averaging method, Method 1 first breaks down a 13500 data-point time history into three

segments of 4500 data points each, and then averages three segmental peaks to determine the final peak value. As an application of the Gumbel distribution (cf. Suresh Kumar 1998 and Holmes 2001), Method 2 first breaks down the time history into ten segments of each of 1350 data points, then picks out ten segmental peaks, and finally fits these ten peaks by the Gumbel distribution (i.e. extreme value Type 1) with a cumulative probability of 0.975. It is worth noting that this number is used in Uematsu and Isyumov (1996).

Method 1 is chosen as the main method used for determining all *Cp* peak values in this study for its simplicity as well as reliability. Method 2 is used for the taps in the roof areas (roof corner and roof gable end) known to experiencing very large peaks. The following two cases refer to two roof taps' pressures measured for oblique wind azimuths (θ) and above OC terrain. The performance of these methods is demonstrated in the following two case studies.

The first case is for the pressure time history of roof Tap 35 with $\theta = 55^{\circ}$. Averaging three peaks, Method 1 yields *Cp min* = -6.01. On the other hand, Method 2 yields *Cp* min = -6.01, -6.21, -6.52 respective to the cumulative probability set at 0.925, 0.95 and 0.975. Figure 3.15a shows a segment of 1350 points of the pressure time history, i.e. 1/10 of the total amount of the data points in the time history. Figure 3.15b illustrates the Gumbel plot curve-fitting. In Fig. 3.15b u and s are respectively the mode and dispersion, which are the two parameters of the Gumbel plot. This typical case shows that the *Cp* min value determined by Method 1 matches that by Method 2 at a cumulative probability ≈ 0.92.

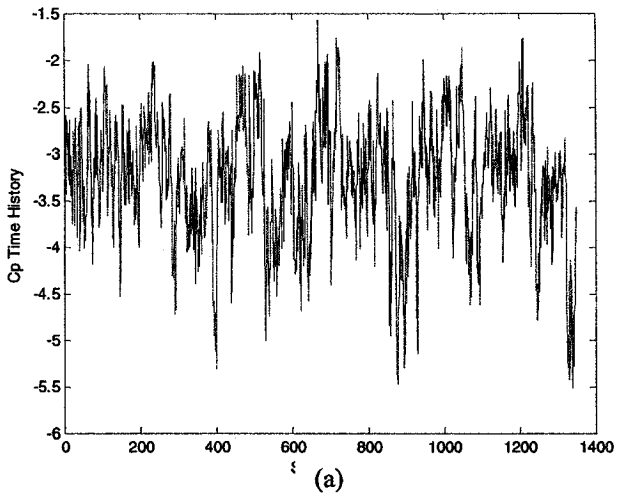

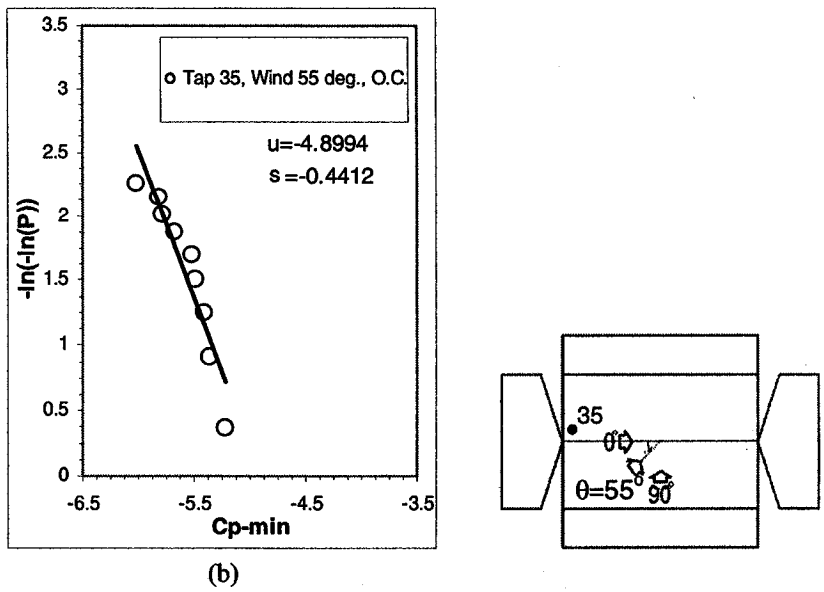

Fig. 3.15. Extreme value behavior and Gumbel plot of a segment of the *Cp* time history of Tap 35 under $\theta = 55^{\circ}$ above OC terrain: (a) time history (data points 1 – 1350), and (b) Gumbel plot.

The second case is for the time history of roof Tap 1, $\theta = 35^{\circ}$. Averaging three peaks, Method 1 yields *Cp* min = -3.33, corresponding to the result of Method 2 of a cumulative probability ≈ 0.90. Method 2 yields *Cp* min ≈ -3.50 for cumulative probability = 0.925.

It is also of interest to see the result of averaging another number of, say 10, peaks from their respective data segments. For the first case, averaging 10 segmental peaks yields *Cp* min = -5.65, corresponding to a cumulative probability ≈ 83%. For the second case, this process yields *Cp* min = -3.07, corresponding to a cumulative probability ≈ 82%. Overall, Method 1 seems to be appropriate.

3.8 Repeatability of the present pressure test

Figure 3.16 shows the *Cp* mean and *Cp* min values measured with $\theta = 90^{\circ}$ above OC terrain in two different tests, 31 days apart. This comparison shows that the repeatability is good. Such an agreement is typical for other cases tested.

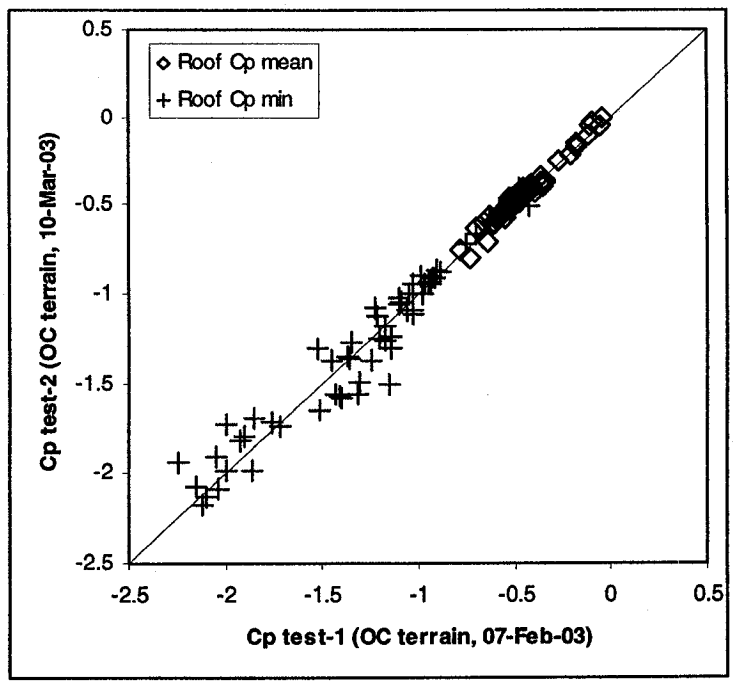

Fig. 3.16. Mean and minimum pressure coefficients measured on the same building roof under the same (OC) terrain in two tests.

Chapter 4 Numerical methodology

4.1 General

This chapter describes the development of the present numerical simulation of the flow-motion equations proposed by Taylor (1969). The model of shear stress variation with fetch (wall function) follows those suggested by Bradley (1968) and Garratt (1990). The control volume method suggested by Schmid and Bunzli (1995) is used for the present equation discretization. The conventional Tri-Diagonal Matrix Algorithm (TBMA, Patankar 1980) is modified in this study to solve the present linear equations of variable coefficients.

4.2 The equations

Following the discussion in Section 2.2, by dropping the first right-hand-side term of Eq. (2.1) and combining Eqs. (2.6) and (2.7), one gets:

$$U\frac{\partial U}{\partial x}+W\frac{\partial U}{\partial z}=\frac{\partial \tau}{\partial z} \quad (x\text{-momentum}) \tag{4.1}$$

$$\frac{\partial U}{\partial x}+\frac{\partial W}{\partial z}=0 \quad (\text{continuity}) \tag{4.2}$$

$$\tau=\left(kz\partial U/\partial z\right)^2 \quad (\text{shear stress}) \tag{4.3}$$

Eqs. (4.1) - (4.3) are associated with the boundary conditions,

$$U(z=z_o^{(i)})=W(z=z_o^{(i)})=0$$

$$\frac{\partial \tau}{\partial z}(z\rightarrow+\infty)=\frac{\partial W}{\partial z}(z\rightarrow+\infty)=0$$

in which U, W are the mean velocity on the x (streamwise) and z (vertical) direction, respectively; τ is the turbulent shear stress, and $z_o^{(i)}$ is the roughness length at a grid point i along the speed profile 'marching' direction.

Above homogeneous terrain, at close-to-ground layer the surface roughness dictates the wind speed, and at gradient height, the upwind speed profile dictates the gradient speed; between the close-to-ground level and the gradient height, the wind profile is governed by Eqs. (4.1) – (4.3). Experience has shown that these equations have the tendency to regulate the speed profile towards logarithmic, if the fetch becomes homogeneous and sufficiently long.

It is necessary to give the equations the close-to-ground layer's speed. For homogeneous terrain, the close-to-ground layer's speed is dictated by the surface roughness parameters z_o and u_* value by log law. This is consistent with the assumption that at such a low level, the speed is in equilibrium with the surface roughness. Regarding inhomogeneous terrain, the surface shear stress variations have been described by Bradley (1968) and Garratt (1990). Bradley (1968) suggested that the surface shear stress τ varies with the length of the downwind patch x in the relationship $\tau \propto x^{-0.2}$, i.e., $u_* \propto x^{-0.1}$, after a smooth-to-rough (S-R) roughness change. Garratt (1990) found that, after an S-R change, the stress initially increases to about twice the final value, and after an R-S change, the stress initially decreases to about half of its final value. As a result, this study found the following relations robust for the present numerical simulation,

$$u_*(x) = 2x^{-0.1}u_* \qquad \text{(S-R)} \tag{4.4}$$

$$u_*(x) = 0.4x^{0.1}u_* \qquad \text{(R-S)} \tag{4.5}$$

where u_* is the friction velocity at the (final) far-downwind terrain.

4.3 Equation discretization and programming

The control volume method suggested by Schmid and Bunzli (1995) was used for the present equation discretization. On the other hand, the finite difference method proposed by Taylor (1969) was also attempted with limited success. A regular grid of vertical interval of 2 m was used. The subsequent discretized equations were treated as linear equations of variable coefficients and were solved by an enhanced TDMA; this treatment is different from that of Schmid and Bunzli (1995), who treated their discrete equations as nonlinear equations with analytical solution.

Term 2 of Eq. (4.1) can be transformed,

$$W\frac{\partial U}{\partial z}=\frac{\partial (WU)}{\partial z}-U\frac{\partial W}{\partial z} \tag{4.6}$$

Eq. (4.2) gives

$$\frac{\partial W}{\partial z}=-\frac{\partial U}{\partial x} \tag{4.7}$$

Substituting Eq. (4.7) into Eq. (4.6) yields,

$$W\frac{\partial U}{\partial z}=\frac{\partial (WU)}{\partial z}+U\frac{\partial U}{\partial x} \tag{4.8}$$

Substituting Eq. (4.8) into Eq. (4.1), one gets

$$2U\frac{\partial U}{\partial x}+\frac{\partial (WU)}{\partial z}=\frac{\partial \tau}{\partial z} \tag{4.9}$$

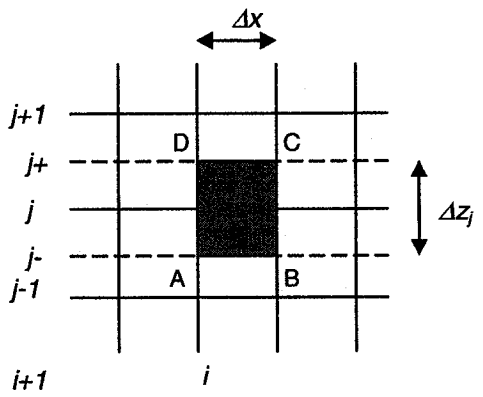

Fig. 4.1. Schematic of the grid.

After transforming the momentum equation into a flux conserving form and replacing τ by $(kz\partial U/\partial z)^2$, one integrates over the area ABCD indicated in Fig. 4.1 and the new equation becomes

$$\int_{x_i}^{x_{i+1}}\int_{z_{j-}}^{z_{j+}} 2U\frac{\partial U}{\partial x}dxdz + \int_{x_i}^{x_{i+1}}\int_{z_{j-}}^{z_{j+}}\frac{\partial(WU)}{\partial z}dxdz = \int_{x_i}^{x_{i+1}}\int_{z_{j-}}^{z_{j+}}\frac{\partial(kz\partial U/\partial z)^2}{\partial z}dxdz \qquad (4.10)$$

$$\text{Term 1 of Eq. (4.10)} = \int_{z_{j-}}^{z_{j+}}\left\{\int_{x_i}^{x_{i+1}} 2U\frac{\partial U}{\partial x}dx\right\}dz$$

$$= \int_{z_{j-}}^{z_{j+}}\left\{\int_{x_i}^{x_{i+1}}\frac{\partial(U^2)}{\partial x}dx\right\}dz = \int_{z_{j-}}^{z_{j+}}\left(U_{i+1}^2 - U_i^2\right)dz$$

Let $\Delta U_{i+1} = U_{i+1} - U_i$,

$$\text{Term 1 of Eq. (4.10)} = \int_{z_{j-}}^{z_{j+}}\left\{(2U_i + \Delta U_{i+1})\Delta U_{i+1}\right\}dz$$

$$\text{Term 2 of Eq. (4.10)} = \int_{x_i}^{x_{i+1}}\left\{(UW)_{j+} - (UW)_{j-}\right\}dx$$

$$\text{Term 3 of Eq. (4.10)} = \int_{x_i}^{x_{i+1}}\left\{(kz\partial U/\partial z)_{j+}^2 - (kz\partial U/\partial z)_{j-}^2\right\}dx$$

Hence, Eq. (4.10) becomes

$$\int_{z_{j-}}^{z_{j+}}\left\{(2U_i + \Delta U_{i+1})\Delta U_{i+1}\right\}dz + \int_{x_i}^{x_{i+1}}\left\{(UW)_{j+} - (UW)_{j-}\right\}dx$$

$$= \int_{x_i}^{x_{i+1}} \left\{ \left(kz(\partial U / \partial z) \right)_{j+}^2 - \left(kz(\partial U / \partial z) \right)_{j-}^2 \right\} dx \tag{4.11}$$

where $\Delta U_{i+1} = U_{i+1} - U_i$ (4.12)

The integral between z_{j-1} and z_{j+1} is approximated by a three-point formula, which is Eq. (A.7) of Schimid and Bunzli (1995) as

$$\int_{z_{j-}}^{z_{j+}} \psi(z) dz \approx \sigma_j^{-1} \psi_{j-1} + \sigma_j^{o} \psi_j + \sigma_j^{+1} \psi_{j+1} \tag{4.13}$$

presently, $\sigma_j^{-1}, \sigma_j^{o}$ and σ_j^{+1} are assumed to be equal to 1/8, 3/4 and 1/8, respectively.

The integral in x-direction is replaced by an implicit first-order formula, i.e.,

$$\int_{x_i}^{x_{i+1}} \psi(x) dx \approx \psi_i \Delta x \tag{4.14}$$

It should be noted that in this study Eq. (4.14) is different from the Eq. (A.8) of Schimid and Bunzli (1995), which is $\int_{x_i}^{x_{i+1}} \psi(x) dx \approx \psi_{i+1} \Delta x$.

$\Delta U_{i+1}, \Delta U_i$ and ΔU_{i-1} can be regarded as independent variables as shown in Fig. 4.2, then the equations hold a tridiagonal-matrix form with variable coefficients.

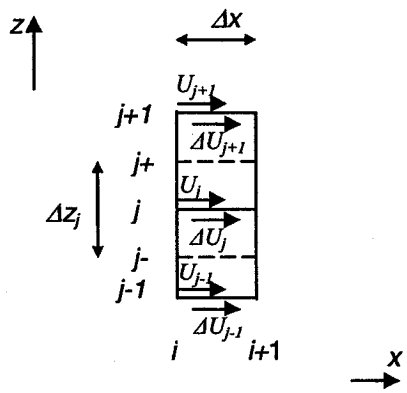

Fig. 4.2. Schematic of the grid and the variables in the calculation.

By virtue of Eq. (4.13), term 1 of Eq. (4.11) has the form,

$$\int_{z_{j-}}^{z_{j+}}\{(2U_i+\Delta U_{i+1})\Delta U_{i+1}\}dz =$$
$$\sigma_j^1\Delta z\{(2U_i+\Delta U_{i+1})\Delta U_{i+1}\}_{j-1}+\sigma_j^2\Delta z\{(2U_i+\Delta U_{i+1})\Delta U_{i+1}\}_j+\sigma_j^3\Delta z\{(2U_i+\Delta U_{i+1})\Delta U_{i+1}\}_{j+1}$$

(a)

Although $\sigma_j^1,\sigma_j^2,\sigma_j^3$ can be considered as functions of height z, so that the program can be more flexible but more difficult to adjust numerically, $\sigma_j^1,\sigma_j^2,\sigma_j^3$ are taken as constants in this study.

In light of Fig. 4.1 and the Eqs. (A.5) and (A.6) of Schmid and Bunzli (1995), which are, respectively,

$$(UW)_{j-}=\mu(UW)_{j-1}+(1-\mu)(UW)_j$$
$$(UW)_{j+}=\mu(UW)_j+(1-\mu)(UW)_{j+1}$$

Taking into account $\int_{x_i}^{x_{i+1}}\psi(x)dx\approx\psi_i\Delta x$, the integral core of Term 2 of Eq. (4.11) is,

$$\left|\mu(UW)_j+(1-\mu)(UW)_{j+1}\right|-\left|\mu(UW)_{j-1}+(1-\mu)(UW)_j\right|$$
$$=(1-\mu)(UW)_{j+1}+\mu(UW)_j-(1-\mu)(UW)_j-\mu(UW)_{j-1}$$
$$=(1-\mu)(UW)_{j+1}+(2\mu-1)(UW)_j-\mu(UW)_{j-1}$$
$$=(1-\mu)(UW)_{j+1,i}\Delta x+(2\mu-1)(UW)_{j,i}\Delta x-\mu(UW)_{j-1,i}\Delta x \qquad \text{(b)}$$

where μ is the weighting factor for interpolating, e.g. $(UW)_{j-}$ in terms of $(UW)_{j-1}$ and $(UW)_{j-}$, and set as 0.49 in this study.

Expanding Term 3 of Eq. (4.11) yields,

$$\int_{x_i}^{x_{i+1}}\left\{(kz(\partial U/\partial z))_{j+}^2-(kz(\partial U/\partial z))_{j-}^2\right\}dx$$

$$=\int_{x_i}^{x_{i+1}}\left\{k^2\left(\frac{z_j+z_{j+1}}{2}\right)^2\left(\frac{U_{j+1}-U_j}{\Delta z}\right)^2\right\}dx-\int_{x_i}^{x_{i+1}}\left\{k^2\left(\frac{z_{j-1}+z_j}{2}\right)^2\left(\frac{U_j-U_{j-1}}{\Delta z}\right)^2\right\}dx$$

$$= \frac{k^2\Delta x}{\Delta z^2}\left[\left(\frac{z_j + z_{j+1}}{2}\right)^2 \left(U_{j+1} - U_j\right)^2\right]_i - \frac{k^2\Delta x}{\Delta z^2}\left[\left(\frac{z_{j-1} + z_j}{2}\right)^2 \left(U_j - U_{j-1}\right)^2\right]_i$$

$$= \frac{k^2\Delta x}{\Delta z^2}\left(\frac{z_j + z_{j+1}}{2}\right)^2 \left(U_{j+1,i}^2 - 2U_{j,i}U_{j+1,i} + U_{j,i}^2\right)$$

$$- \frac{k^2\Delta x}{\Delta z^2}\left(\frac{z_{j-1} + z_j}{2}\right)^2 \left(U_{j,i}^2 - 2U_{j,i}U_{j-1,i} + U_{j-1,i}^2\right) \qquad \text{(c)}$$

Collecting each of the terms of Eq. (4.11) yields,

$$\sigma_j^1\Delta z\{(2U_i + \Delta U_{i+1})\Delta U_{i+1}\}_{j-1} + \sigma_j^2\Delta z\{(2U_i + \Delta U_{i+1})\Delta U_{i+1}\}_j + \sigma_j^3\Delta z\{(2U_i + \Delta U_{i+1})\Delta U_{i+1}\}_{j+1}$$

$$+ (1-\mu)(UW)_{j+1,i}\Delta x + (2\mu - 1)(UW)_{j,i}\Delta x - \mu(UW)_{j-1,i}\Delta x$$

$$- \frac{k^2\Delta x}{\Delta z^2}\left\{\left(\frac{z_j + z_{j+1}}{2}\right)^2 \left(U_{j+1,i}^2 - 2U_{j,i}U_{j+1,i} + U_{j+1,i}^2\right) - \left(\frac{z_j + z_{j+1}}{2}\right)^2 \left(U_{j,i}^2 - 2U_{j,i}U_{j-1,i} + U_{j-1,i}^2\right)\right\} = 0 \qquad (4.15)$$

i.e.,

$$\Delta U_{i+1,j-1}(\sigma_j^1\Delta z)(\Delta U_{i+1,j-1} + 2U_{i,j-1}) + \Delta U_{i+1,j}(\sigma_j^2\Delta z)(\Delta U_{i+1,j} + 2U_{i,j})$$

$$+ \Delta U_{i+1,j+1}(\sigma_j^3\Delta z)(\Delta U_{i+1,j+1} + 2U_{i,j+1})$$

$$+ (1-\mu)\Delta x U_{i,j+1}W_{i,j+1} + (2\mu - 1)\Delta x U_{i,j}W_{i,j} - \mu\Delta x U_{i,j-1}W_{i,j-1}$$

$$- \frac{k^2\Delta x}{\Delta z^2}\left\{\left(\frac{z_j + z_{j+1}}{2}\right)^2 \left(U_{i,j+1}^2 - 2U_{i,j}U_{i,j} + U_{i,j+1}^2\right) - \left(\frac{z_j + z_{j+1}}{2}\right)^2 \left(U_{i,j}^2 - 2U_{i,j}U_{i,j-1} + U_{i,j-1}^2\right)\right\} = 0 \qquad (4.16)$$

Eq. (4.16) forms a linear equation system with variable coefficients that can solved by an enhanced TriDiagonal-Matrix Algorithm (TDMA).

The above approach is used to treat the continuity equation. It follows Eq. (4.2) that

$$\int_{x_i}^{x_{i+1}}\int_{z_{j-}}^{z_{j+}} \frac{\partial U}{\partial x}dxdz + \int_{x_i}^{x_{i+1}}\int_{z_{j-}}^{z_{j+}} \frac{\partial W}{\partial z}dxdz$$

$$= \int_{z_{j-}}^{z_{j+}} (U_{i+1} - U_i)dz + \int_{x_i}^{x_{i+1}} \left(W_{z_{j+}} - W_{z_{j-}}\right)dx$$

$$= \int_{z_{j-}}^{z_{j+}} \Delta U_{i+1}dz + \int_{x_i}^{x_{i+1}} \left(W_{z_{j+}} - W_{z_{j-}}\right)dx = 0$$

By Eqs. (A.7) and (A.8) of Schmid and Bunzli (1995) and $W_{j+} = 0.5W_j + 0.5W_{j+1}$, it follows that:

$$\sigma_j^1 \Delta U_{i+1,j-1} + \sigma_j^2 \Delta U_{i+1,j} + \sigma_j^3 \Delta U_{i+1,j+1} + \Delta x(0.5W_{i+1,j} + 0.5W_{i+1,j+1} - 0.5W_{i+1,j-1} - 0.5W_{i+1,j}) = 0$$

$$W_{i+1,j+1} = W_{i+1,j-1} - \frac{1}{0.5\Delta x}\left(\sigma_j^1 \Delta U_{i+1,j-1} + \sigma_j^2 \Delta U_{i+1,j} + \sigma_j^3 \Delta U_{i+1,j+1}\right) \quad (4.17a)$$

where

$$W_j = \frac{W_{j+1} + W_{j-1}}{2} \quad (4.17b)$$

is assumed.

There is no coupling relation between Eqs. (4.16) and (4.17); we can solve Eq. (4.16) to find $\Delta U_{i+1,j-1}, \Delta U_{i+1,j}, \Delta U_{i+1,j+1}$, and then Eq. (4.17) to find W. Eqs. (4.16) and (4.17) have been programmed, and the program source code is presented in Appendix 5. Standard TDMA (Patankar 1980) is modified and used as the solver in this program.

4.4 Specifications of the inputs

This numerical simulation is applied for every fetch case tested in this study for velocity investigations. This numerical simulation has taken the wind tunnel characteristic values as program input (see Table 3.1). The wind tunnel reference gradient height is set constant 240 m. In computation domain, the boundary layer depth is divided into 120 vertical grids, with a vertical interval of 2 m.

4.5 Testing

Typical OC, Suburban and Urban terrain cases have been simulated and the results have been compared with log-law results, as shown in Fig. 4.3. The numerical results compare

well with the log law profiles. Furthermore, test runs have shown that this numerical program is robust for fetches with intensive roughness rises and falls.

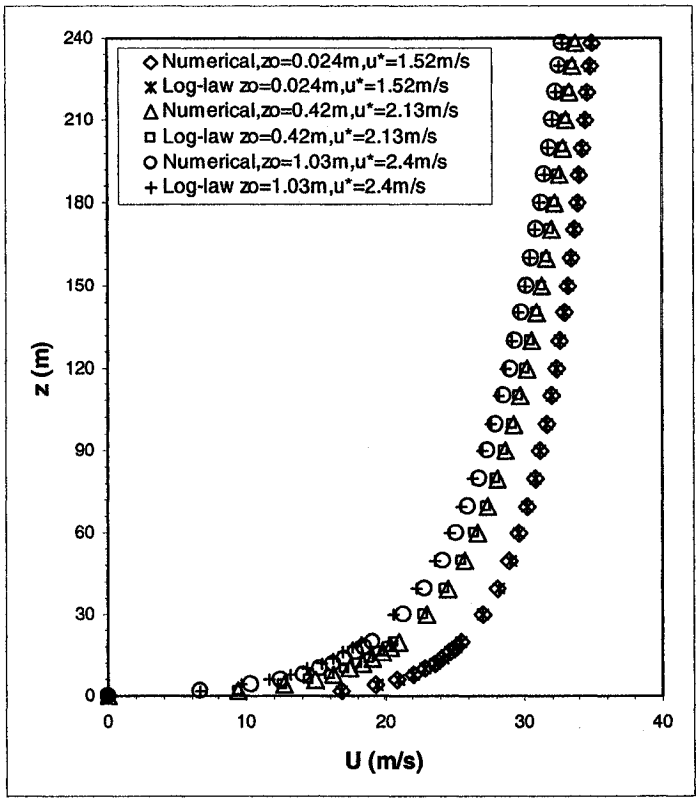

Fig. 4.3. Numerical simulations and log-law predictions of OC, Suburban and Urban.

Chapter 5 Wind speed results and discussion

5.1 Introduction

Previous studies on the variation of wind mean speed profile with inhomogeneous terrain usually assumed that wind speed profiles sense the roughness averaged in a large-scale terrain-grid, so terrain roughness patches of different distance to the site are regarded of equal importance. This is mainly due to the fact that the exposure characterization was primarily based on the findings of meteorological studies, the primary interest of which was not in the building design but in the prediction of upper level boundary-layer winds. For instance, a terrain-grid of 5×5 km^2 was used by Wieringa (1986) for estimating 60 m level boundary layer wind speed. Such a large terrain-grid may have several subgrid roughness changes, which have usually been treated as grid-average roughness by using several methodologies reviewed in Grimmond and Oke (1999).

Recent studies have pointed out the significance of local, small-scale roughness changes in terrain grid of the order of 100 meters. Schmid and Bunzli (1995) pointed out that the subgrid roughness changes have significant impact on boundary layer estimation. Zhang and Zhang (2001) showed the significance of small-scale roughness changes close to the site, and suggested that terrain roughness can be assessed in a terrain-grid of 500×500 m^2, i.e. a scale of order of 100 meters, within an upstream fetch of 2 km. In fact the limited range of patch influence to wind above site has been tackled by a number of studies that attempted to define the upwind limit of the pertinent length influential to the site. For instance, the full-scale investigations of Tamura et al (2001b) implied that the

pertinent fetch length may be of the order of 1 km. AS/NZS 1170.2 (2002) suggests that an upstream fetch of 1 to 4 km is considered significant, but dependent on the building height of interest; for lower buildings ($h < 50$ m), a 1 km upstream fetch may be adequate for exposure classification.

The present study has carried out an extensive series of wind tunnel experiments to investigate the speed profile variation for cases of upstream fetch with roughness changes. Since previous modeling efforts on inhomogeneous terrain were mainly made by numerical simulation, this study has also attempted a numerical simulation to ensure that the wind tunnel findings could be better than the numerical results. Local, small-scale terrain effects were paid particular attention in the investigations.

Based on the wind tunnel data, this study proposes a simple-formed model (Wang and Stathopoulos 2005a, 2005b) and compares its output with the other modeling results as well as with a limited amount of full-scale findings (Bradley 1968; Tamura et al 2001b).

5.2 The proposed speed model

5.2.1 General description

This study takes the length of a pertinent fetch as constant (4 km) after considering the research findings of Zhang and Zhang (2001), Tamura et al (2001b) and the provisions of AS/NZS 1170.2 (2002). Results of the investigations of the variation of speed profile above fetch with small-scale roughness changes may be described starting with a single patch. A patch may be described by three parameters: length, characteristic value of roughness, and distance to the site. A patch may influence a corresponding segment of a speed profile above the site, but not the site speed profile in its entirety.

A fetch may have isolated patch(es) with negligible effects on the speed profile at the site. A fetch section may be packed with a number of small separate or joined patches, which may have an integrated effect on the speed profile. Such configurations may be utilized to simplify the calculations.

If the effects of a number of patches are independent from one another, the patches may stratify the boundary layer regime into an outer sub-layer or a set of corresponding Internal Boundary Layers (IBL's). The IBL depth growth $g(x)$ may be modeled by a 0.8 power law; as per Elliot, and Wood (Garratt 1990) as follows (i.e. Eq. (2.13)),

$$g(x) \propto z_{o,r}^{0.2} x^{0.8} \tag{5.1}$$

where $z_{o,r}$ is greater of an upstream patch roughness length or its adjacent downstream patch roughness length; x is the distance from the change of roughness to the site.

Each segment in the speed profile is dictated by the power law index of the corresponding patch. Fig. 5.1 shows an example that may better illustrate this model.

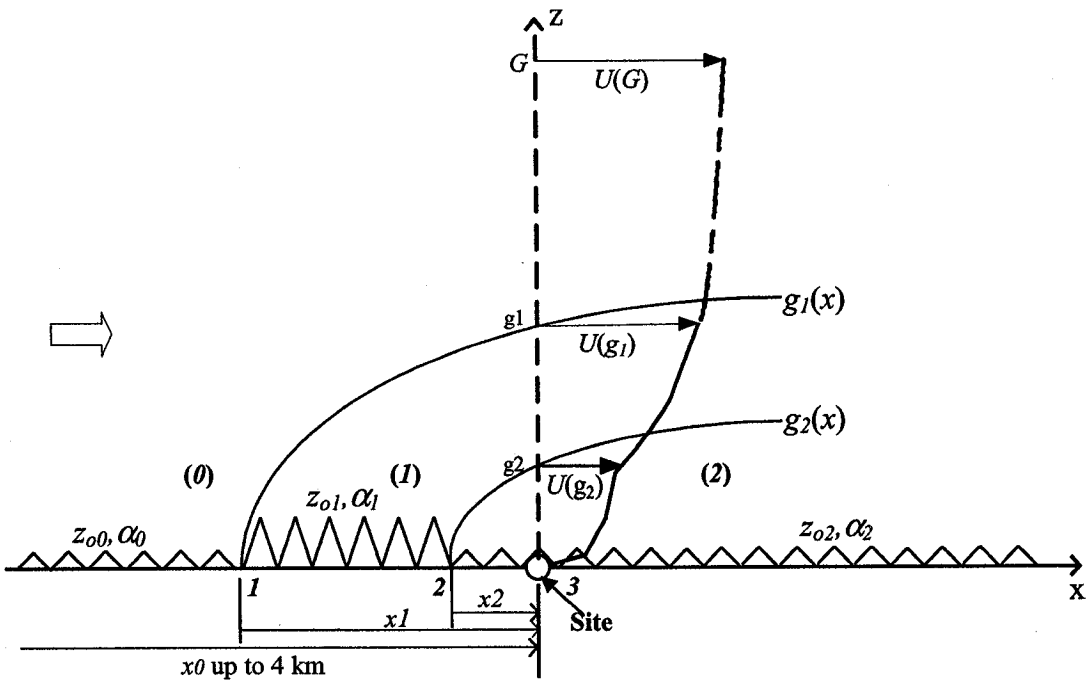

Fig. 5.1. Schematic boundary layer with two IBL's developing above a fetch with two roughness changes.

This example has a pertinent fetch of three patches: patch 0 from the 4 km upwind location to the first roughness change location 1; patch 1 from roughness change location 1 to 2; and patch 2 from roughness change location 2 to the site. The entire boundary layer is correspondingly stratified into three sub-layers: outer sub-layer (*0*) in the height range from G down to $g_1(x)$, IBL (*1*) from $g_1(x)$ down to $g_2(x)$, and IBL (*2*) from $g_2(x)$ down to the ground. Both $g_1(x)$ and $g_2(x)$ may be modeled with the 0.8 power law Eq. (5.1). The layer depths $g_1(x)$ and $g_2(x)$ break the speed profile at the site into three segments, each of which can be modeled by power-law equation with the patch-respective power-law indices α_0, α_1 and α_2.

5.2.2 The model

The proposed speed model has the form:

Gradient height:

$$g_n(x) = G \qquad (n = 0) \tag{5.2}$$

IBL depth:

$$g_n(x) = 0.5 z_{o,(n,n-1)}^{0.2} x_n^{0.8} \quad (n = 1, 2, \ldots, N) \tag{5.3}$$

Speed profile segment:

$$U(z) = U(g_n(x)) \left(\frac{z}{z_{g_n}} \right)^{\alpha_n} \qquad (g_{n+1} < z \leq g_n;\ n = 0, 1, \ldots, N;\ g_{N+1} = 0) \tag{5.4}$$

in which the subscript n denotes the patch number, i.e. patch N is the patch of the site; $g_o(x)$ denotes the gradient height; $g_n(x)$ denotes the depth of the n^{th} IBL; x_n is the distance from the n^{th} roughness change to the site; $z_{o,n}$ and α_n are roughness characteristic values of patch n; and $z_{o,(n,n-1)} = z_{o,n-1}$ or $z_{o,n}$, whichever is larger. For homogeneous terrain of no roughness change, $N = 0$, Eq. (5.3) does not apply and Eq. (5.4) reduces to the ordinary power law.

In order to use Eqs. (5.2) – (5.4), the boundary conditions need to be specified for the pertinent fetch length, the patch information (x_n, $z_{o,n}$, α_n), the gradient height G, and the gradient wind speed $U(G)$. In this study, the pertinent fetch length is assumed as constant 4 km. Patch roughness information (x_n, $z_{o,n}$, α_n), and the gradient height G for the pertinent fetch can be found in Table 5.1 after Davenport et al (2000) and ASCE (1999). The highest roughness grade (Class 8, Chaotic, $z_o > 2$ m) of the original classification (Davenport et al 2000) is combined within Urban (Closed) in compliance with ASCE 7-02. Little ambiguity should exist in using Table 5.1; however if indeed so, smaller values

of $z_{o,n}$, α_n and/or G will be conservative from the structural safety point of view. Values of $U(G)$ have already been available in wind standards and codes of practice.

Table 5.1. The present roughness classification after Davenport et al (2000) with power law α values after ASCE (1999).

Roughness Class	z_o [m]	α	G [m]
1. Sea	0.0002	*0.09*	213
2. Smooth	0.005	*0.125*	213
3. OC	0.03	0.15	274
4. Roughly open	0.1	*0.2*	274
5. Suburban (Rough)	0.25	0.25	366
6. Very rough	0.5	*0.3*	366
7. Urban (Closed)	1	0.33	366

Number in *italics* is obtained by best fit of data.

5.3 Discussion

5.3.1 Application of the model

The proposed speed model is compared with the present wind tunnel data, the ESDU (82026) model, the present numerical model and/or limited full-scale data. Except for the model application to the ESDU example, the boundary conditions (G, $U(G)$, $z_{o,n}$ and α_n) used in this section were best-fit from the wind tunnel data for all cases considered in this study.

Figure 5.2 shows the speed profile results for the typical OC, Suburban and Urban homogeneous terrain. Clearly the proposed model agrees well with the wind tunnel data, as well as with the full-scale measurements conducted by Tamura et al (2001b) for OC and suburban cases in two sites, one of which located at seashore, the other 4 km downwind on a dense suburban fetch section. In the model application, Eq. (5.2) turns out to yield $g_o(x)$ = 240 m, and since N = 0, i.e. no roughness change, Eq. (5.3) is not applicable and the final speed profiles of each of the terrain cases are calculated by using

Eq. (5.4) with the case-respective $U(G)$ and α values. With the exception of the OC exposure, ESDU (82026) seems to yield somewhat larger, i.e. more conservative, speed profiles.

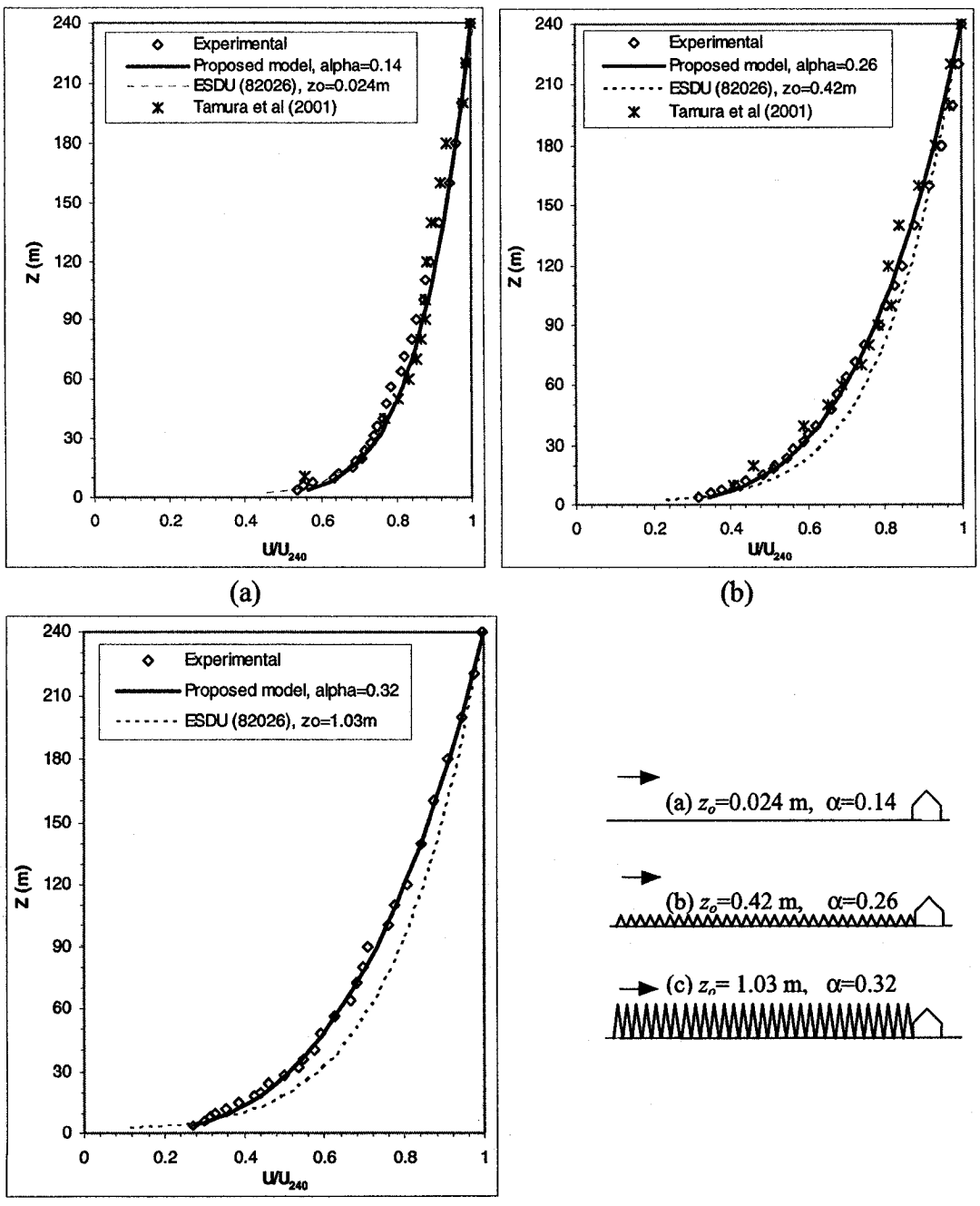

Fig. 5.2. The test speed profiles measured above turntable in: (a) OC, (b) Suburban, and (c) Urban.

It would be of interest to demonstrate how the proposed model fits the actual ESDU (82026) values for a case of inhomogeneous upstream terrain. The example provided in the ESDU document was deemed the most appropriate case to check.

The ESDU (82026) example requires to find the mean speed profile at a site downwind of two changes in surface roughness, given the reference speed $U(10) = 22$ m/s, and the fetch containing three patches, as shown in Fig. 5.3. ESDU (82026) appears to take a lot more steps than the proposed model in speed profile calculation. It is worth noting that the probability factor, which is taken into account by the original ESDU (82026) data, has been removed in the comparison of Fig. 5.3, which shows that the agreement between the proposed model and ESDU (82026) is reasonable, particularly below 20 m and above 80 m. For intermediate heights, ESDU tends to provide higher values than the proposed model, which thus appears less conservative than ESDU (82026). However, the proposed model agrees better with the full-scale investigation of Letchford et al (2001) on a geometrically similar fetch configuration under hurricane conditions; Letchford et al (2001) found that the ESDU (82026) transitional model may tend to overestimate, as much as around 20%, the increase in speed at 10 m height induced by an R-S roughness change. It is also noteworthy that this particular case ensures conditions of neutral atmospheric stability considering the high wind speeds it refers to.

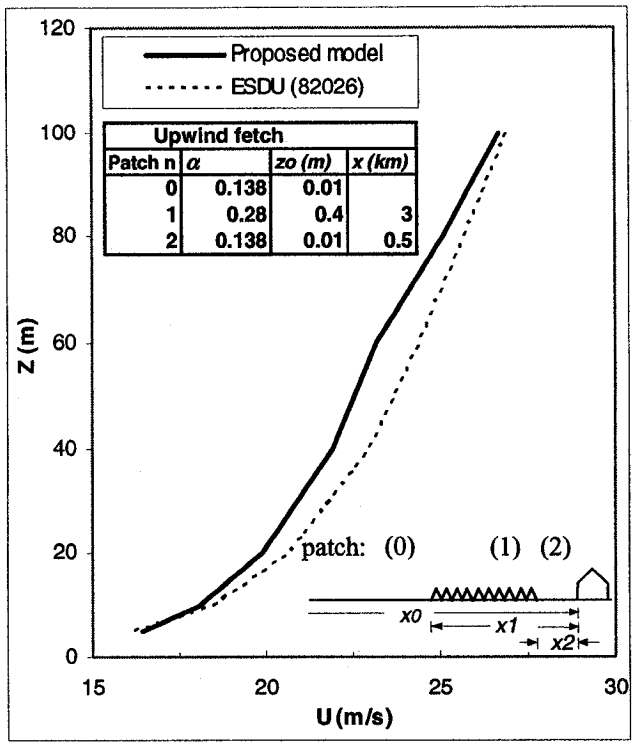

Fig. 5.3. The proposed speed model and the ESDU (82026) model for the same ESDU (82026) example.

Figure 5.4 shows comparative data for the case with a fetch of two roughness changes. In fact the exposure is mainly typical of OC with an interrupting Urban-type patch, 375 m long, starting at about 250 m upstream of the site. The proposed model assumes the pertinent fetch length is 4 km, $G = 240$ m, and $U(G) = 13.2$ m/s. Eqs. (5.2) - (5.4) are used as follows: first carrying $G = 240$ m into Eq. (5.2), $g_o(x) = 240$ m; then plugging $x_1 = 625$ m and $z_{o(1,0)} = 1.03$ m (the larger of $z_{o0} = 0.024$ m and $z_{o1} = 1.03$ m) into Eq. (5.3), $g_1(x) \approx 80$ m; and in the same manner, $g_2(x) \approx 28$ m. Plugging the values $U(G) = 13.2$ m/s, $\alpha_o = 0.14$, $g_o = 240$ m, $\alpha_1 = 0.32$, $g_1 = 80$ m, $\alpha_2 = 0.14$, $g_2 = 28$ m and $g_{2+1} = 0$ into Eq. (5.4), the speed profile plotted in Fig. 5.4 is obtained. Also compared in this figure are the present numerical model and the ESDU (82026) model results.

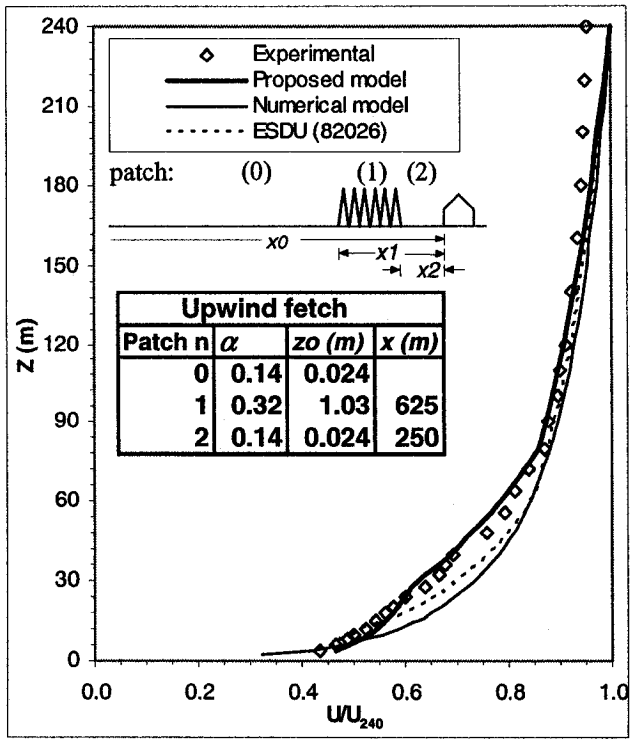

Fig. 5.4. The proposed speed model, the present wind tunnel data and the ESDU (82026) model for a fetch of two roughness changes.

The procedure of the application of the ESDU (82026) model for Fig. 5.4 may be summarized as follows: (a) calculate the speed profiles respective to patches 0, 1 and 2; (b) calculate the speed-profile modification factors respective to patches 1 and 2, in terms of patch z_o, u_* values and the distances from each of the roughness changes to the site; (c) draw the speed profile for patch 0, as well as draw the speed profiles for patches 1 and 2 with the respective modification factors; and (d) tailor the three speed profiles into one continuous profile.

It is found in Fig. 5.4 that the proposed model matches well with the wind tunnel data, whereas the present numerical model matches well with the ESDU (82026) model. The difference of the proposed model from the ESDU (82026) model is regarded similar with

the characteristic difference of power law from log law for a homogeneous upstream terrain configuration.

The calculation experience for the case in Fig. 5.4 has also revealed that the application of the proposed model is easier than that of the ESDU (82026) model.

Fig 5.5 shows terrain configurations of general Suburban form with a number of OC patches at various distances from the site. Figure 5.5a shows the case with a fetch of three roughness changes, while Fig. 5.5b refers to a more extreme case with eight upstream roughness cases. Wind tunnel data, the proposed model, and the numerical results have been included in both cases. However, the ESDU model has not been applied in the latter case (Fig. 5.5b) because the actual process is rather cumbersome for this upstream configuration, since as per ESDU *"this procedure can obviously be extended to even more roughness changes but it is unlikely that more than three roughness changes will be considered"*. In contrast, it is found that the proposed model remains easy to apply for a fetch of more than three roughness changes as well.

Clearly, Fig. 5.5a shows the proposed model matches well with the wind tunnel data, whereas the present numerical model matches well with the ESDU (82026) model. Figure 5.5b also shows that the proposed model agrees well with the wind tunnel data for this complex fetch configuration. It is worth mentioning that in this case, it has also been attempted to average the short patches upstream and near the model into an effective equivalent patch by using Eq. (2.12), i.e. the Lettau's (1969) model, with satisfactory results.

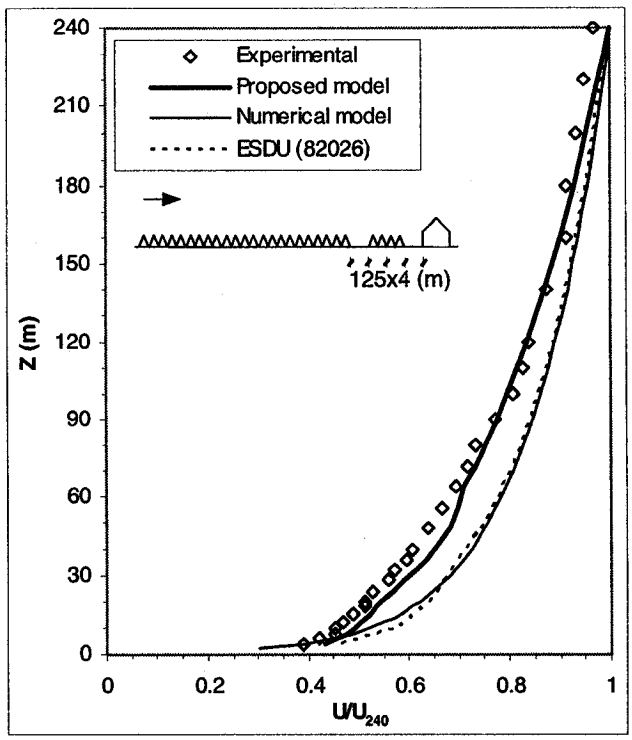

(a)

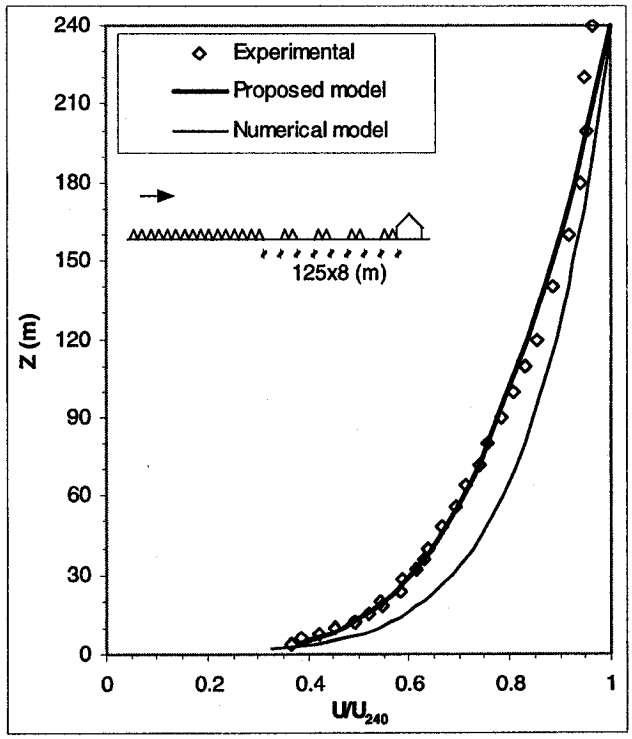

(b)

Fig. 5.5. The proposed speed model, the present wind tunnel data, the ESDU (82026) model, and/or the present numerical model for (a) a fetch of three roughness changes, and (b) a fetch of eight roughness changes.

Generally speaking, the results of a number of typical fetch cases examined show satisfactory performance of the proposed model that demonstrates appropriate curvature response to roughness changes. The proposed model has a simple form compatible with both homogeneous and inhomogeneous fetch configurations. It can also be easily applied for fetch of multiple small-scale roughness changes. As a matter of fact, Cook (1997) has presented good agreement of the power law, which is the simplest form of the proposed speed model, with the ESDU (82026) equilibrium speed model, at least for smooth terrain conditions. On the other hand, the proposed model agrees better with field investigations (Letchford et al 2001) than the ESDU (82026) model.

5.3.2 Validation of the model

Notwithstanding the limited number of full-scale studies of wind speed profiles, particularly above inhomogeneous terrains, full-scale data of Bradley (1968) were used to validate the proposed wind speed model. These data can at least be used to examine the difference found in the proposed model from the ESDU (82026) model.

Figures 5.6 and 5.7 show the model comparisons against the data of Bradley (1968). These full-scale data were measured within 3 meters above ground. Regarding upstream fetch, the smoother patch was tarmac with z_{01} = 0.00002m (which could be translated into $\alpha \approx 0.08$), and the rougher patch was spikes with z_{02} = 0.0025m ($\alpha \approx 0.12$). Both surfaces were aerodynamically on the smooth side. The proposed speed model shares this power-law feature and matches better with the full-scale data than the ESDU (82026) model. The strong power law feature of this model is also in good agreement with the full-scale speed profile measured in Tamura et al (2001b), as mentioned previously.

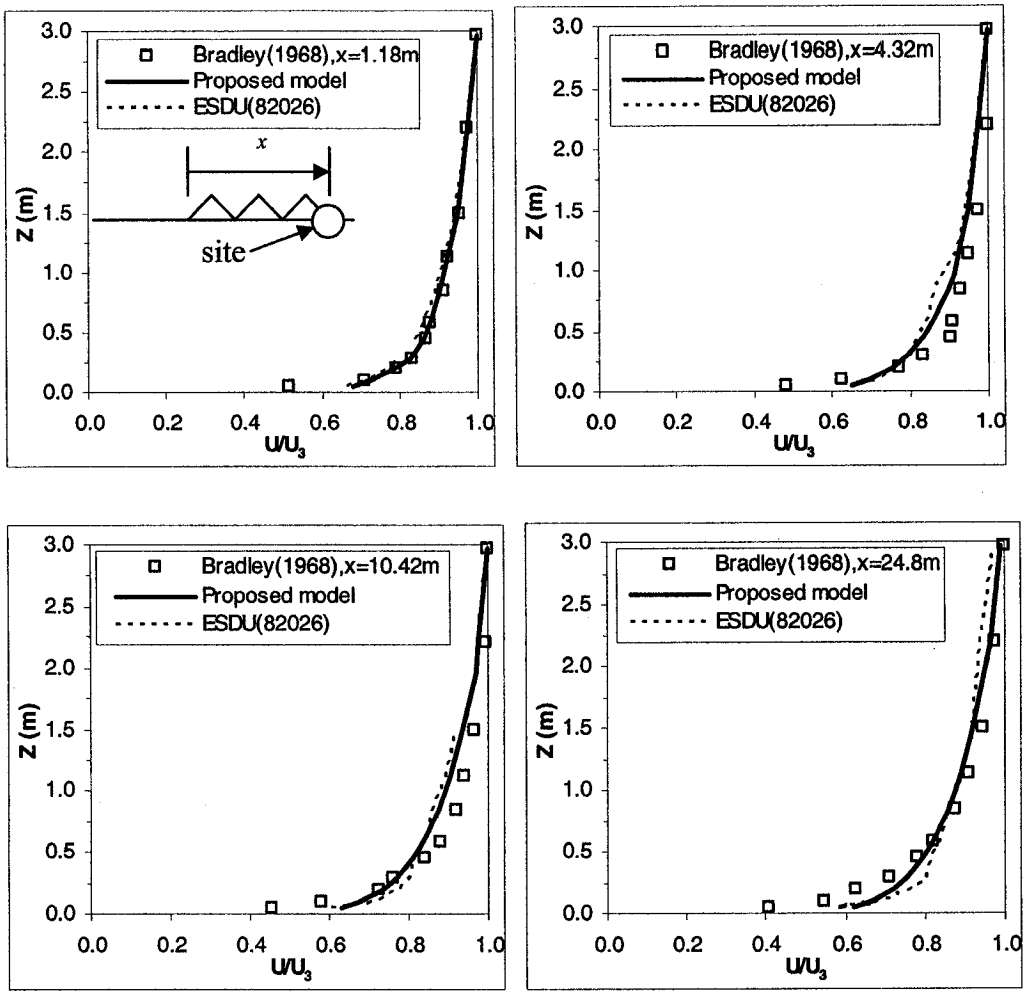

Fig. 5.6. The proposed speed model, the ESDU (82026) model and Bradley (1968) data for a fetch with single roughness change from smoother (tarmac, $z_{o1} = 0.00002$ m, $\alpha \approx 0.08$) to rougher (spikes, $z_{o2} = 0.0025$ m, $\alpha \approx 0.12$).

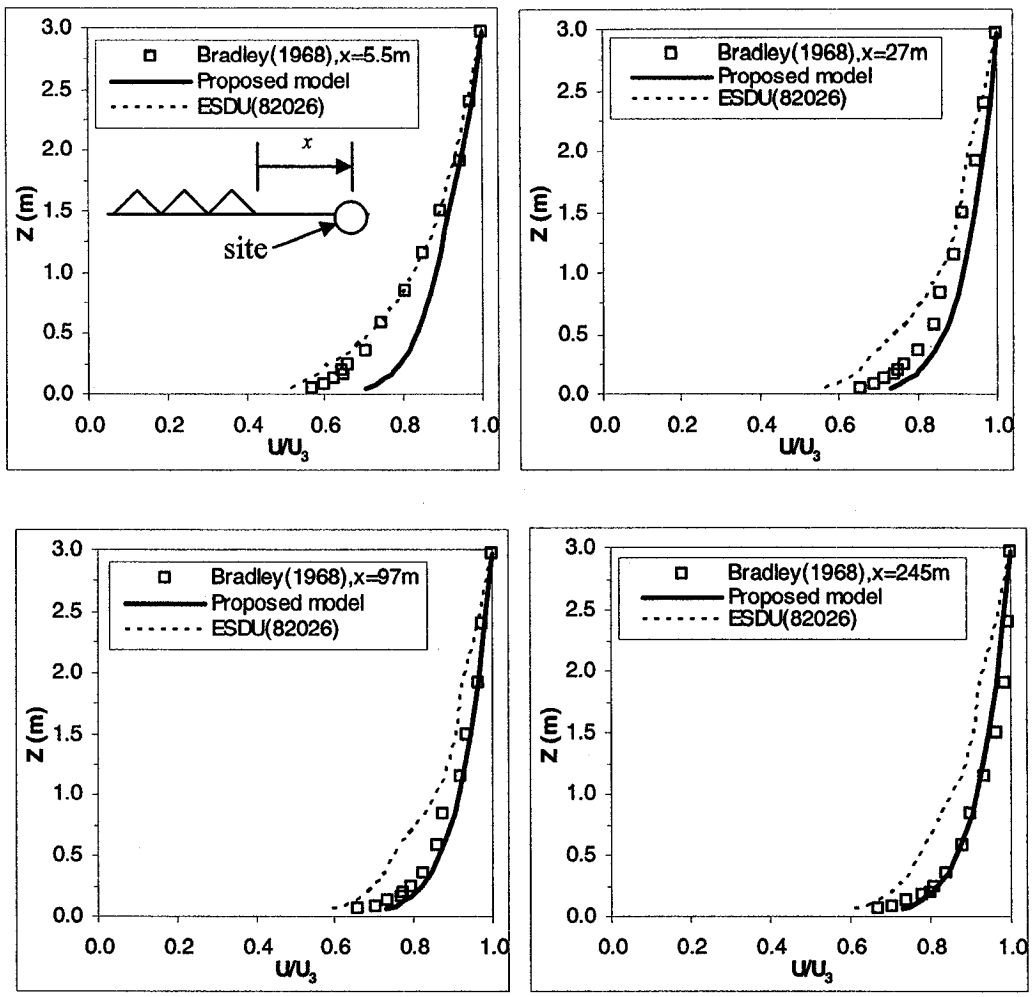

Fig. 5.7. The proposed speed model, the ESDU (82026) model and Bradley (1968) data for a fetch with single roughness change from rougher (grass, $z_{o1} = 0.005$ m, $\alpha \approx 0.125$) to smoother (tarmac, $z_{o2} = 0.00002$ m, $\alpha \approx 0.08$).

Figure 5.6 refers to the so-called S-R roughness change. The data show that as far as the profile curvature response to a roughness change is concerned, the proposed model has a larger curvature than the ESDU model and, in general, fits the field data well. However, the results presented in Fig. 5.7 refer to an R-S case and the model still works well except for the case with a small patch 5.5 m long just upstream the site location. In all other cases the proposed model performs actually better than the ESDU (82026) model. Naturally, the available full-scale results, which covered the boundary layer only

in the lowest 3 m above ground, may not be sufficient to yield a definite conclusion. However, Figs. 5.6 and 5.7 show that the proposed speed model is also applicable to very smooth terrain and very low elevation (note the small magnitudes of z_o and α values in Figs. 5.6 and 5.7).

Generally speaking, the proposed model has the power law form, which is compatible with the power law adopted by ASCE 7-02 for homogeneous terrain. It is also worth noting that this model is based on both wind tunnel and full-scale data, whereas the ESDU (82026) transitional model is the result of numerical evaluations.

ASCE 7-02 classifies terrain in three grades, i.e. Coastal, OC, and Suburban-Urban. On the other hand, the modified roughness classification in Table 5.1 appears to have much more support from experimental evidence. The present study has found that the proposed model is easy to apply for various terrain classifications without any particular difficulty. Therefore, the introduction of the terrain roughness classification (Table 5.1) after Davenport et al (2000) via the present model efforts is expected to improve the accuracy in design speed profile estimation.

5.4 Conclusion

A wind speed model has been proposed for the description of upstream terrain exposures for better design wind loading estimations. The model is based on wind speed data obtained in an extensive wind tunnel study dealing with a variety of upstream exposure configurations both homogeneous and inhomogeneous in nature. The model uses N sections corresponding to N different roughness patches, in the upstream terrain within a range no more than 4 km from the site. Recognition of patch type and patch roughness

information (z_o and α) can be referenced to a roughness classification after Davenport et al (2000). The proposed speed model is simple and easy to apply for fetch with multiple roughness changes. Its validation has been attempted by using the limited available field data with satisfactory results. The proposed model may be helpful for future code development.

Chapter 6 Turbulence intensity results and discussion

6.1 Introduction

The wind tunnel experimental data that are used to develop the speed model in the preceding chapter have also provided an opportunity for finding a model estimating turbulence intensity, $Iu = u(z)/U(z)$, in which u = standard deviation of fluctuating velocity.

For homogeneous terrain, a number of models have been suggested in ESDU (82026), Simiu and Scanlan (1996), AIJ (1996), ASCE 7-02, and Zhou and Kareem (2002). The ESDU (82026) model is essentially an empirical curve fitting. Simiu and Scanlan (1996) provided an inverse log law equation, and Zhou and Kareem (2002) proposed an inverse power law equation. On the other hand, few studies were found in the literature for inhomogeneous terrain, the most significant one perhaps was Deaves (1981a), which furnished the numerical results that were formulated into the ESDU (84030) standard datasets for typical inhomogeneous terrain cases.

This study mainly intends to develop an *Iu* model for fetch with roughness changes, since there might not be any practically useful model on this regard, although Deaves (1981) and ESDU (84030) have attempted with limited success. In general, the *Iu* model proposed can apply for both homogeneous and inhomogeneous terrain.

This chapter describes this *Iu* model (cf. Wang and Stathopoulos 2005a), and discusses the model application and compares this model with other results.

6.2 The proposed *Iu* model

6.2.1 General description

The pertinent fetch length of 4 km and the gradient conditions, which have been provided for the speed model (Table 5.1), are considered effective for the *Iu* modeling. It is worth noting that Letchford et al (2001) pointed out that wind-tunnel observations showed that turbulence takes a shorter fetch to 'forget' the upwind patch influence than does mean wind speed.

This study found that the present wind tunnel data can be characterized well by a generalized (inverse) power law. In modeling *Iu* above inhomogeneous terrain, it is known that terrain roughness changes can induce the subdivision of boundary layer into IBL('s) and an outer layer, and the IBL depth growth $g(x)$ obey Eq. (5.1). These are the same as those found in the present speed modeling. What appears more complicated in the *Iu* modeling is that an IBL will further subdivide into two sublayers: a transitional sublayer and an equilibrium sublayer. The depth of the equilibrium sublayer, $g'(x)$, can be predicted by $g'(x) \propto z_{o,r}^{0.2} x^{0.72}$ and $g'(x) \propto z_{o,r}^{0.2} x^{0.4}$, respective to a smooth-to-rough (S-R), and a rough-to-smooth (R-S) roughness change. The present 0.72 power law and 0.4 power law are comparable to the findings of Antonia and Luxton (1971 and 1972), which are the 0.79 power law and 0.43 power law, respective to S-R and R-S change (Eqs. (2.14) and (2.15)). Since the depth growths of the different sublayers may follow power law of different alphas, i.e., 0.8, 0.72 and 0.4, the boundaries of the sublayers may meet each other, the sublayers can collectively form a 'mixing layer'. In the end, a boundary layer subdivides into outer layer, transitional sublayer, equilibrium sublayer and 'mixing layer' in the *Iu* modeling above inhomogeneous terrain.

In the equilibrium sublayer or outer layer, the *Iu* profile segment may be predicted by a -0.4 power law with the patch-characteristic $Iu(10)$ value, and in the transitional and/or 'mixing layer', the *Iu* profile segments appear as line shape, which connect through to form a continuous *Iu* profile.

The present modeling may be illustrated in Fig. 6.1. Above the pertinent fetch, there are three patches: patch 0 from the 4 km upstream location to the first roughness change location 1, patch 1 from roughness change location 1 to 2, and patch 2 from roughness change location 2 to the site. Respecting these three patches are three layers: the outer layer (*0*) delimited from $g_o'(x)$ (= G) to $g_1(x)$, the IBL (*1*) from $g_1(x)$ to $g_2(x)$, and the IBL (*2*) from $g_2(x)$ to ground level; both $g_1(x)$ and $g_2(x)$ obey the 0.8 power law (Eq. (5.1)). The IBL (*1*) is broken down into a transitional sub-layer and the equilibrium sub-layer (denoted by *1'*), separated by $g_1'(x)$ that obeys the 0.72 power law (S-R). The IBL (*2*) is broken down into the transitional sub-layer and the equilibrium sub-layer (*2'*), separated by $g_2'(x)$ that obeys the 0.4 power law (R-S). Correspondingly, the *Iu* profile has three power-law segments: one from $Iu(g_o')$ to $Iu(g_1)$, another from $Iu(g_1')$ to $Iu(g_2)$, and the last from $Iu(g_2')$ to the ground, each of which obeys the -0.4 power law specified with the patch-respective $Iu_o(10)$, $Iu_1(10)$, $Iu_2(10)$. The line segments connect through to form the final *Iu* profile.

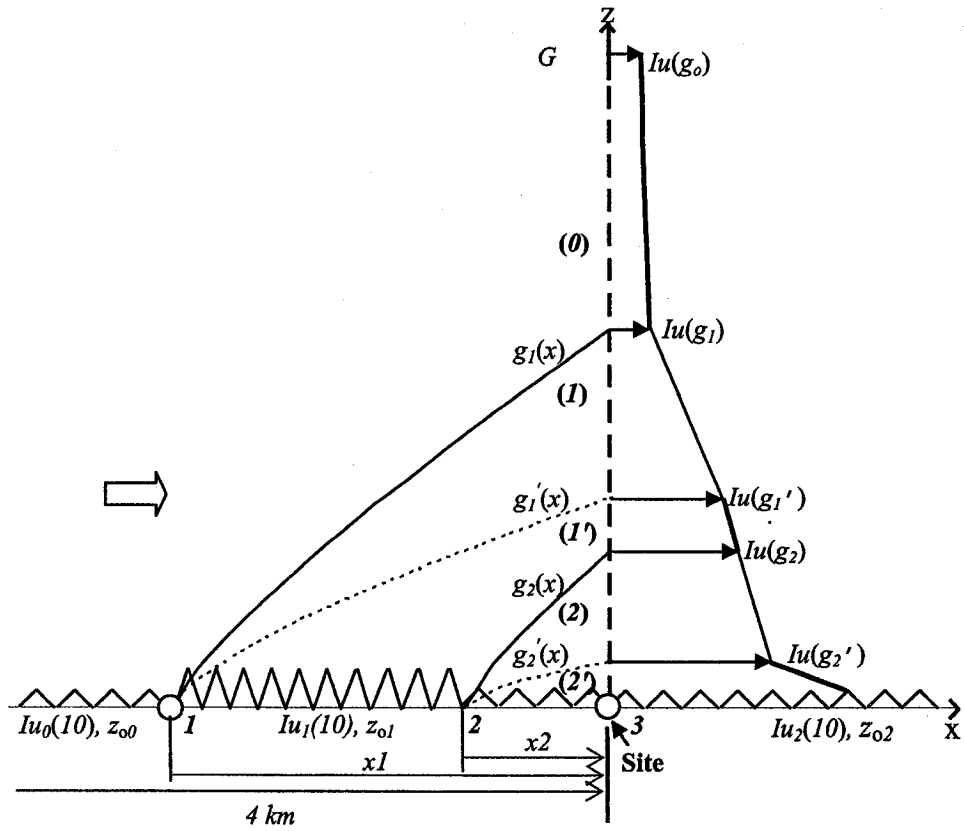

Fig. 6.1. Illustrative Iu profile developing above a fetch with two roughness changes.

6.2.2 The model

The proposed *Iu* model has the following form,

Gradient height:

$$g_n'(x) = G \qquad (n = 0) \tag{6.1}$$

IBL total depth:

$$g_n(x) = 0.5 z_{o,(n,n-1)}^{0.2} x_n^{0.8} \qquad (n = 1, 2, \ldots, N) \tag{6.2}$$

IBL equilibrium sub-layer depth:

$$g_n'(x) = 0.5 z_{o,(n-1,n)}^{0.2} x_n^{0.72} \quad (\text{if } z_{o,n-1} < z_{o,n};\ n = 1, 2, \ldots, N) \quad \text{S-R} \tag{6.3a}$$

$$g_n'(x) = 0.5 z_{o,(n-1,n)}^{0.2} x_n^{0.4} \quad (\text{if } z_{o,n-1} > z_{o,n};\ n = 1, 2, \ldots, N) \quad \text{R-S} \tag{6.3b}$$

Iu profile:

$$Iu(z) = Iu_n(10)\left(\frac{z}{10}\right)^{-0.4} \quad (g_{n+1} \le z \le g_n';\ n = 0, 1, \ldots, N;\ g_{N+1}=0) \tag{6.4}$$

$$Iu(z) = Iu(g_n) + \frac{(z - g_n)}{(g_n' - g_n)}(Iu(g_n') - Iu(g_n)) \quad (g_n' < z < g_n;\ n = 1, 2, \ldots, N) \tag{6.5}$$

where the subscript n denotes the patch number, and patch 0 is the patch from 4 km to the first roughness change, and patch N is the patch of the site; $g_o'(x)$ denotes the gradient height; $g_n(x)$ denotes the total depth of the n^{th} IBL; $g_n'(x)$ denotes the depth of the n^{th} equilibrium sub-layer; $z_{o,n}$ is the characteristic z_o of patch n; and $z_{o,(n,n-1)} = z_{o,n-1}$ or $z_{o,n}$, whichever is larger; x is the distance from the n^{th} roughness change to the site. For homogeneous terrain, $N = 0$, and this model reduces to be Eqs. (6.1) and (6.4).

The only information that we need to add is $Iu_n(10)$ that can be provided from Table 6.1, besides the natural boundary conditions that can be found in Table 5.1.

Table 6.1. $Iu(10)$ values of this study and ASCE (1999) for homogeneous terrain.

	Very smooth	Open	Suburban	Urban
Present	-	0.17 (α=0.14)	0.28 (α=0.26)	0.35 (α=0.32)
ASCE (1999)	0.092 (α=0.09)	0.172 (α=0.14)	0.271 (α=0.22)	0.434 (α=0.33)

6.3 Discussion

Application of the model may follow such a procedure. Draw the fetch diagram, simplify the fetch diagram if possible, then label the necessary conditions ($Iu(10)$, z_o, x, and/or G) by Tables 5.1 and 6.1, and finally apply the Iu model. In the application, for inhomogeneous terrain, (a) use Eqs. (6.1) - (6.3) to subdivide the boundary layer, (b) apply Eq. (6.4) for outer layer and/or equilibrium sub-layer, and (c) apply Eq. (6.5) for transitional sub-layer and/or mixing sub-layer. For homogeneous terrain, this is just to apply Eq. (6.4) for the entire boundary layer.

The following two cases intend to show the characteristics of the Iu model, and attempt to make model justification. In these two cases, the boundary condition G comes from wind-tunnel measurements, i.e., G is simply assumed as 240 m; this value does not reference to Table 5.1.

Figures 6.2a and 6.2b show the features of the Iu model by comparing this model with the present wind-tunnel Iu data, and with previous full-scale data (Cermak and Cochran 1992; Kato et al 1992; Tieleman 1996; Schroeder et al 1998; and Baker 2004), as well as with previous models (ESDU 82026; AIJ 1996; AS/NZS 2002; and ASCE 7-02). Figure 6.2b shows the lower part of Fig. 6.2a.

Agreement of the proposed Iu model with those limited full-scale data is reasonably good for homogeneous terrain conditions. Figures 6.2a and 6.2b show that, for OC, both

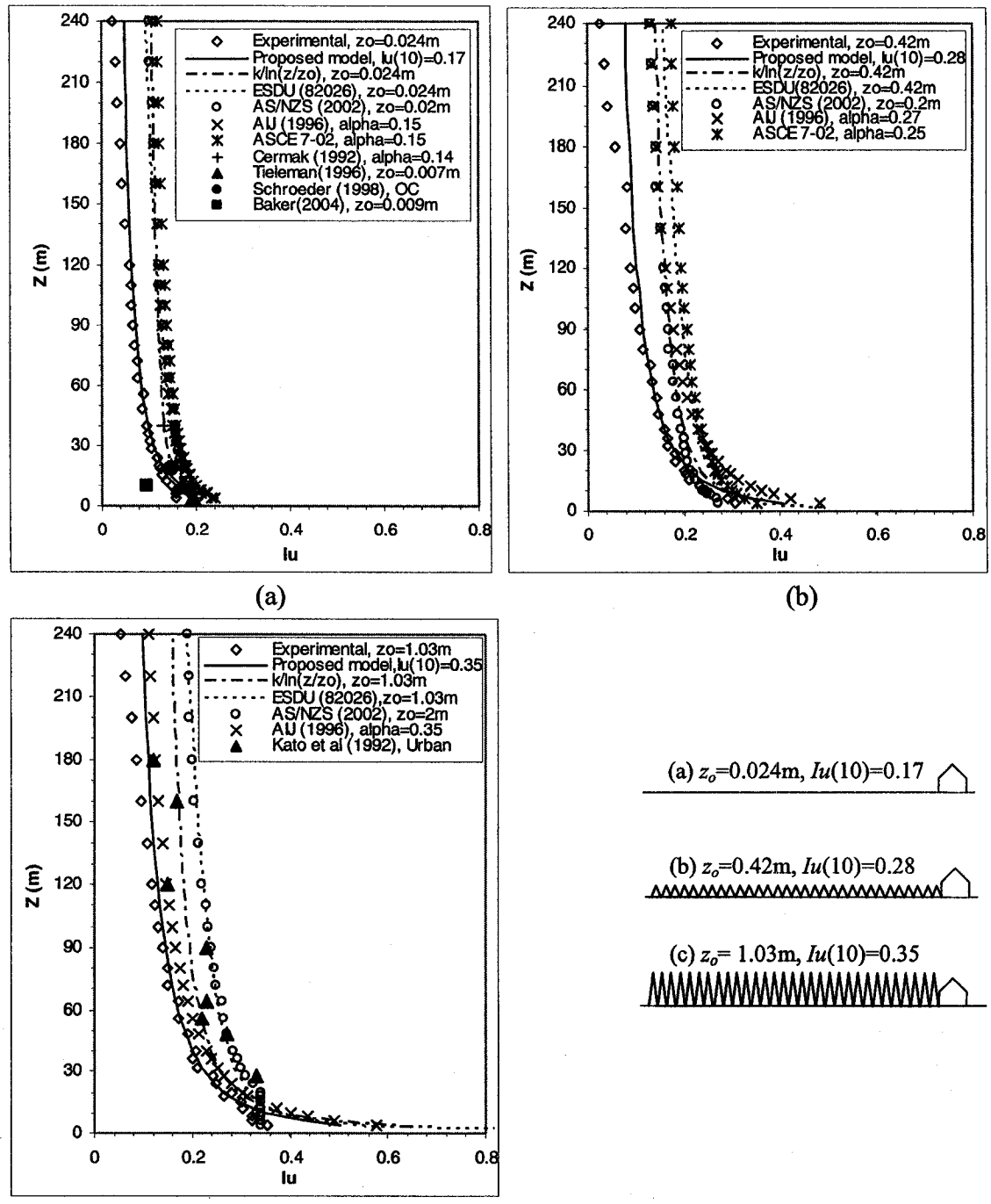

Fig. 6.2a. Wind-tunnel and model Iu profiles above (a) OC, (b) Suburban, and (c) Urban.

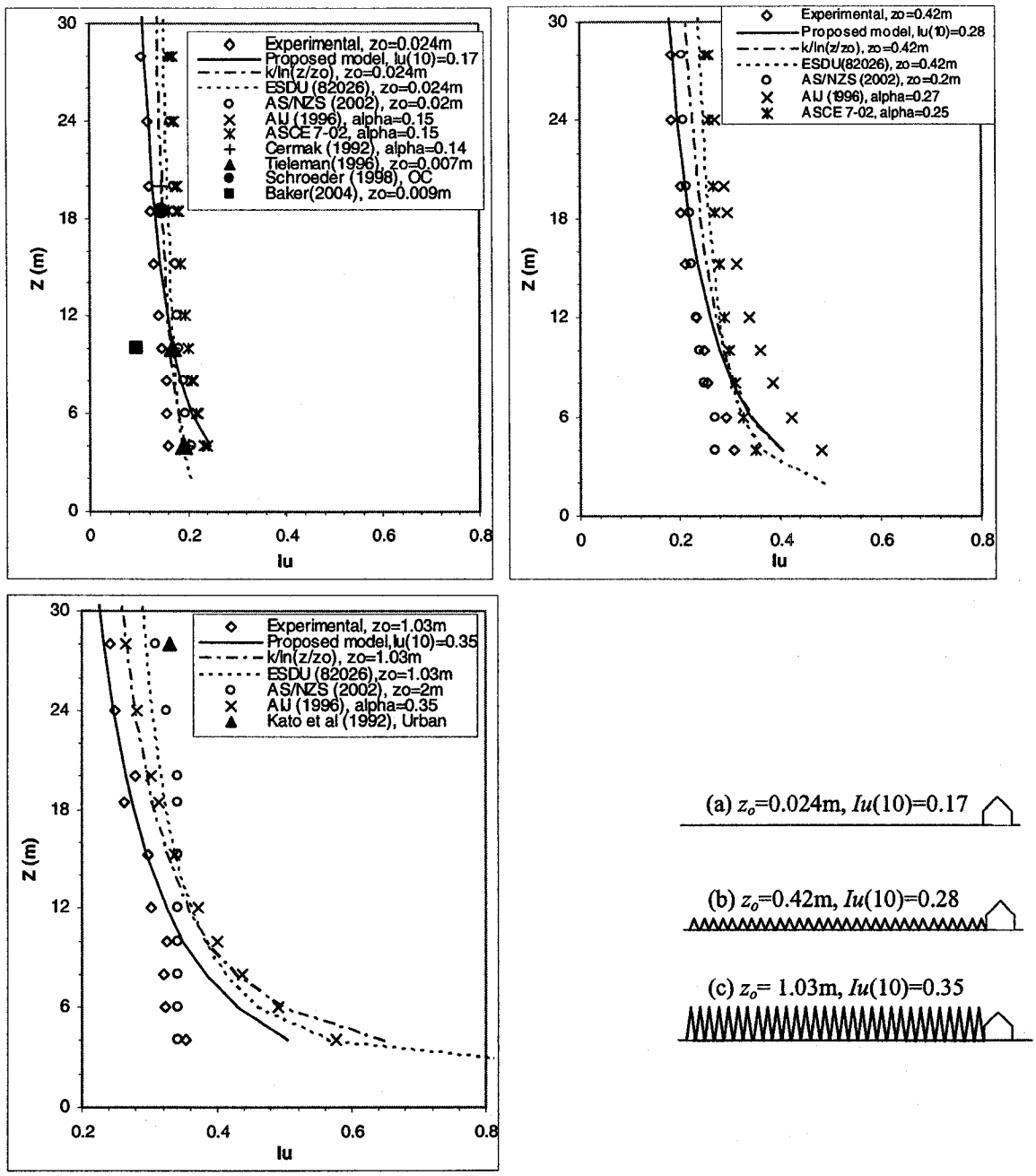

Fig. 6.2b. Wind-tunnel and model Iu profiles above (a) OC, (b) Suburban, and (c) Urban (presented for elevation in the range from 0 to 30 m).

this *Iu* model and the present wind-tunnel data compare well with data of Tieleman (1996), Schroeder et al (1998), and Baker (2004), although the terrain z_0 value of Baker (2004) and that of Tieleman (1996) appear lower. Data values of Cermak and Cochran (1992) are slightly higher than the present findings. For the Urban case, both this *Iu*

model and the present wind-tunnel data compare reasonably well with data of Kato et al (1992) who collected the *Iu* data in Tokyo city supposedly much rougher. Furthermore, both Fig. 6.2a and Table 6.1 show that the proposed *Iu* model may yield lower values than the previous models. However, this can be easily adjusted by a simple modification of the terrain-respective *Iu*(10) value. Since the full-scale data are not sufficient, no conclusion can be reached presently whether the terrain-respective *Iu*(10) values should be really increased.

Figure 6.3 shows a specific case of the fetch of two roughness changes; this typical example shows that the proposed *Iu* model fits well with the present wind-tunnel data.

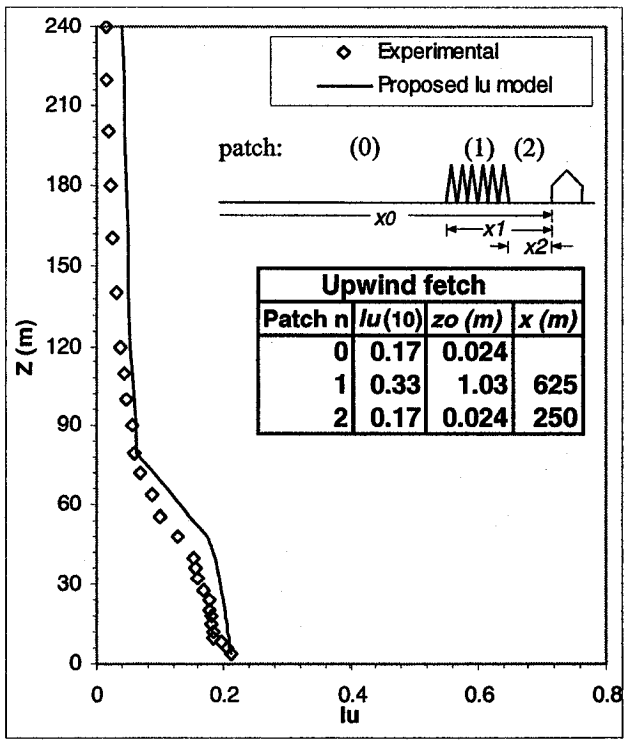

Fig. 6.3. The present wind-tunnel data and the proposed Iu model results for a fetch with two roughness changes.

Figure 6.4 shows another case for comparison with ESDU (84030). The ESDU (84030) data provisions relate to a fetch that has a roughness change from smooth

upstream terrain (z_{o0} = 0.03 m) to a 300 m long rough patch (z_{o1} = 0.3 m); in other words, the fetch in the ESDU (84030) case is very similar to that shown in Fig. 6.4, but not exactly the same.

Figure 6.4 shows that the proposed *Iu* model matches well with the wind-tunnel data, but furnishes lower values than the ESDU (84030) data provisions, especially for higher elevations. However, this data trend can be easily adjusted with the value of the exponent of the proposed *Iu* model, which is presently assumed as -0.4. Presently, such an adjustment is not made, since comparable full-scale data cannot be found. Moreover, it should be noted that few cases of the present study can be compared with those in ESDU (84030).

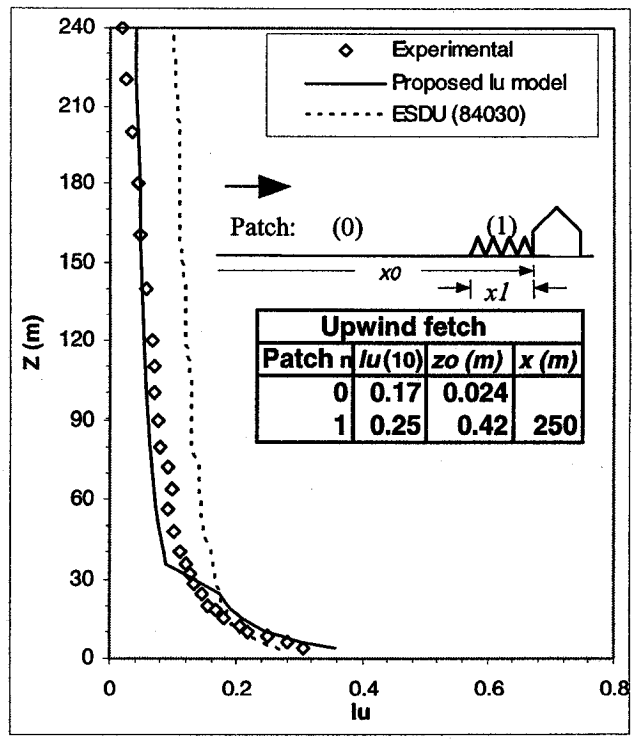

Fig. 6.4. The present wind-tunnel data, the proposed *Iu* model results for a fetch with a single (S-R) roughness change (shown in this figure), as well as the ESDU (84030) data provided for a very similar fetch.

6.4 Conclusion

A *Iu* model has been proposed for the description of upstream terrain exposures from the present wind tunnel speed measurements. The *Iu* model takes into account the same terrain information as the proposed speed model (see the preceding chapter) does, expect that this *Iu* model requires patch characteristic turbulence intensity at 10 m level, *Iu*(10), as input. The proposed model appears simpler and easier to use than the previous results. The model validation has been attempted by utilizing limited field data available; generally speaking, the present comparisons are satisfactory.

Chapter 7

Modeling the low building design wind loads above various exposures

7.1 Introduction

It is well known that low-rise building wind loads vary with upstream terrain exposure. However, the terrain-load relationship has not been well quantified, especially with terrain of roughness changes. Particularly when compared with studies on pressure coefficients, quantification of the terrain-load relationship is still an on-going research area, where one of the first studies was carried out by Hussain and Lee (1980). A full review has been presented in Chapter 2.

Past research results have been partially adopted into wind standards and codes of practice, with considerable differences from each other however. Although the code provisions commonly agree that terrains can be evaluated into a number of classes, namely, Costal, Open Country (OC), Suburban-Urban, and/or Large-City-Center, different wind standards and codes of practice give different specifications on the minimum fetch length requirement for a patch to qualify as (matured) homogeneous terrain (see Table 2.4). In addition, the design load estimated by ASCE 7-02 for above Suburban-Urban terrain is 25% less than that by ASCE 7-95 for the same type of terrain. Generally speaking, it is still needed to clarify/justify what would be the best specifications for the minimum fetch length requirement and for the Suburban exposure factor in previous studies (see more details in Chapter 2).

The present wind tunnel pressure database has provided an opportunity to tackle the above issues for better design specifications for low-rise building wind loading. The results are presented in this chapter.

7.2 Comparison with previous work

Validation of the present wind tunnel data has been made by comparison with previous studies (Stathopoulos 1979; Stathopoulos and Saathoff 1994; Case and Isyumov 1998). The agreement among these studies is reasonably good, thus the effectiveness of the present data is ascertained.

Figure 7.1 compares the *Cp mean* values measured on two roof positions in this study to two (similar) roof positions measured in Stathopoulos and Saathoff (1994). Both studies have been made on the same building model, in the same OC settings and the same wind-tunnel, but with different wind tunnel entrance settings. The board mounted with egg boxes and placed adjacent to the inlet screen in this study – see Fig. 3.2 – was not used in Stathopoulos and Saathoff (1994). The slightly higher magnitudes of the data in Stathopoulos and Saathoff (1994) can be attributed to this setting difference, since this present addition of the board should cause pressure to be slightly lower (in magnitude).

Figure 7.2 compares the most-critical *Cp* min values among Stathopoulos (1979), Case and Isyumov (1998) and this study. The present model is also the same as that used in Stathopoulos (1979), but different from that of Case and Isyumov (1998). The results of this study agree well with those of Stathopoulos (1979), but appear lower than those of Case and Isyumov (1998). The magnitude differences can be attributable

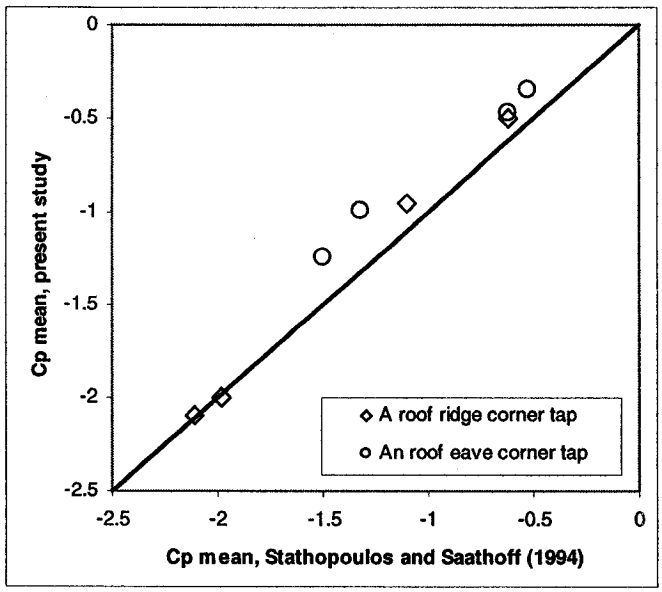

Fig. 7.1. *Cp* mean values of two taps above in OC measured by Stathopoulos and Saathoff (1994) and those by the present study, with wind azimuths $\theta = 0^{\circ}$, 45°, 90° and 135° (see θ definition with Fig. 3.12).

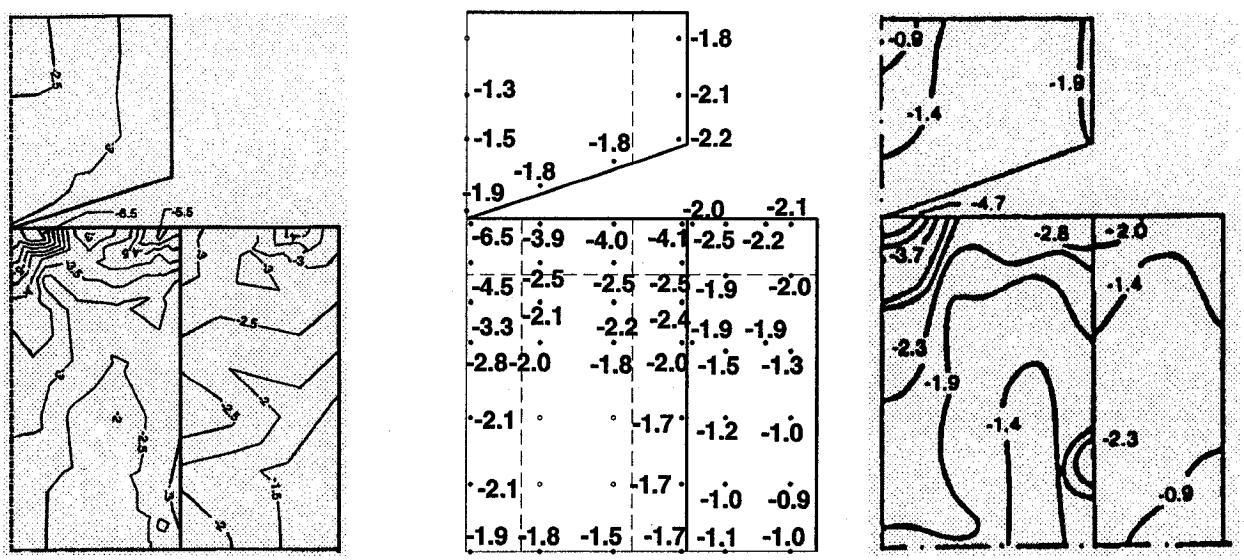

(a) (b) (c)

Fig. 7.2. Most-critical *Cp* min values measured on a 4:12 slope low building by (a) Case and Isyumov (1998), (b) the present study, and (c) Stathopoulos (1979): •: in use; and ○: dummy.

to the higher tap resolution used in Case and Isyumov (1998) for critical areas, and the scale difference, as well to the differences in boundary layer simulation and in building geometry. More discussion on the differences has also been given in Case and Isyumov (1998). It should be noted that the extreme value analysis Method 2 (i.e. Gumbel plot, see Chapter 3) is used for calculating those outstandingly larger (roof corner) local *Cp* min results, and the extreme value analysis Method 1 (three-peak average) is used to generate all the rest *Cp* min results employed in this comparison.

7.3 Results of wind loads above homogeneous terrain

Figures 7.3 – 7.5 present the most-critical *Cp* min and *Cp'* min results above OC, Suburban and Urban. As introduced in Chapter 3, the definition of *Cp* is different from that of *Cp'*. *Cp* uses the OC mid-roof height velocity-pressure as the reference pressure for the denominator, i.e.,

$$Cp = (p - p_o)/(0.5\rho U^2_{m-rf,OC}) \tag{7.1}$$

where p_o is the reference static pressure, ρ = air density, '*m-rf*,*OC*' = mid-roof height above OC terrain. The *Cp* definition has been employed in NBCC-1995, and can be used to directly compare the difference of the actual loads above different terrain configurations. *Cp'* uses the *local terrain* mid-roof height velocity-pressure as the reference pressure for the denominator, i.e.,

$$Cp' = (p - p_o)/(0.5\rho U^2_{m-rf,localTerrain}) \tag{7.2}$$

The *Cp'* definition has been held in ASCE 7-02. Conversion between *Cp* and *Cp'* for one actual pressure can be made by the following relationship,

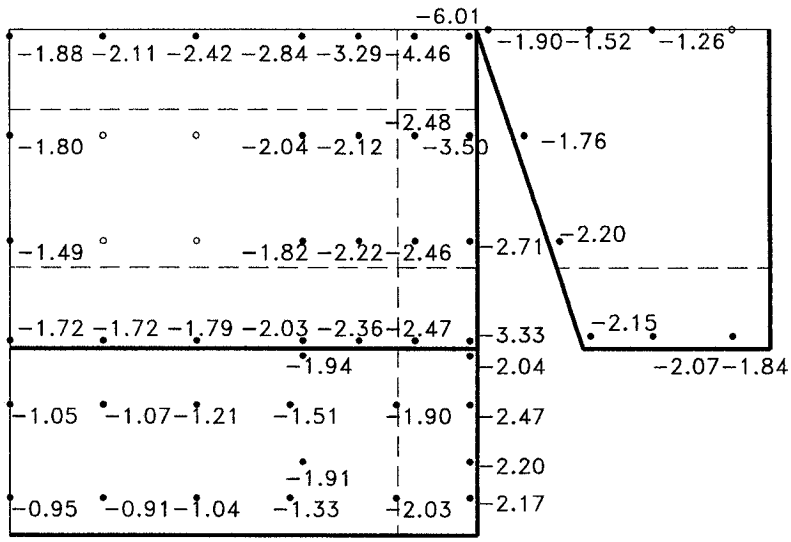

$$Cp = \frac{p - p_o}{0.5\rho U^2_{m-rf,OC}}$$

Fig. 7.3. Local (tap) most-critical *Cp* min measured above OC terrain.

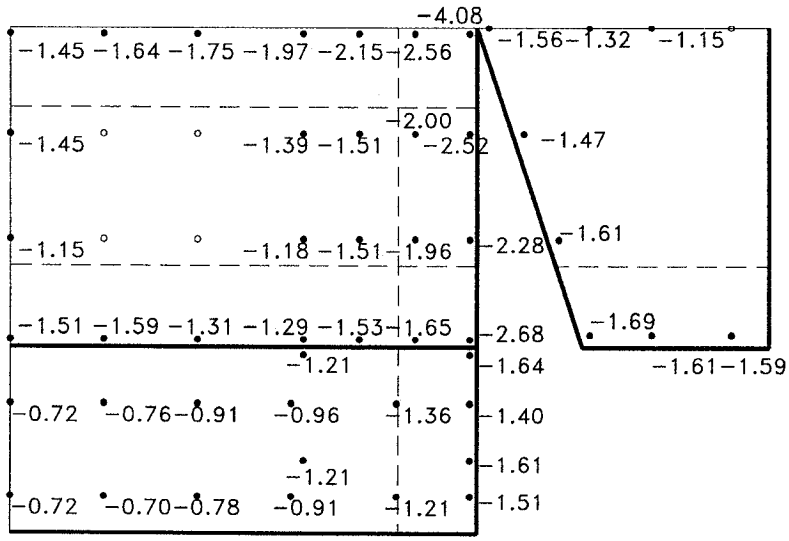

(a) $Cp = \dfrac{p - p_o}{0.5\rho U^2_{m-rf,OC}}$

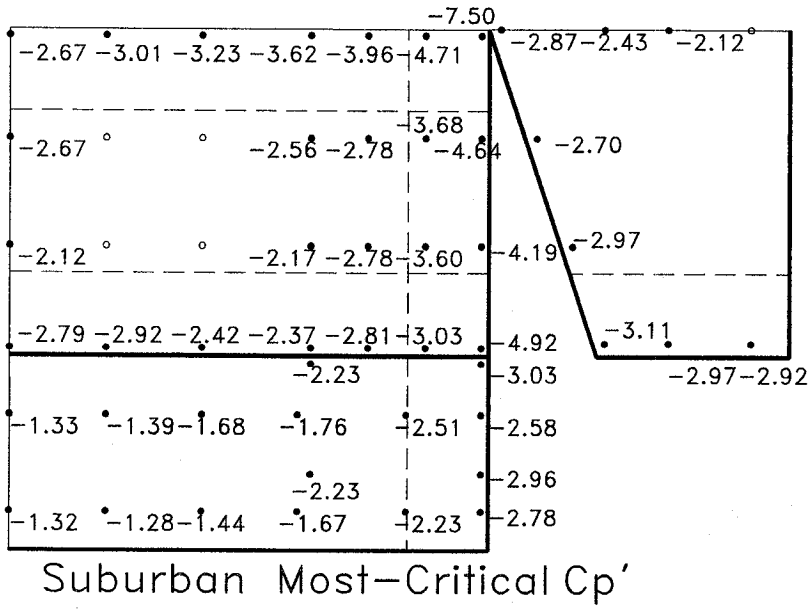

(b) $Cp' = \dfrac{p - p_o}{0.5\rho U^2_{m-rf,Suburban}}$

Fig. 7.4. Local (tap) most-critical *Cp* min and *Cp'* min measured above Suburban terrain.

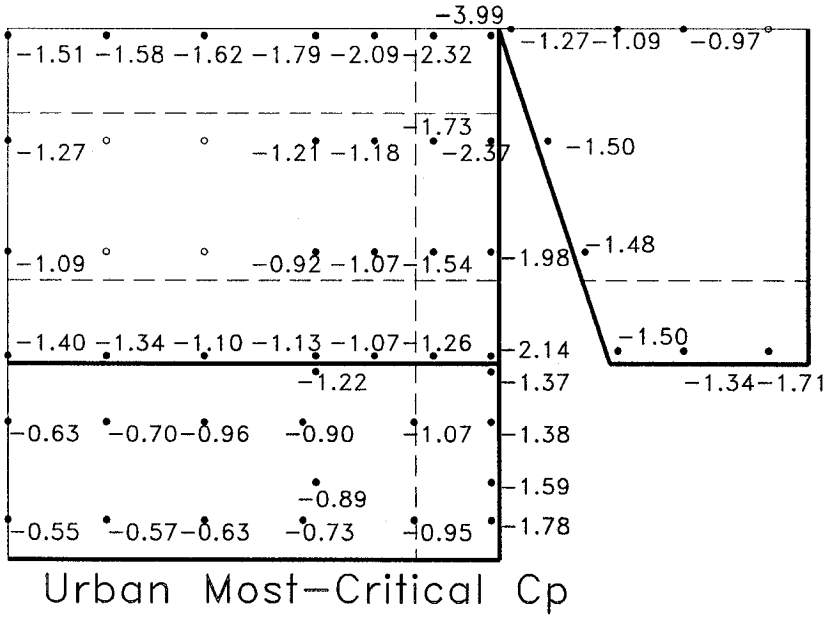

(a) $Cp = \dfrac{p - p_o}{0.5\rho U^2_{m-rf,OC}}$

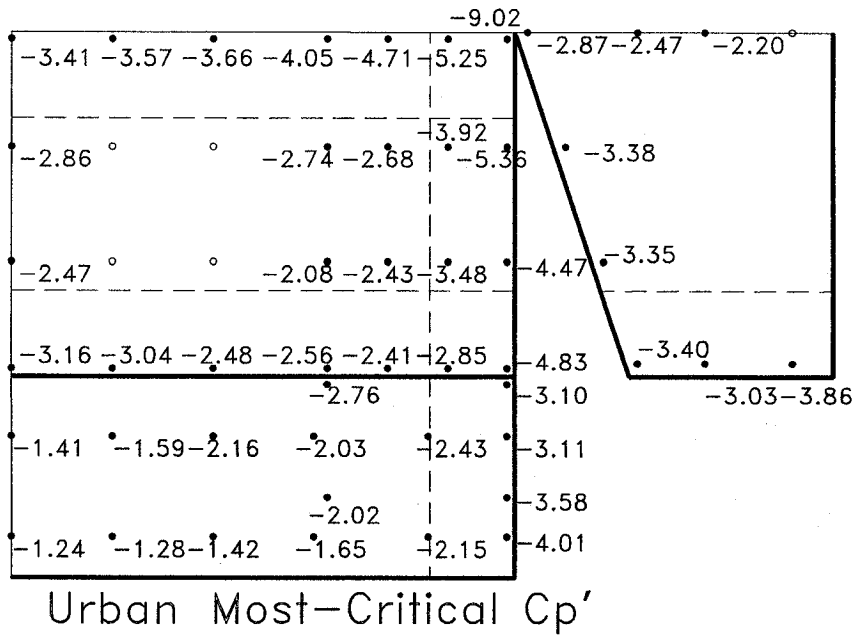

(b) $Cp' = \dfrac{p - p_o}{0.5\rho U^2_{m-rf,Urban}}$

Fig. 7.5. Local (tap) most-critical *Cp* min and *Cp'* min measured above Urban terrain.

$$P = 0.5Cp'\rho U^2_{m-rf,localTerrain} = 0.5Cp\rho U^2_{m-rf,OC} \quad (7.3)$$

Naturally, these definitions yield,

$$Cp'_{OC} \equiv Cp_{OC} \quad (7.4)$$

Figures 7.3 – 7.5 first show the good agreement of the present wind-tunnel results with ASCE 7-02 on the aerodynamic zoning definition as shown in Fig. 3.13. In fact, the ASCE 7-02 zoning definition is found effective for all fetch configurations in this study. The loads at gable end, ridge and corner areas (i.e. flow-separation-prone areas) are higher than those in the eave edge and interior areas. The roof corner, which is subject to the so-called "conical vortex", experiences the highest loads throughout all cases in this study.

Figures 7.3, 7.4a and 7.5a, which use the *Cp* definition, allow direct wind load comparison for these three terrains. Clearly, the peak negative loads above OC are higher than those above Suburban or Urban. On the other hand, the Suburban and Urban *Cp* min values do not fall far apart from each other.

Figures 7.3, 7.4b and 7.5b, which use the *Cp'* definition, cannot tell alone which terrain induces higher loads if the reference velocity pressures are not known. Magnitudes of Urban *Cp'* min are higher than those of Suburban, which in turn are much higher than those of OC. However, the behavior of mean pressure coefficients (*Cp* mean) may be different.

Comparing sets of data with a symmetric line (45°-line) as reference, Figs. 7.6 – 7.8 present *Cp* and/or *Cp'* results measured on the same set of pressure tappings but above two different homogeneous terrains. In this figure, the abscissa of a data point corresponds to the *Cp* (or *Cp'*) magnitude for a specific tapping above one terrain, while

the ordinate of the data point corresponds to the *Cp* (or *Cp'*) magnitude for the same tapping above another terrain; thus this form of comparison can easily show the degree of data similarity (or correlation), and which terrain gives higher loads.

Figure 7.6a presents the *Cp* mean results above OC and those above Suburban for 90°, 135°, and most-critical wind directions; the wind incidence angle (θ) definition and the building surface layout are shown in this figure, while the detailed tapping layout has been given in Fig. 3.11. Figure 7.6a shows that the magnitudes of OC *Cp* mean results are higher than those of the Suburban ones. Figure 7.6a also shows that both roof and wall loads collapse well onto a same straight line (with little scatter), implying that the OC loads have high similarity (i.e. correlation) with their Suburban counterparts. Therefore, one can use the OC *Cp* mean with a proper scaling factor (e.g. slope of a fit line) to estimate the Suburban *Cp* mean; this is true for both roof and wall loads.

The same data presented as *Cp* mean in Fig. 7.6a are also presented as *Cp'* mean in Fig. 7.6b in order to investigate the relationship of OC and Suburban *Cp'* values. It is found that OC local-tapping *Cp'* mean values are approximately equal to the corresponding Suburban values.

Similar to Figs. 7.6a and 7.6b, Figs. 7.6c and 7.6d present respectively the OC and Suburban local *Cp* and *Cp'* min values. Figure 7.6c shows that the magnitudes of the OC *Cp* min results are also slightly higher than those of Suburban. Therefore, *Cp* min results are less sensitive to terrain change than *Cp* mean data. This finding was also reported by Surry and Djakovich (1995) in their tall building cladding load study. On the other hand,

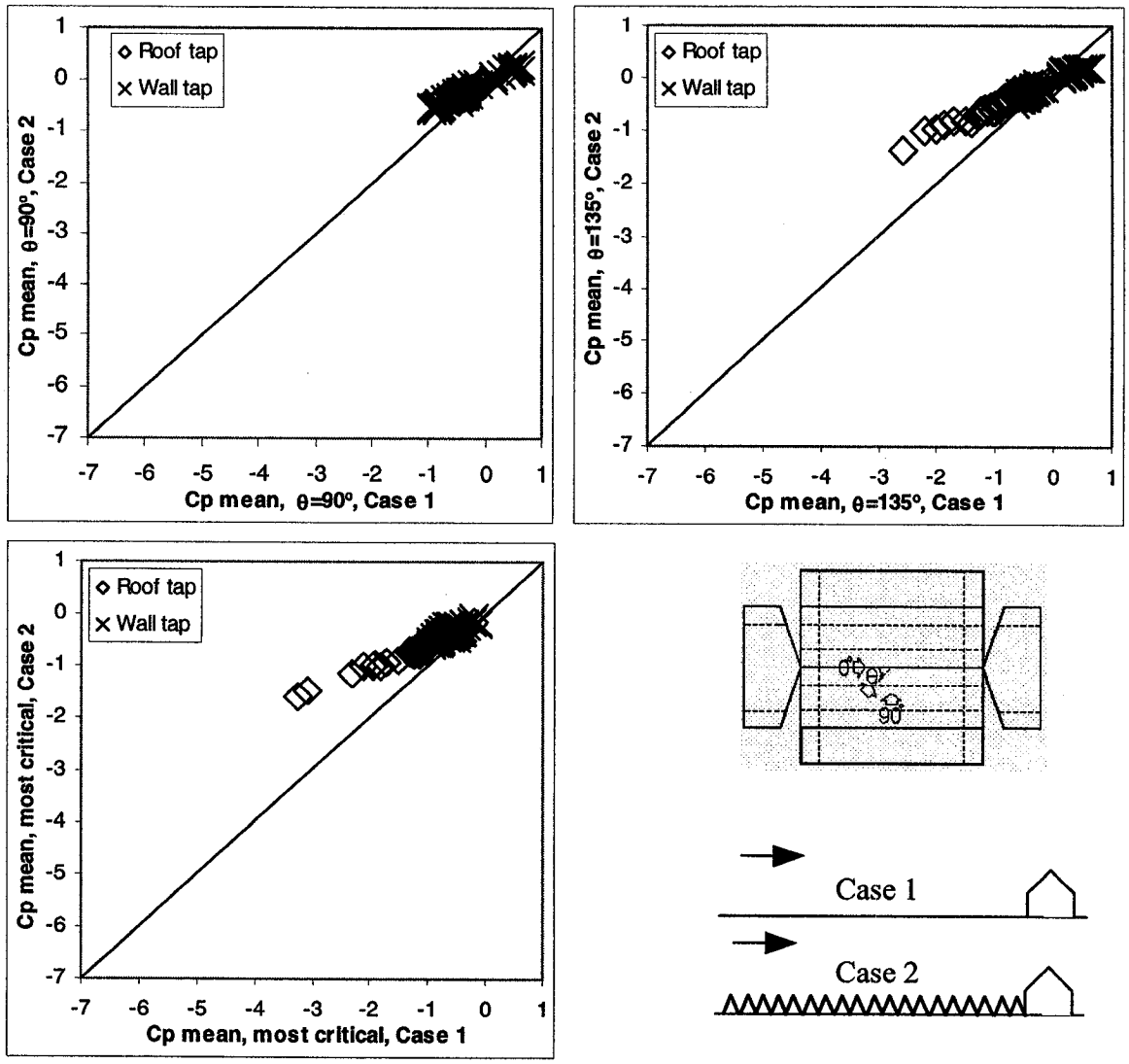

Fig. 7.6a. Local *Cp* mean results above Case (1) OC and Case (2) Suburban.

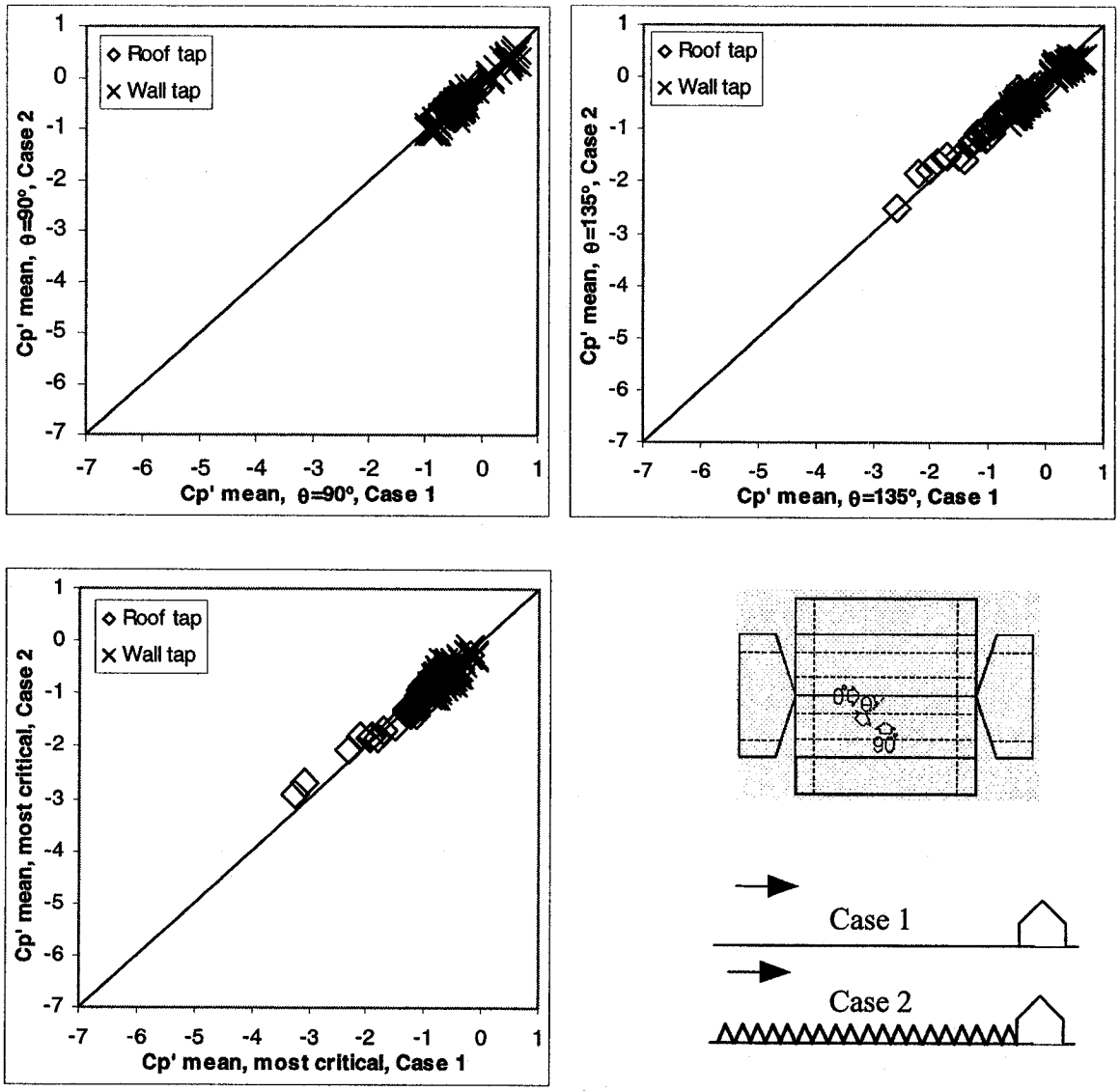

Fig. 7.6b. Local *Cp´* mean results above Case (1) OC and Case (2) Suburban.

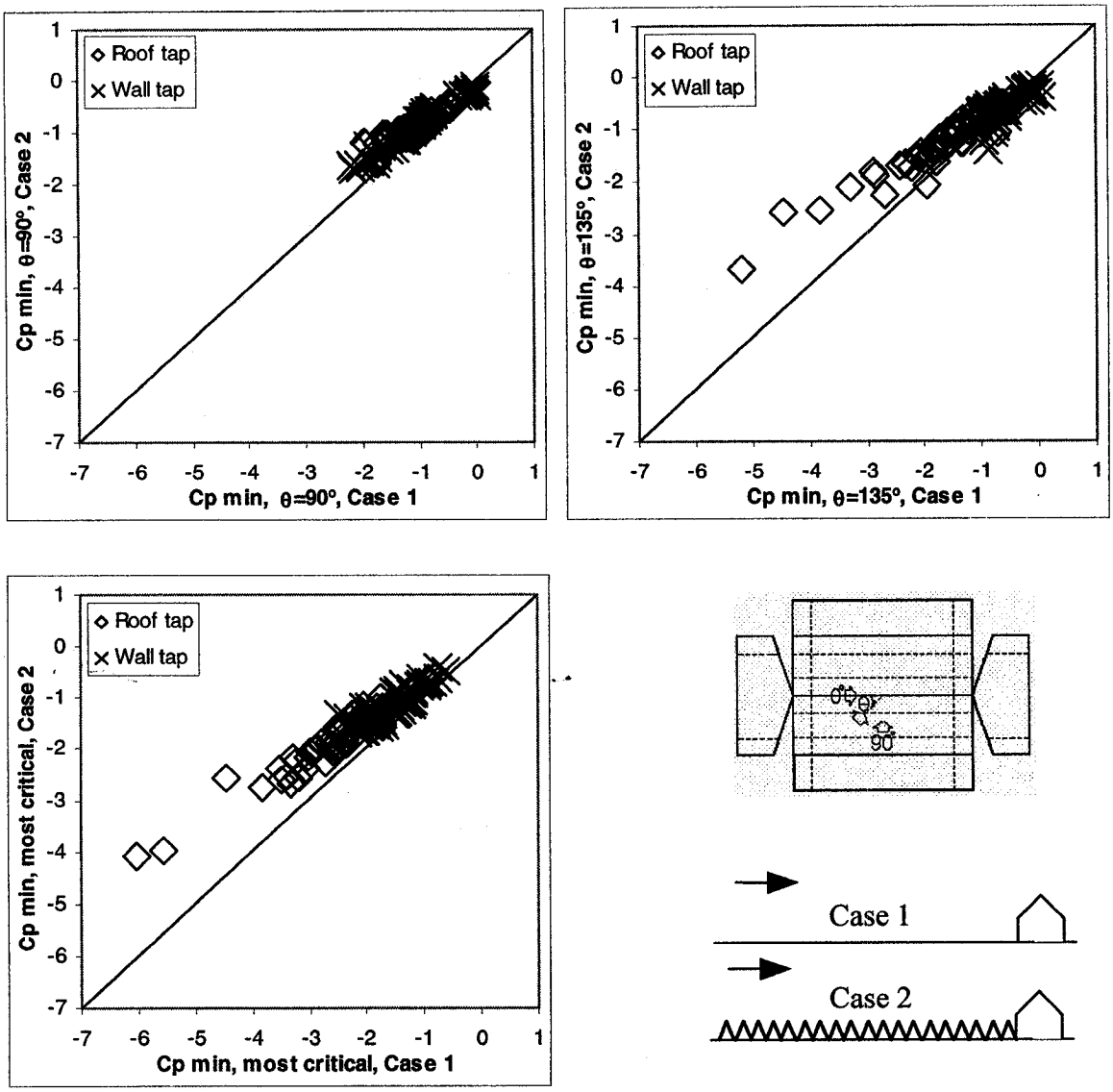

Fig. 7.6c. Local *Cp* min results above Case (1) OC and Case (2) Suburban.

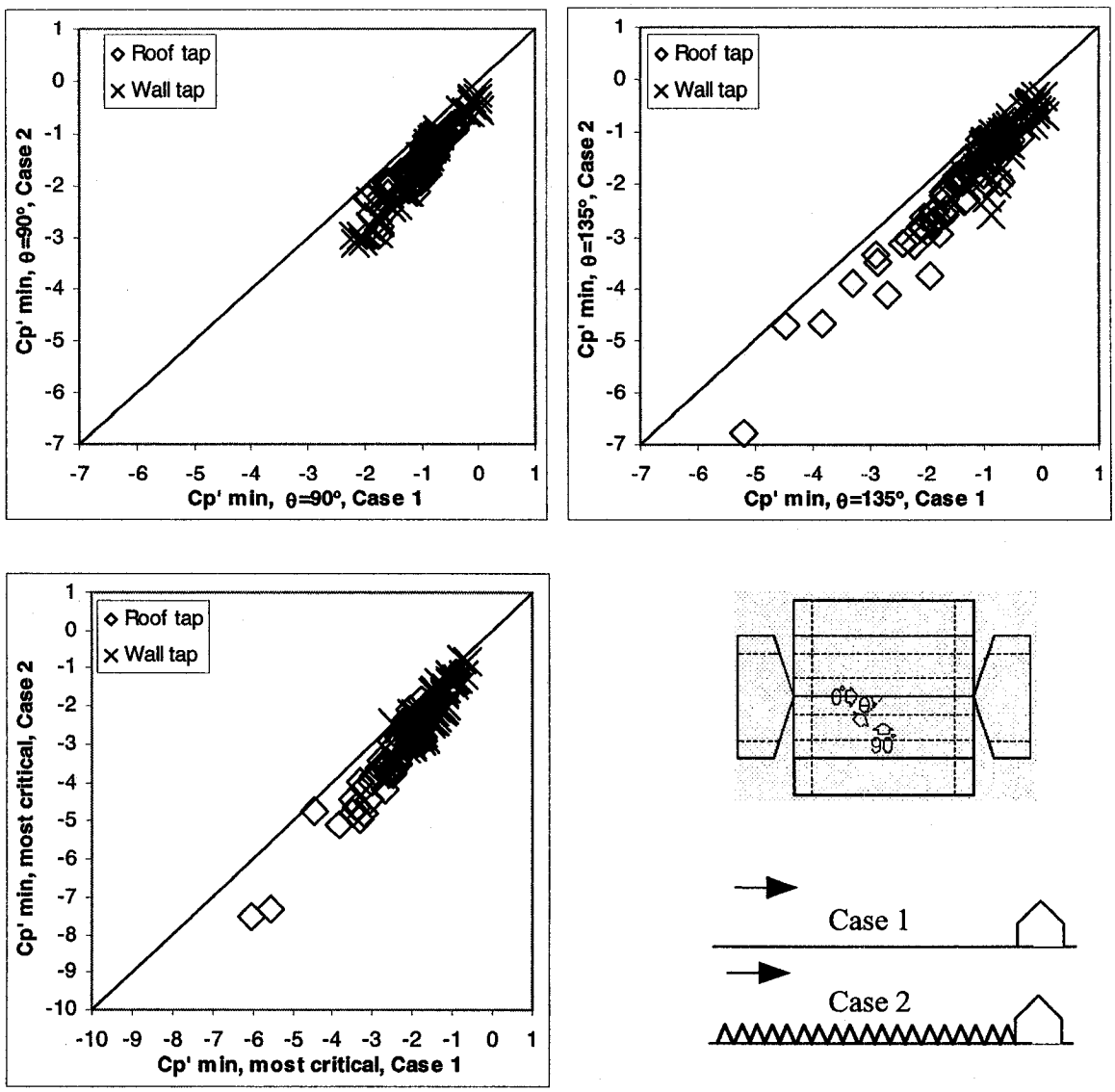

Fig. 7.6d. Local *Cp'*min results above Case (1) OC and Case (2) Suburban.

Fig. 7.6d shows that the Cp'min data above Suburban are much higher than those above OC. Hence the good match between the OC Cp'mean data and those of Suburban (see Fig. 7.6b) does not recur for the OC and Suburban Cp'min data

Figure 7.7 compares OC Cp and Cp'values (both mean and min) with the Urban counterparts in the same format with that shown in Fig. 7.6. Fig. 7.7 shows very similar data trends as Fig. 7.6 does; in fact the data in Fig. 7.7 very clearly show a high degree of correlation.

It is of interest to make a direct comparison of Cp min values of Suburban with those of Urban, in order to see the load differences. Figure 7.8 shows that the magnitudes of Suburban and Urban Cp min results are similar to each other, although Suburban suction values are somewhat higher.

Generally speaking, Figs. 7.6 – 7.8 show that roof pressure coefficients are influenced by terrain roughness in a way similar to those measured on the walls. Thus if one can estimate roof pressure coefficients properly, then one should be able to estimate wall Cp values. Therefore, the following discussion will focus on the behavior of roof loads. In addition, it is found that the present findings do not strongly support using $Cp'$to describe terrain effects; since Cp'values just show certain (statistical) similarity among mean values, which are not of direct interest to structural design however.

7.4 Results of wind loads above fetch with a single roughness change

It is probably the first time that a systematic study was made on the low-rise building wind load variation above fetch with a single roughness change.

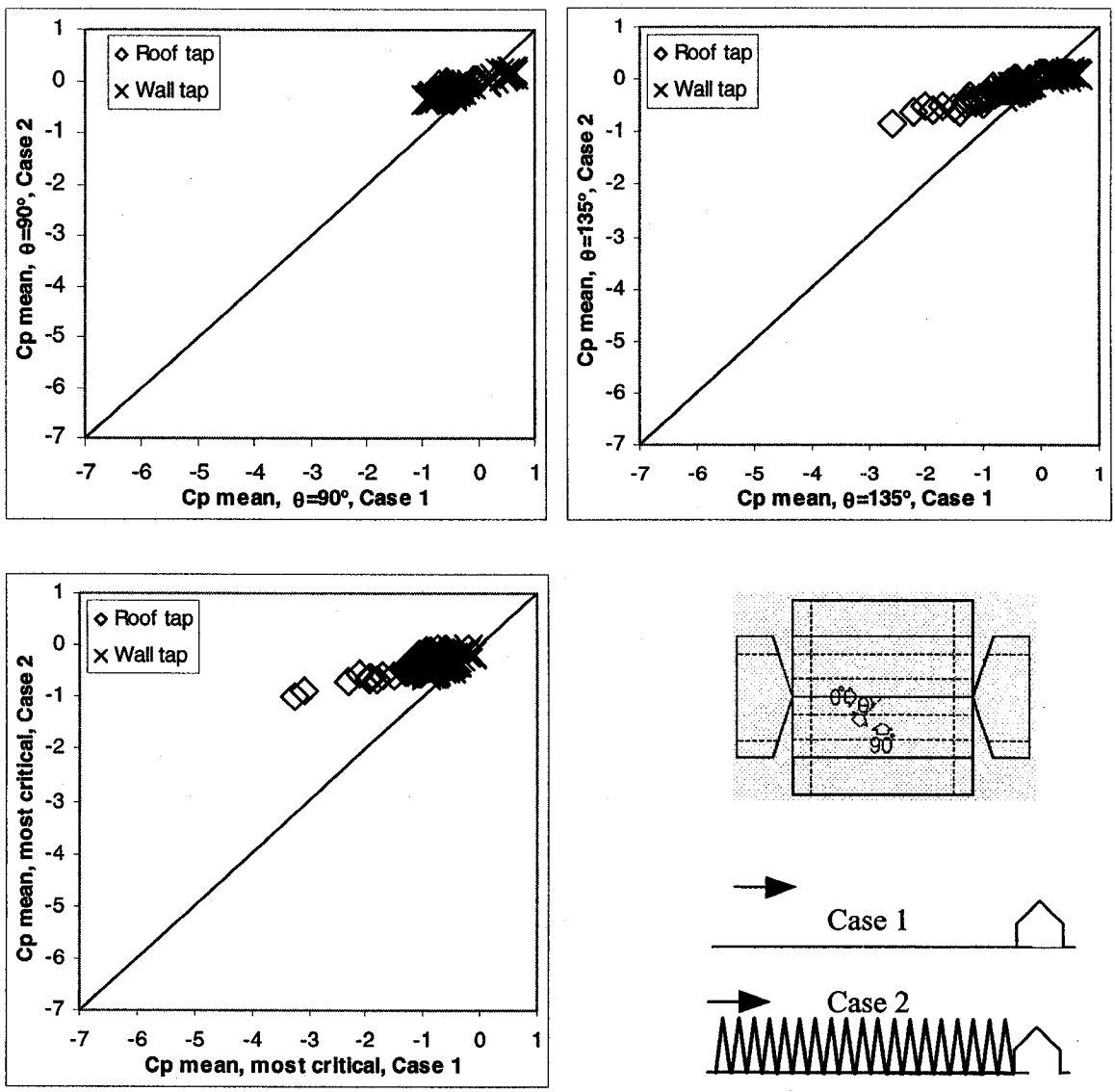

Fig. 7.7a. Local *Cp* mean results above Case (1) OC and above Case (2) Urban.

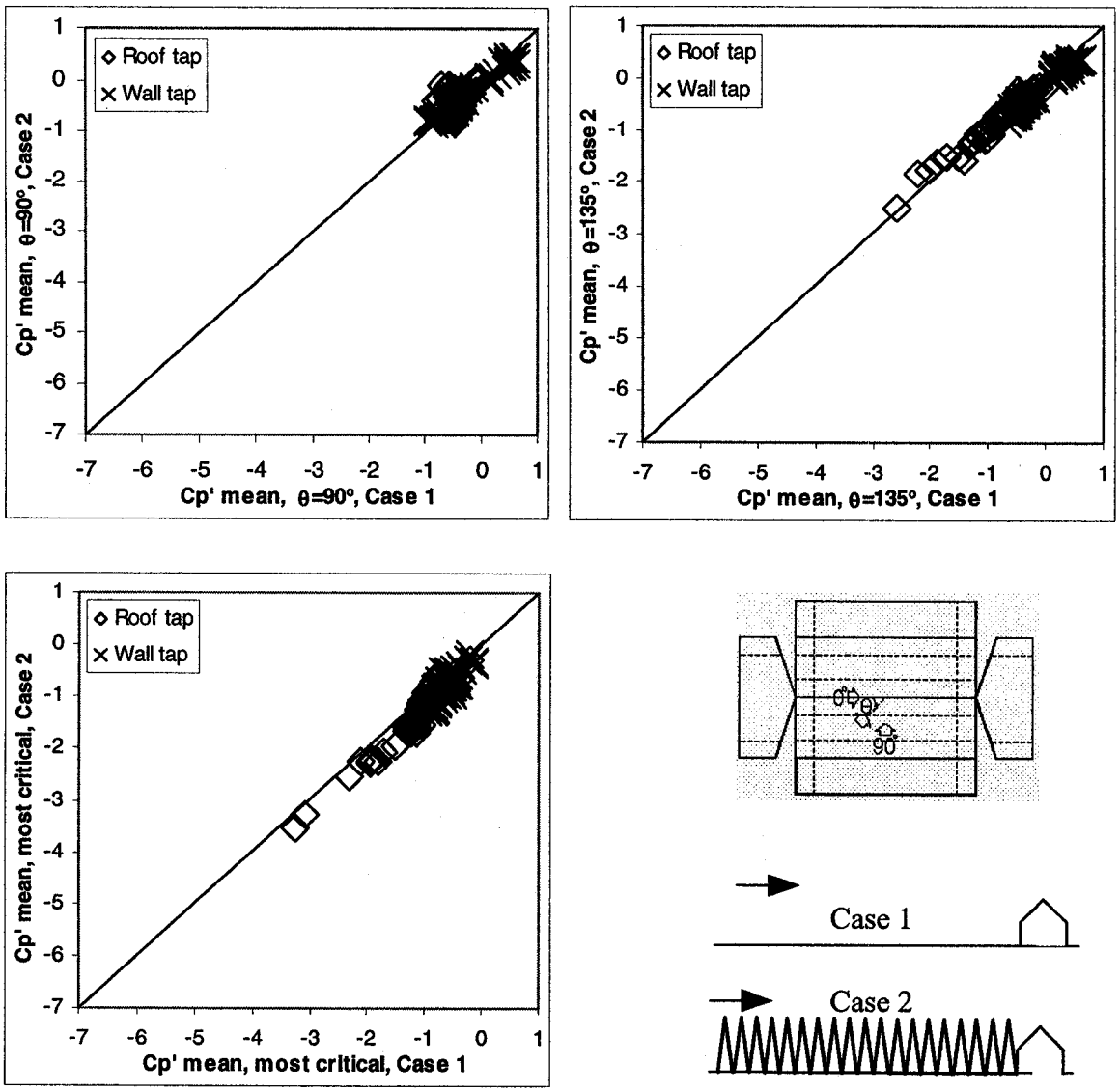

Fig. 7.7b. Local *Cp'* mean results above Case (1) OC and Case (2) Urban.

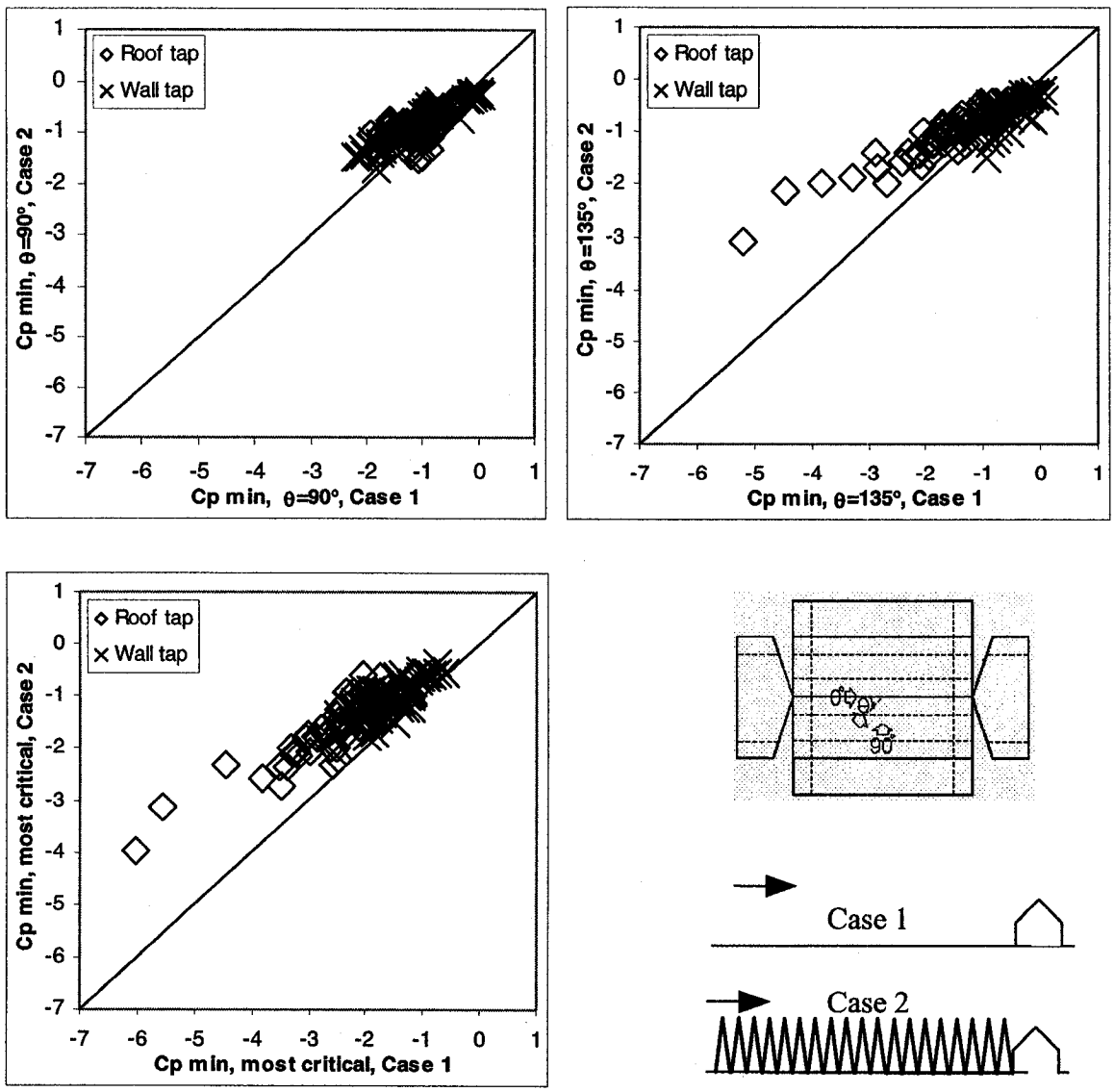

Fig. 7.7c. Local *Cp* min results above Case (1) OC and Case (2) Urban.

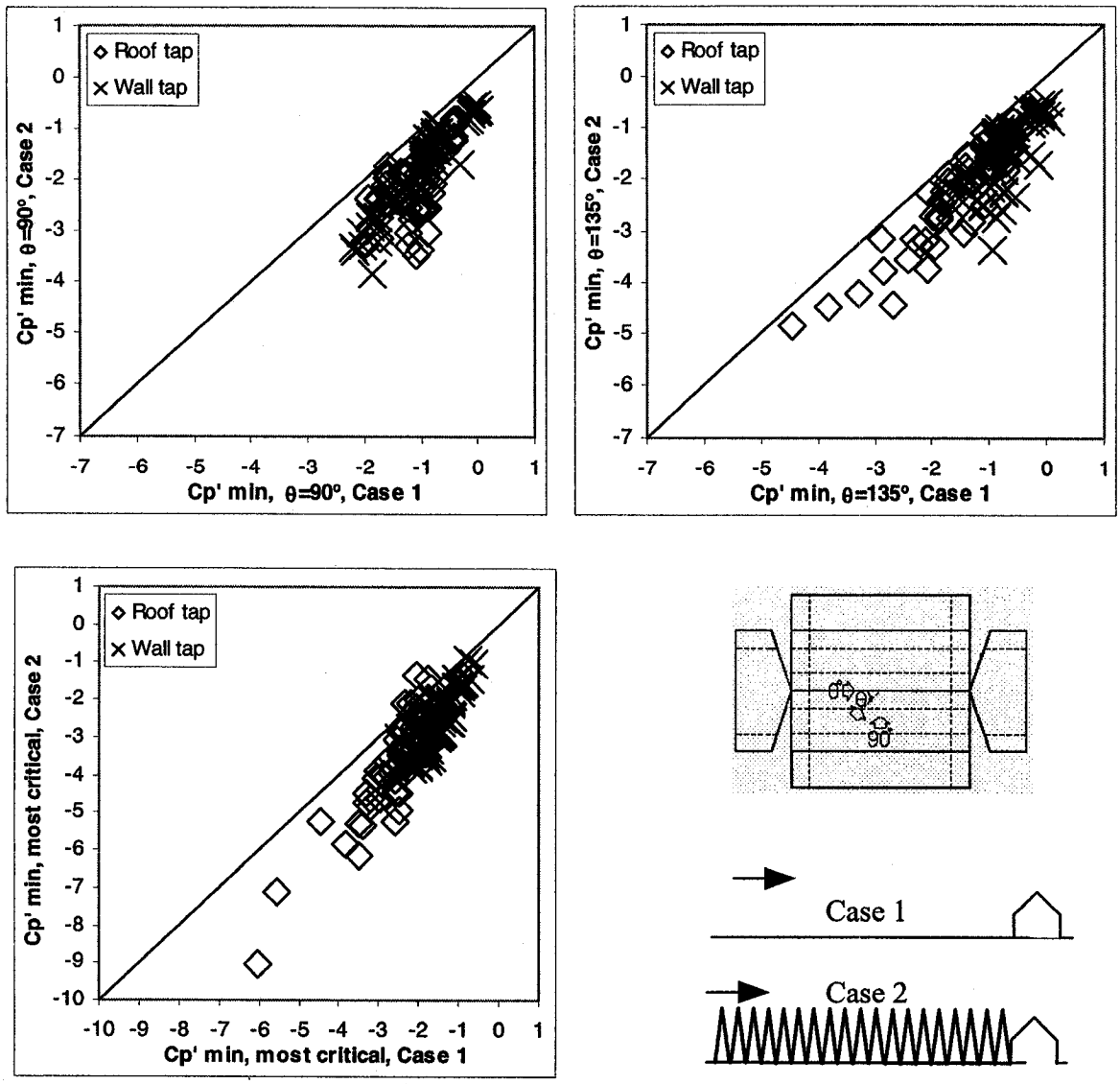

Fig. 7.7d. Local *Cp'*min results above Case (1) OC and Case (2) Urban.

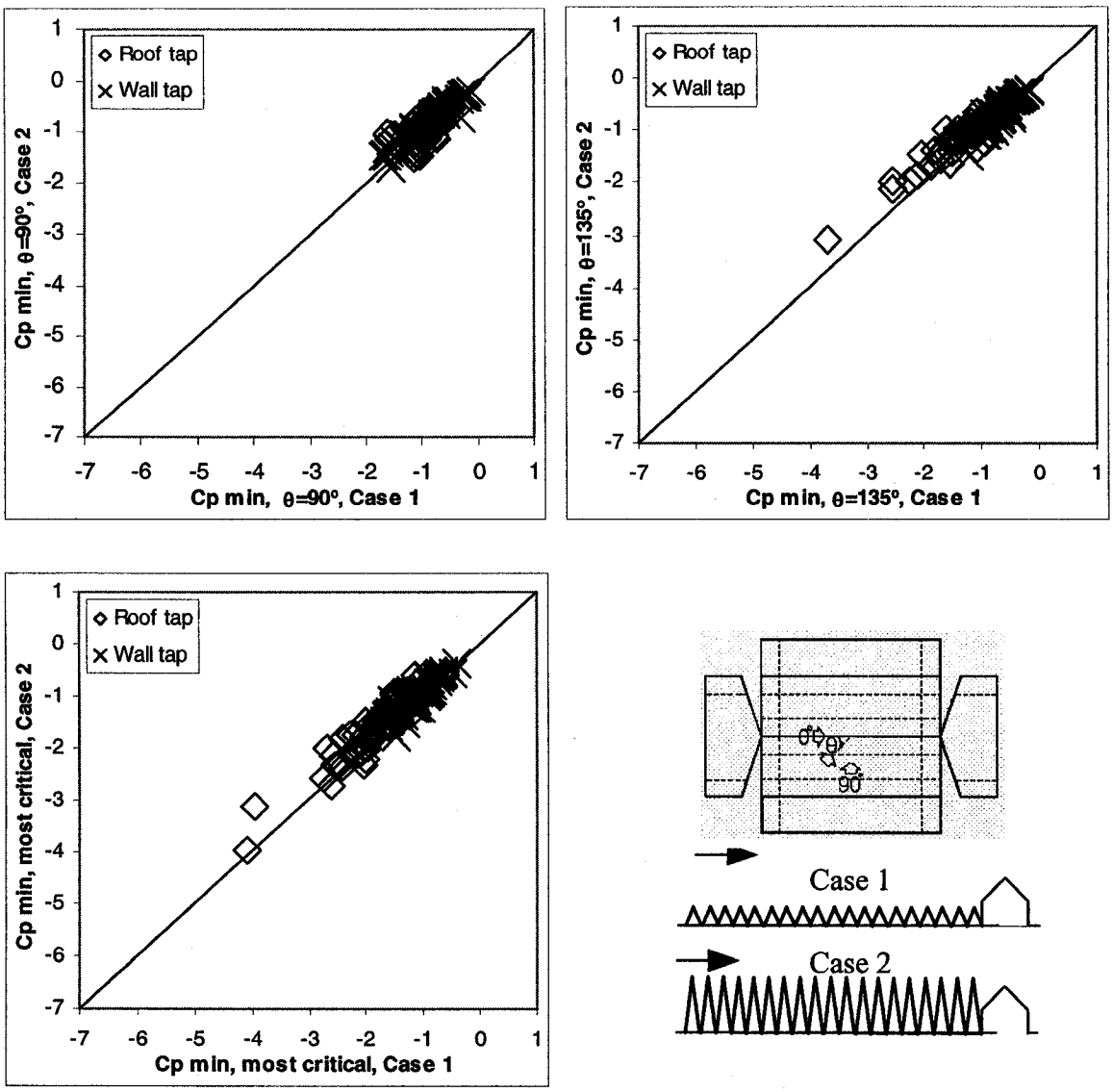

Fig. 7.8. Local *Cp* min results above Case (1) Suburban and Case (2) Urban.

A single roughness change from rough to smooth

As shown in Table 2.4, some wind standards and codes of practice provide specifications of discrepancies on the minimum fetch length to qualify as homogeneous terrain. Presently, Figs. 7.9 – 7.18 provide an opportunity to look into this issue.

Figures 7.9 compares the *Cp* results above OC with those above the fetch case '*Open patch of 125 m long directly upstream to the building with Urban as remainder*', and and 7.10 compares the *Cp* results above OC with those above the fetch case '*Open patch of 500 m long directly upstream to the building with Urban as remainder*'. The only variable of interest herein is the length of the OC patch. In comparison to Figure 7.9, Fig. 7.10 shows that the OC patch about very hundred meters long can raise the wind loads close to the OC load level. As a matter of fact, it is not inconsistent with the findings of Young and Vickery (1998).

Figure 7.11 shows that the presence of the OC patch in the order of 100 m long directly upstream to the building on otherwise Urban terrain can significantly increase all of the important load quantities (local and zonal-area, most-critical *Cp*, mean and min). The definition of aerodynamic zone is shown in Fig. 3.13 after the ASCE 7-02 definition (cf. Stathopoulos et al. 1999, 2001), which is slightly different from specification in another work (e.g. NBCC-1995; Stathopoulos et al. 2000). The term 'zonal' implies the most-critical local *Cp* measured within this particular zone, irrespective of the wind attack angle. Furthermore, the term 'zonal-area' stands for the area-average *Cp* of an entire zone. In this figure, the wind load is presented as a function of the OC patch length

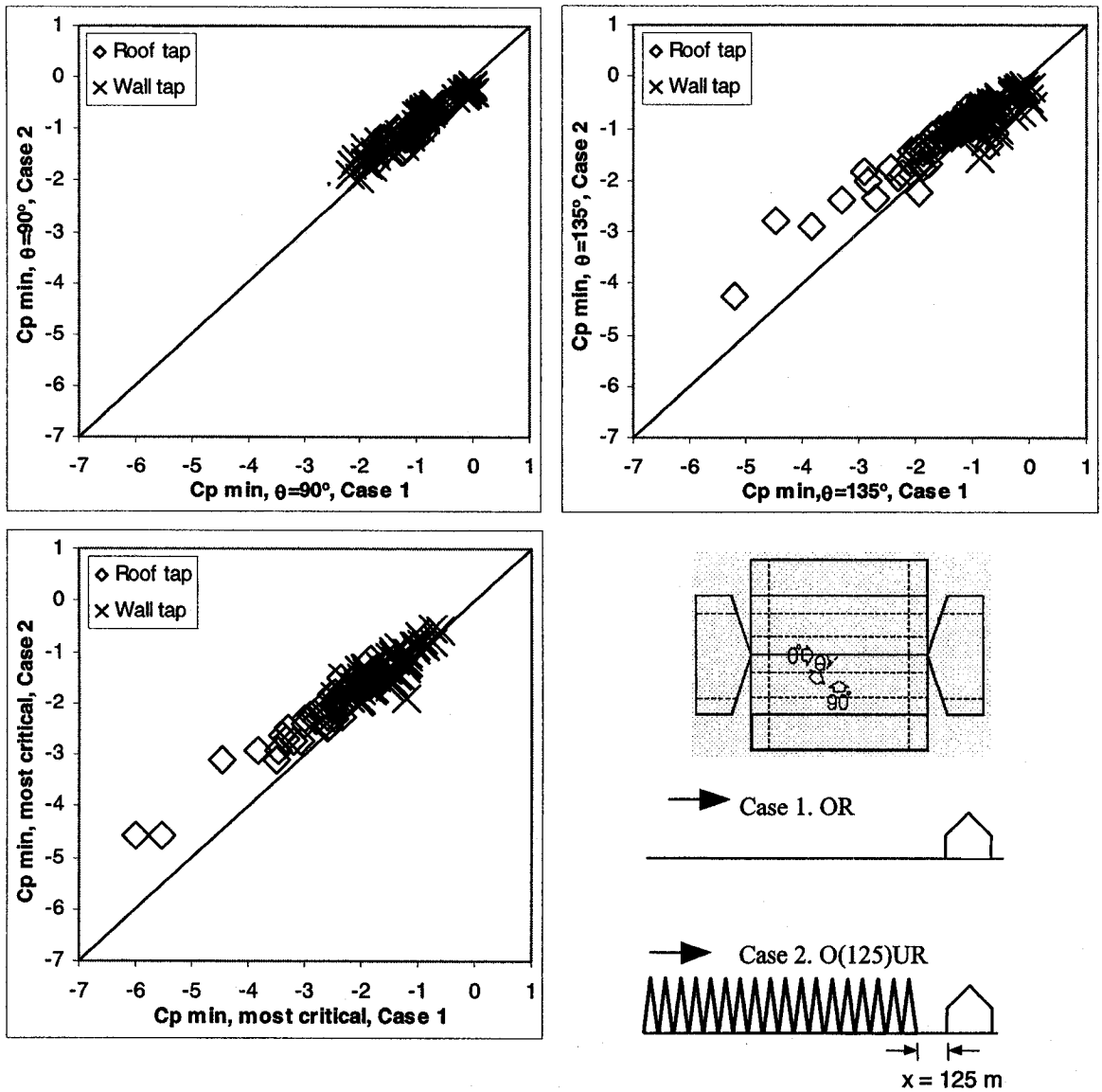

Fig. 7.9. Local *Cp* min results above Case (1) OC terrain and Case (2) 'OC patch of 125 m long directly upstream to the building with Urban as remainder'.

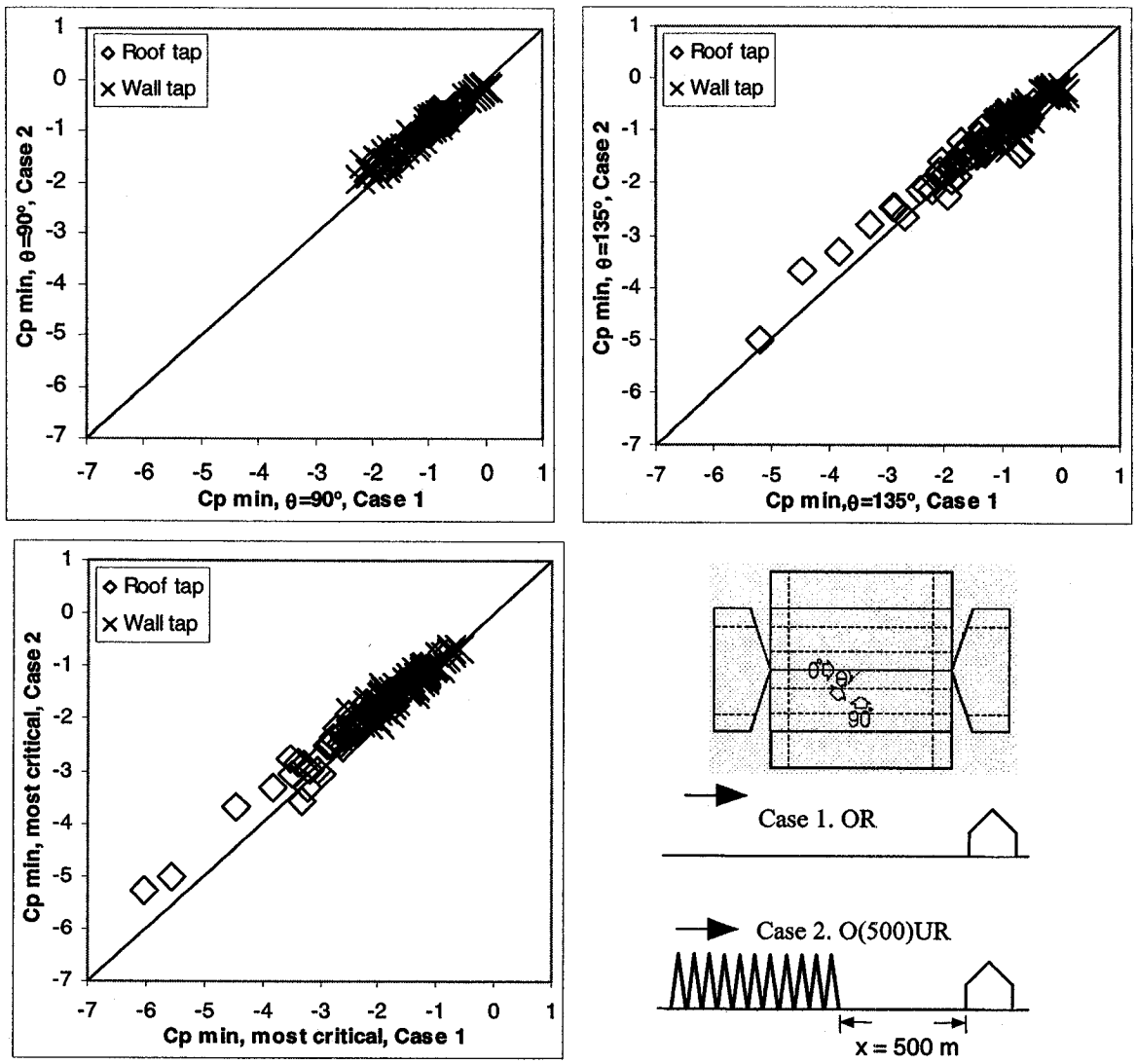

Fig. 7.10. Local *Cp* min results above Case (1) OC and Case (2) 'OC patch of 500 m long directly upstream to the building with Urban as remainder'.

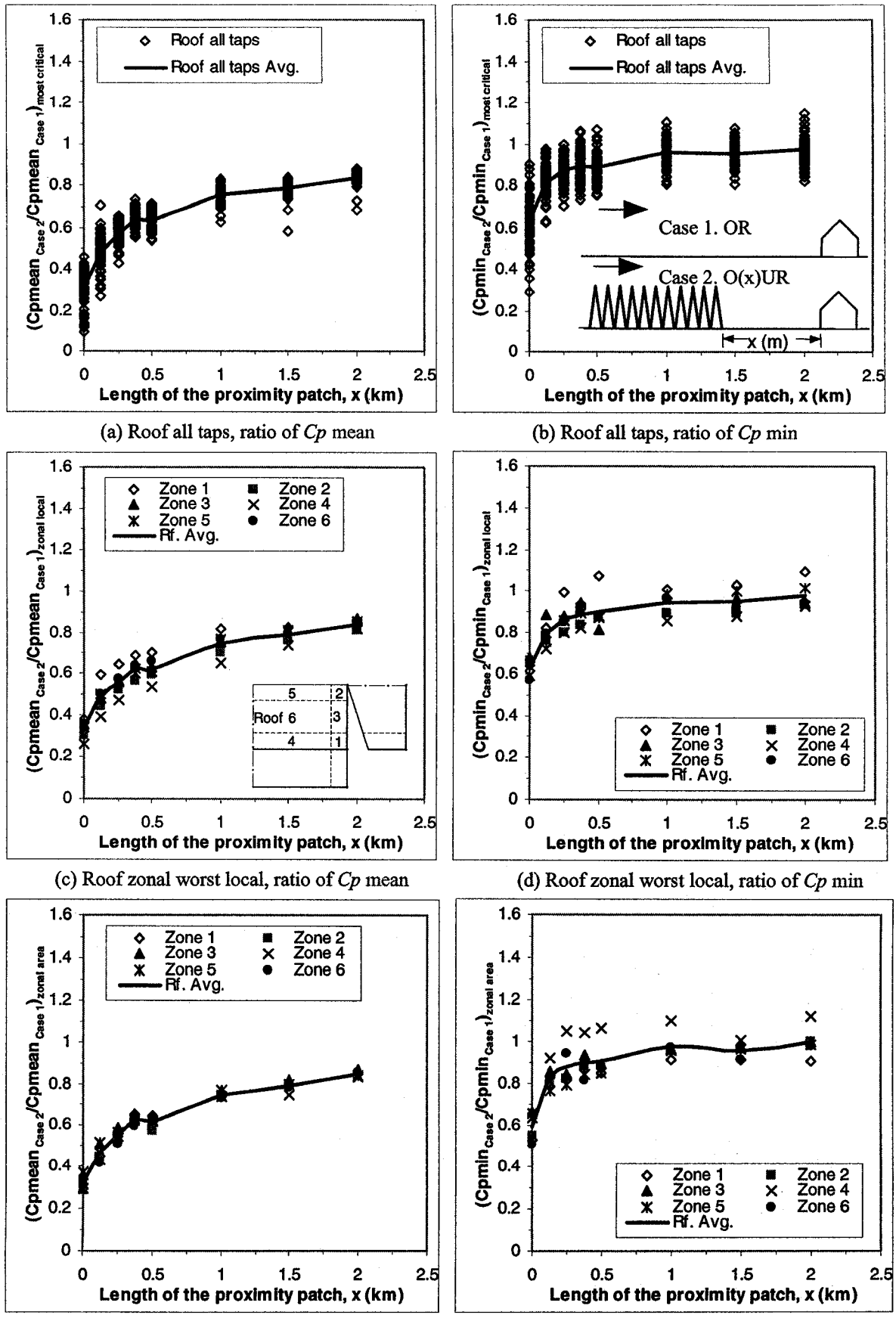

Fig. 7.11. Most-critical *Cp* ratios for the cases in the test Group 'OC patch of variable length directly upstream to the building with Urban as remainder (i.e. O(*x*)UR)'.

and in terms of *Cp* ratio, the numerator of which is *Cp* of Case 2 (*local terrain*) and the denominator is *Cp* of Case 1 OC; in a greater detail, the diagrams (a) - (f) present local mean, local min, zonal-local mean, zonal-local min, zonal-area mean, and zonal-area min load, respectively.

Diagrams (a) and (b) of Fig. 7.11 show that the loads increase rapidly with the OC patch length increment, and then gradually stabilize, and a 125 m OC patch directly upstream to the building can increase the loads significantly. It takes about 250 – 500 m for the peak loads to stabilize, while the mean loads take a longer distance to stabilize. In addition, these two diagrams show that the Urban mean- and min-load averages are about 30% and 60% of their OC counterparts respectively, although their variability is high. Furthermore, it is found that the most critical local values in each zone and the area-averaged *Cp*'s in the diagrams (c) – (f) of Fig. 7.11 show similar trends and magnitudes as do the diagrams (a) and (b).

Figure 7.12 shows similar findings with those of Fig. 7.11, except that the Suburban mean and peak load averages are about 55% and 75% of their OC counterparts respectively. A detailed comparison of the data presented in Figs. 7.11 and 7.12 reveals that the wind loads are, on average, similar in the presence of an open patch of the order of 100 m, no matter what the further upstream roughness type is, Suburban or Urban; that is to say, the wind loads are dominated mainly by the small-scale (of the order of 100 m) terrain roughness directly upstream to the building, but not strongly affected by further upstream terrain configurations. It should be noted that in the present experiments, there were variations of the static pressure from case to case, corresponding to different

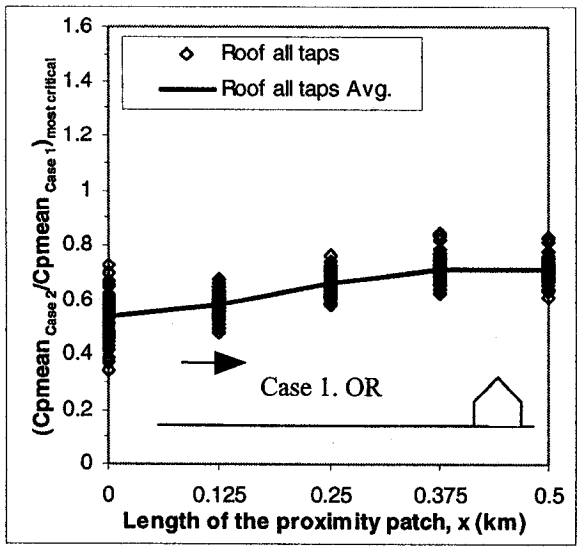

(a) Roof all taps, ratio of *Cp* mean

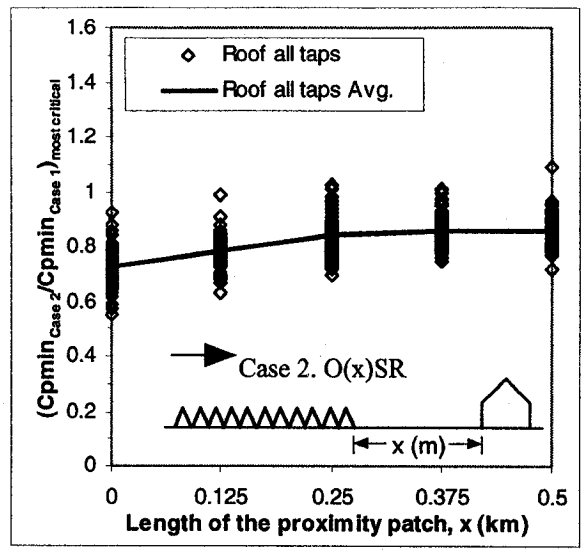

(b) Roof all taps, ratio of *Cp* min

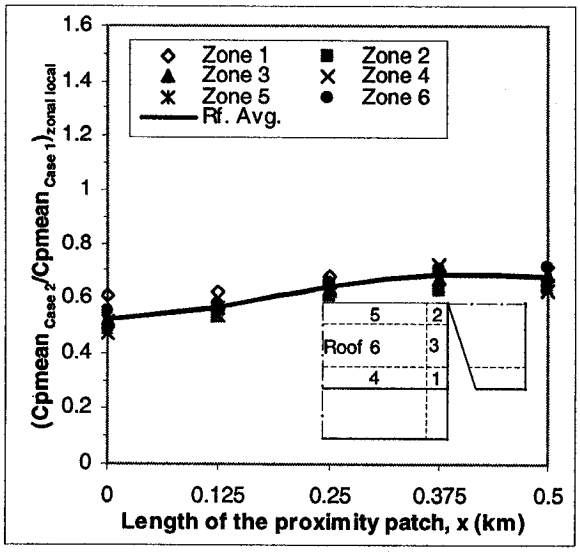

(c) Roof zonal worst local, ratio of *Cp* mean

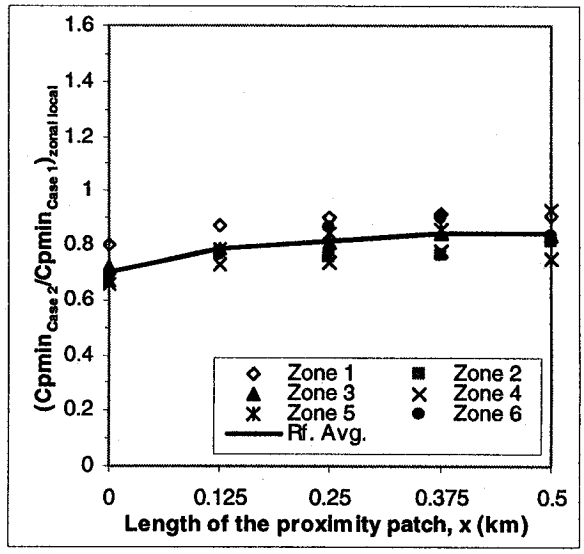

(d) Roof zonal worst local, ratio of *Cp* min

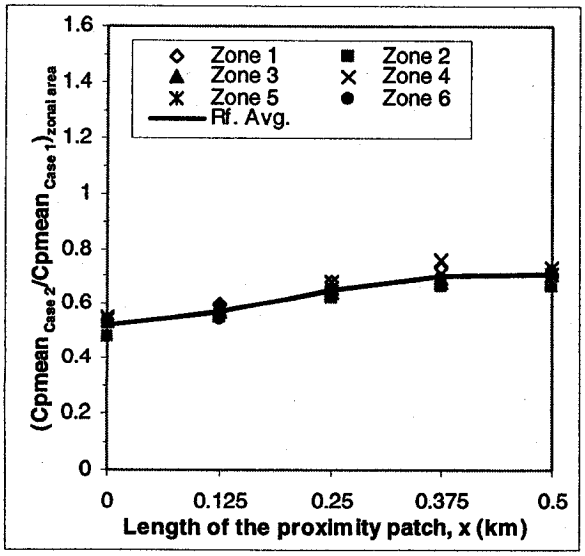

(e) Roof zonal area, ratio of *Cp* mean

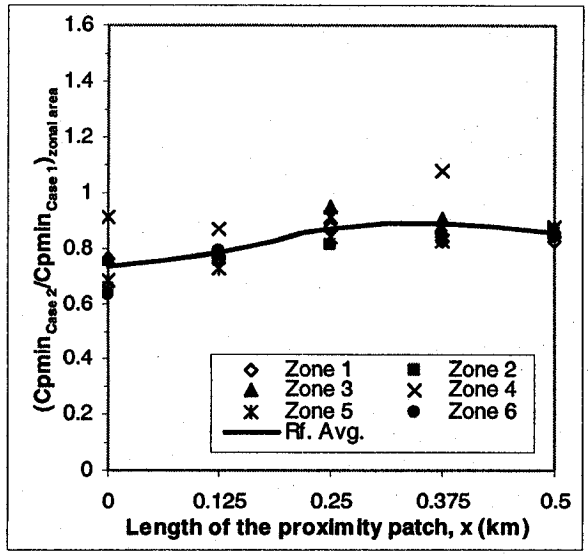

(f) Roof zonal area, ratio of *Cp* min

Fig. 7.12. Most-critical *Cp* ratios for the cases in the test Group 'OC patch of variable length directly upstream to the building with Suburban as remainder (i.e. O(*x*)SR)'.

roughness configurations (see Fig. 3.14); as a result, every 'Case 2' configuration may not reflect the same speed and turbulence profile and this may explain the variation of data in Figs. 7.11 and 7.12.

A single roughness change from smooth to rough

Figure 7.13 compares with a symmetric line (45°-line) as reference of *Cp* above the fetch Case 1 Suburban with those above Case 2 '*Suburban patch 125 m long directly upstream to the building with OC as remainder*'. Figure 7.13 shows that a short Suburban patch is sufficient to decrease the loads to the level of Suburban.

Figure 7.14 shows that the presence of the Suburban patch of length in the order of 100 m directly upstream to the building on otherwise OC terrain can significantly decrease all of the important load quantities. The loads decrease rapidly with the Suburban patch length increment till about 250 - 500 m, and then gradually stabilize. Hussain and Lee (1980), Holmes (1994), and Young and Vickery (1998) have also reported that a very short rough patch can fully reduce the wind loads as a rough terrain does. Similar to Fig. 7.11, Fig. 7.14 also shows that the mean loads take longer distance to stabilize than do the peak loads.

Results of Fig. 7.15 are similar to those of Fig. 7.14. Now it is clearer to see that the 250 - 500 m long Urban patch directly upstream to the building is sufficient to level off both peak or mean loads.

Generally speaking, Figs. 7.14 and 7.15 reveal that the wind loads are very sensitive

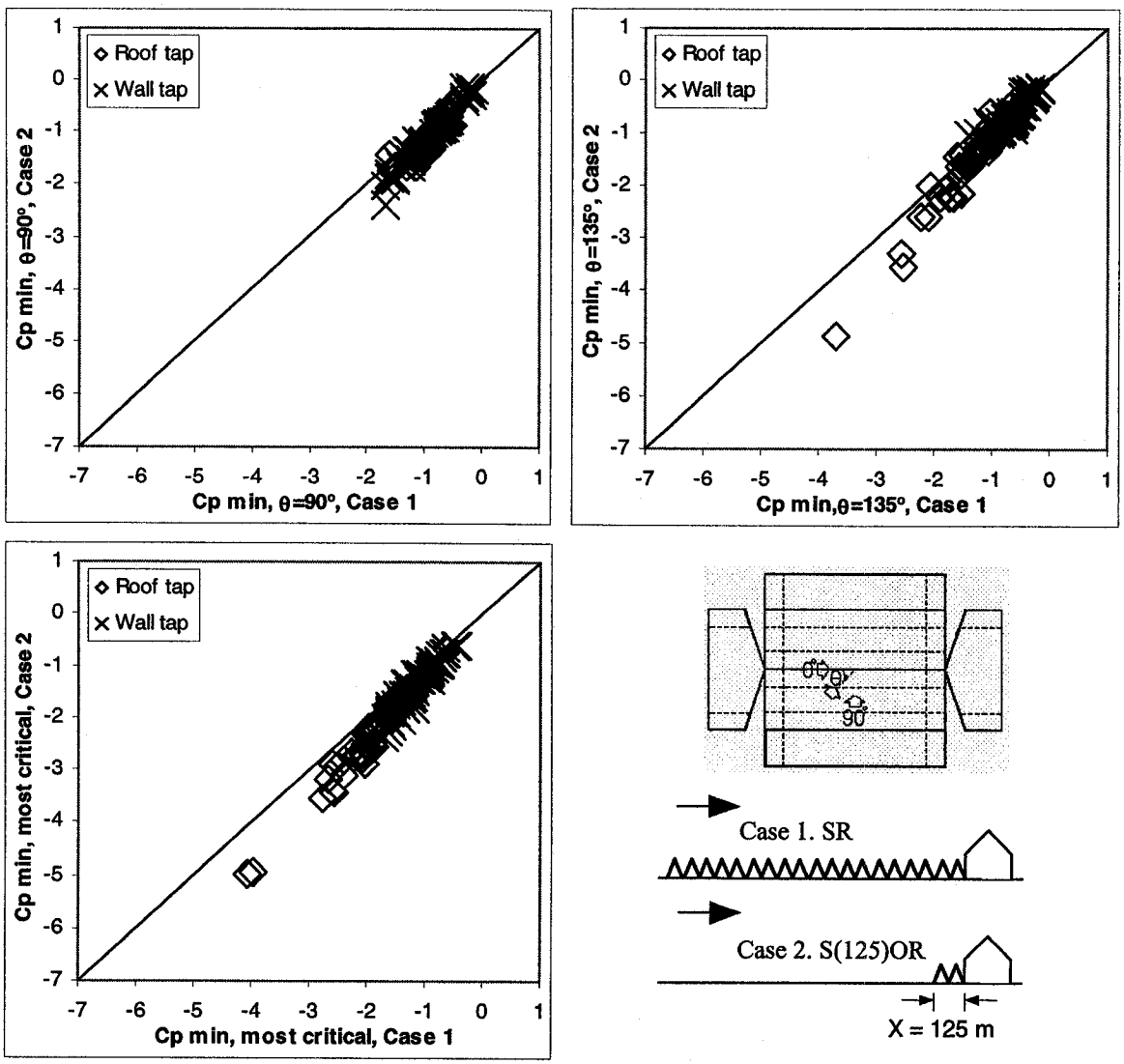

Fig. 7.13. Local *Cp* min results above Case (1) OC terrain and Case (2) 'Suburban patch of 125 m long directly upstream to the building with OC as remainder'.

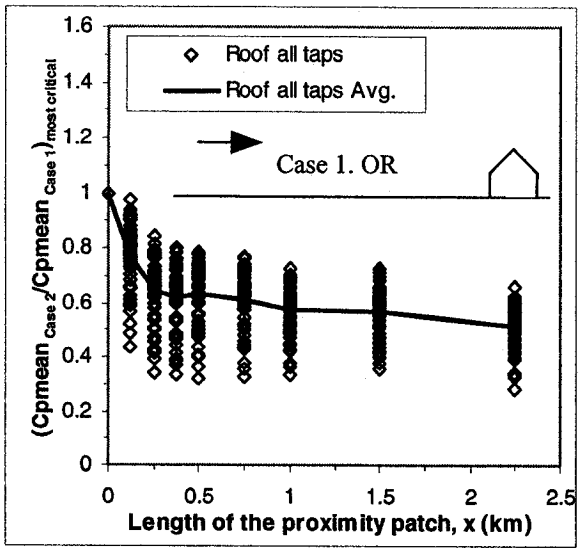

(a) Roof all taps, ratio of *Cp* mean

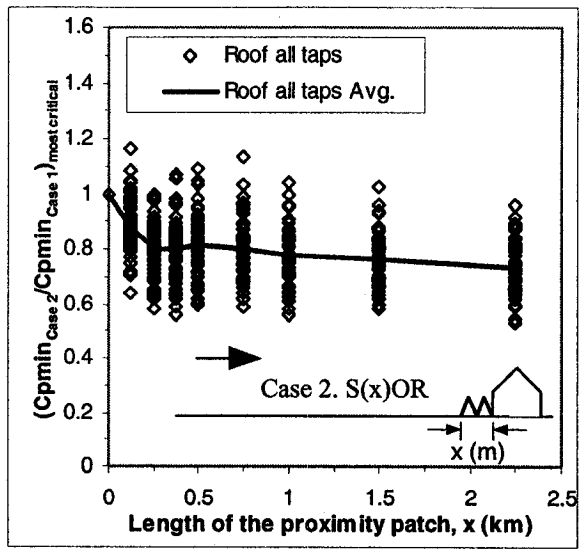

(b) Roof all taps, ratio of *Cp* min

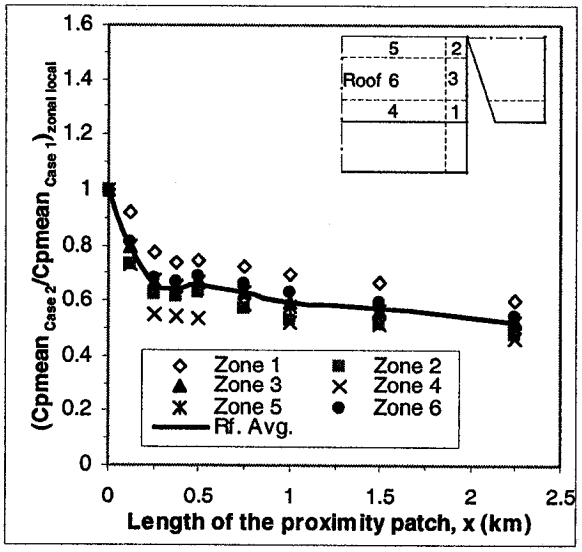

(c) Roof zonal worst local, ratio of *Cp* mean

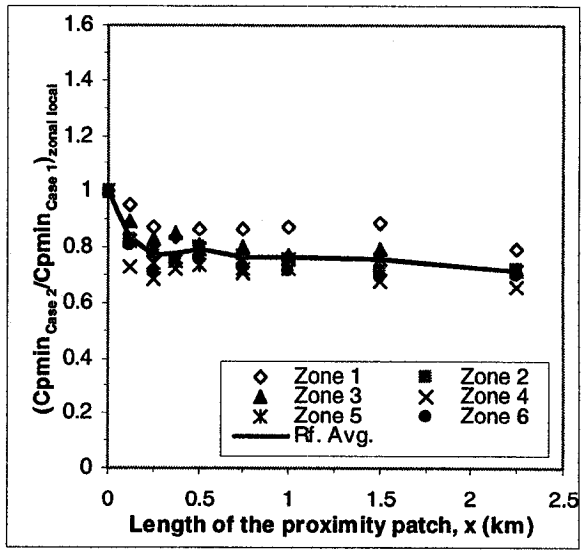

(d) Roof zonal worst local, ratio of *Cp* min

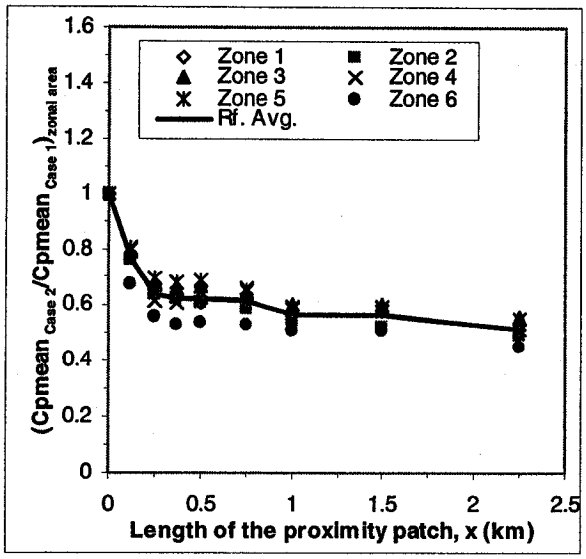

(e) Roof zonal area, ratio of *Cp* mean

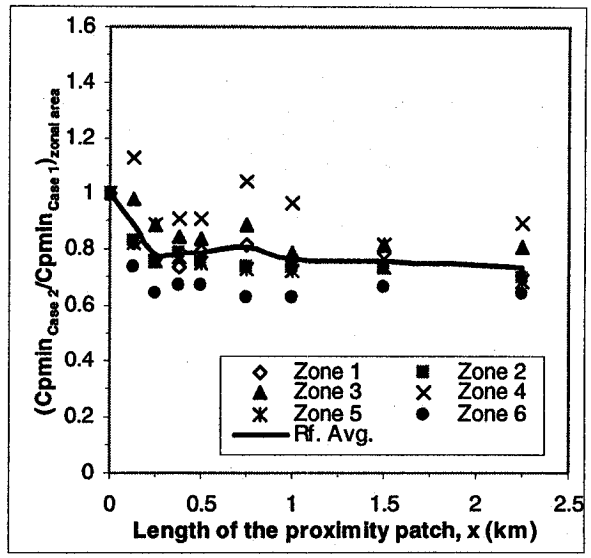

(f) Roof zonal area, ratio of *Cp* min

Fig. 7.14. Most-critical *Cp* ratios for the cases in the test Group 'Suburban patch of variable length directly upstream to the building with OC as remainder (i.e. S(*x*)OR)'.

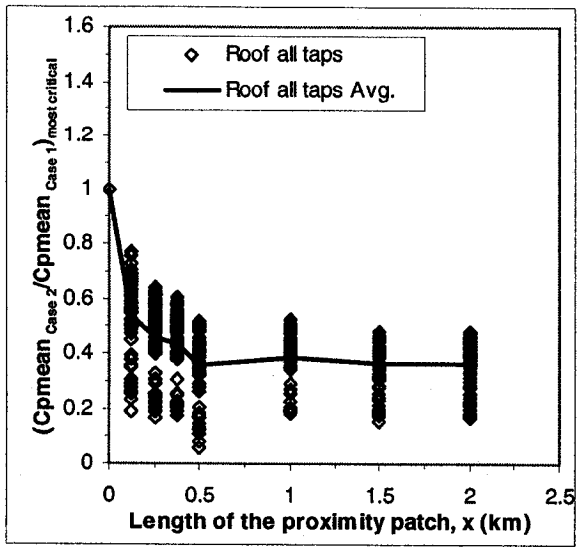

(a) Roof all taps, ratio of *Cp* mean

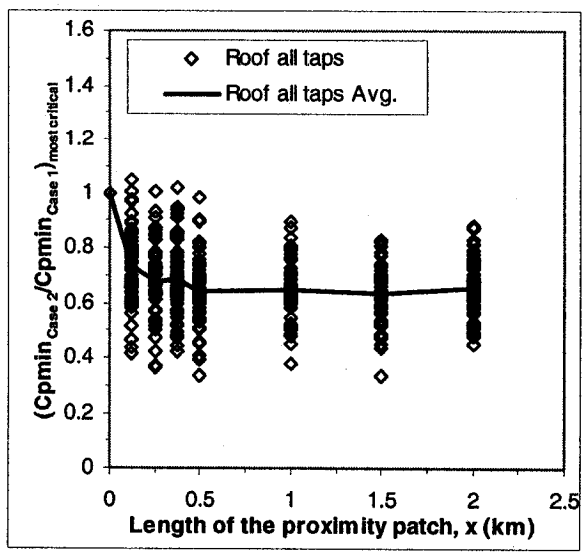

(b) Roof all taps, ratio of *Cp* min

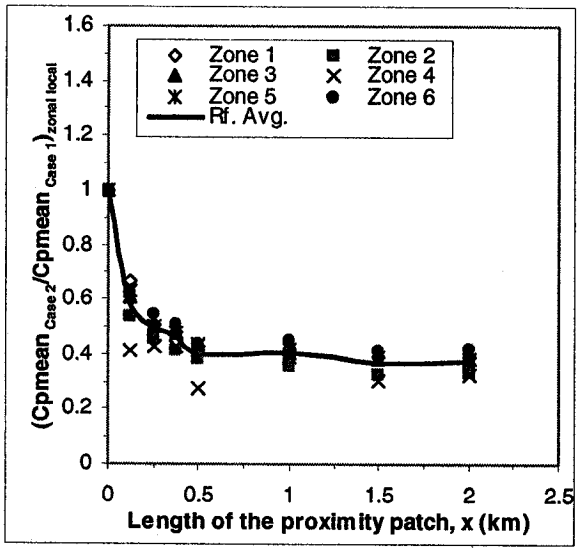

(c) Roof zonal worst local, ratio of *Cp* mean

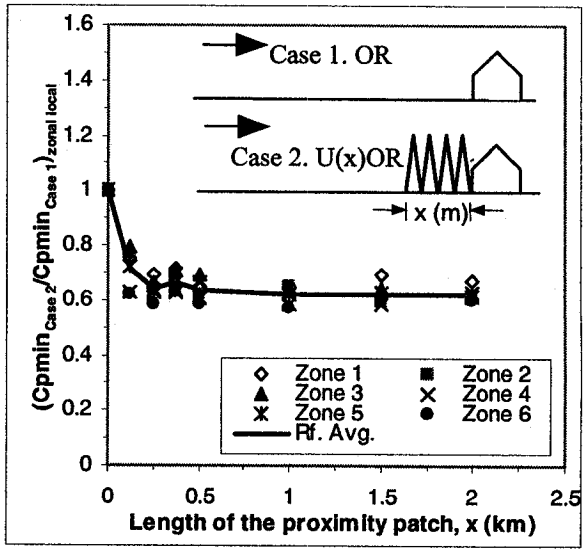

(d) Roof zonal worst local, ratio of *Cp* min

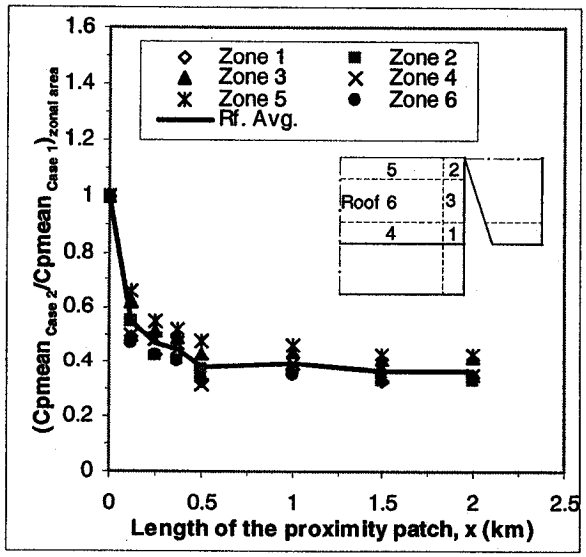

(e) Roof zonal area, ratio of *Cp* mean

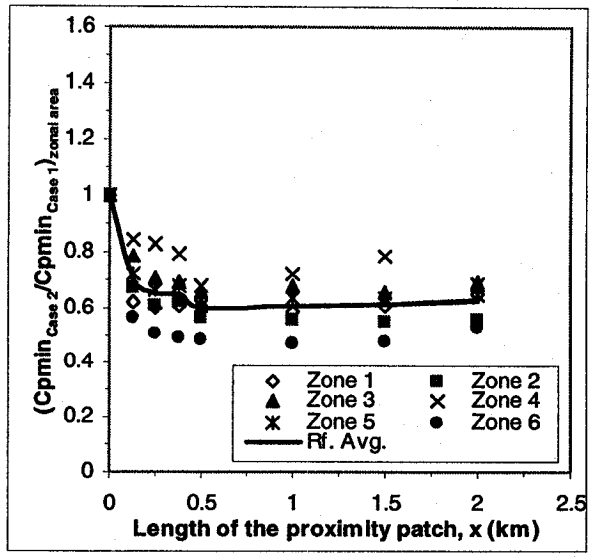

(f) Roof zonal area, ratio of *Cp* min

Fig. 7.15. Most-critical *Cp* ratios for the cases in the test Group 'Urban patch of variable length directly upstream to the building with OC as remainder (i.e. U(*x*)OR)'.

to the first 250 - 500 m long patch directly upstream to the building. This finding is more in favor with the BS 6399-2 (1997) specification (see Table 2.4), although that standard provision may appear less conservative.

Overall comparisons

The overall comparison is just to extract the data-average of local, zonal-local, and zonal-area *Cp* ratios from Figs. 7.11 - 7.15 (where the averages are shown as solid lines), and re-organizes these data into Figs. 7.16 – 7.18 for better description of the variations of the quantities above fetch with a single roughness change.

Figure 7.16 presents the data (in terms of 'local most-critical *Cp* ratio average', 'zonal-local most-critical *Cp* ratio average', and 'zonal-area most-critical *Cp* ratio average') for two test fetch groups '*OC patch of variable length directly upstream to the building with Urban as remainder* (O(*x*)UR)' and '*OC patch of variable length directly upstream to the building with Suburban as remainder* (O(*x*)SR)'. The data of these two fetch groups are presented in the same figure, for these data appear to have similar trends and magnitudes. This figure shows that all these average quantities agree with each other very well, especially when the OC patch gets longer. This is a significant finding because it suggests that different types of *Cp* ratios can be simplified into a simple entity that can be called Upstream Terrain Factor (UTF) after Case and Iysumov (1998) with the following expression,

$$UTF = \frac{load_{Local.Terrain}}{load_{REF.Terrain}} = \frac{Cp_{Local.Terrain}}{Cp_{REF.Terrain}} \tag{7.5}$$

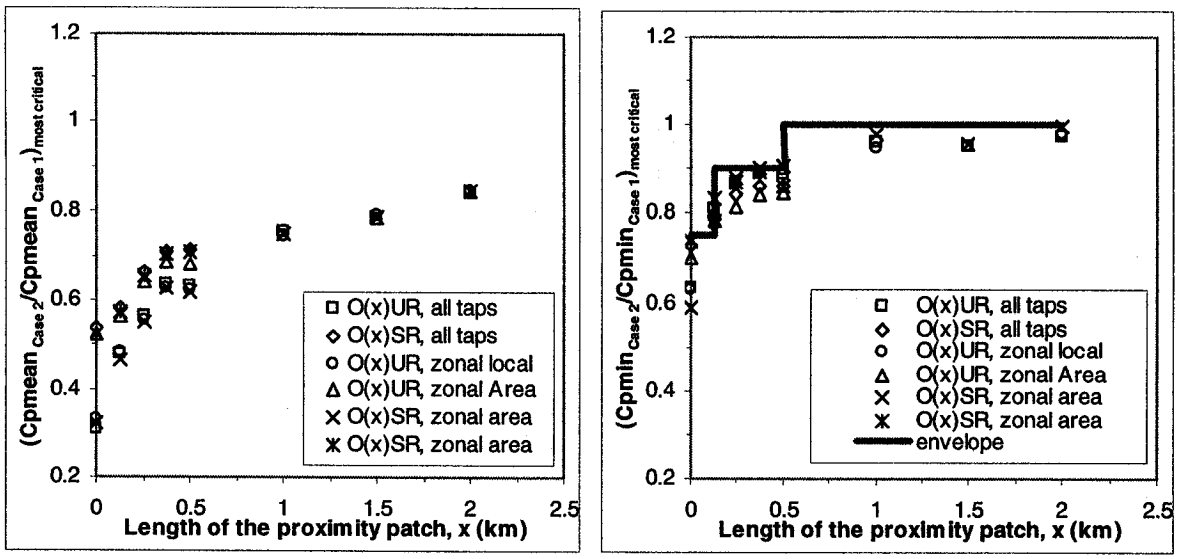

(a) Average lines, mean Cp_{Case2}/Cp_{Case1} (b) Average lines, min Cp_{Case2}/Cp_{Case1}

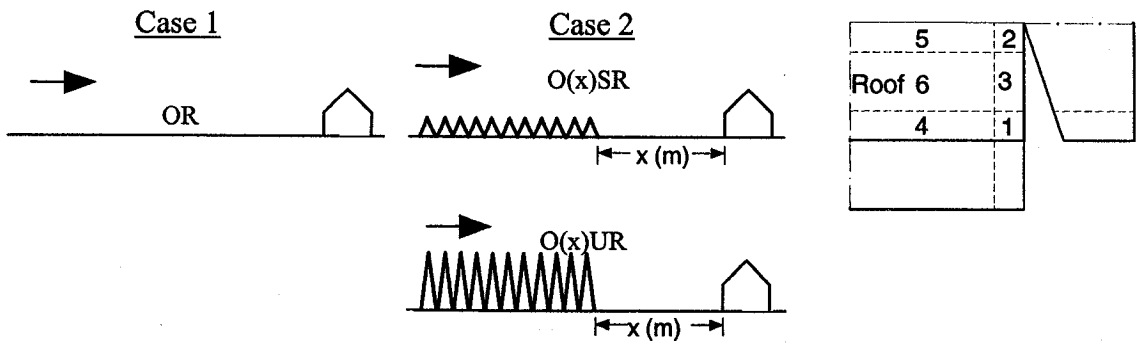

Fig. 7.16. 'Local most-critical *Cp* ratio averages', 'zonal-local most-critical *Cp* ratio averages', and 'zonal-area most-critical *Cp* ratio averages' for two test Groups, 'O(*x*)UR' and 'O(*x*)SR'.

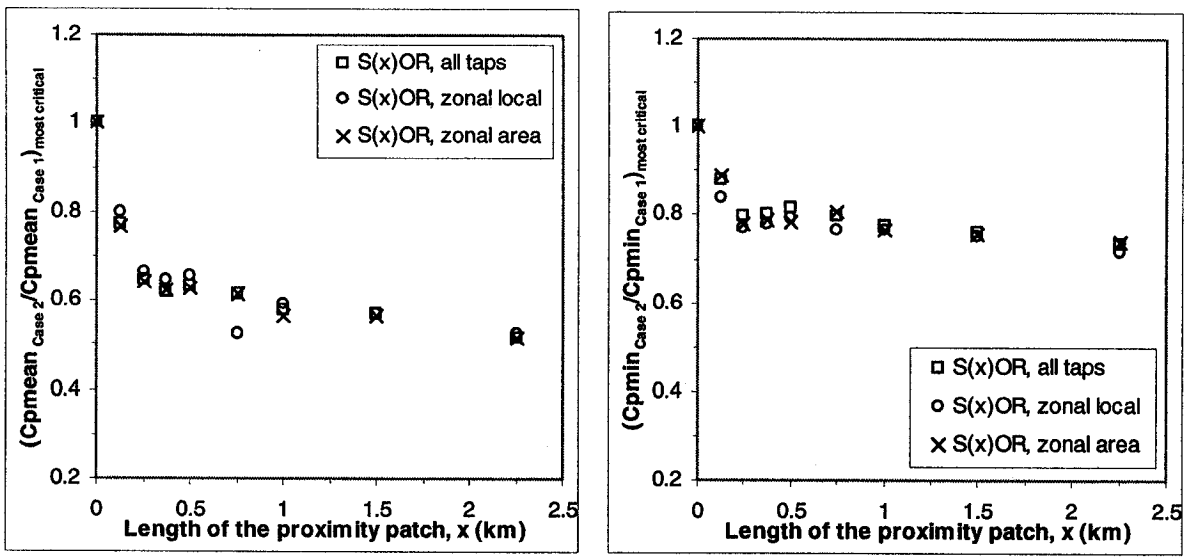

(a) Average lines, mean Cp_{Case2}/Cp_{Case1} (b) Average lines, min Cp_{Case2}/Cp_{Case1}

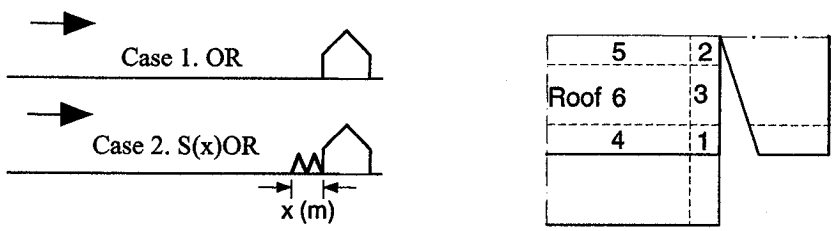

Fig. 7.17. 'Local most-critical *Cp* ratio averages', 'zonal-local most-critical *Cp* ratio averages', and 'zonal-area most-critical *Cp* ratio averages' for the test Group 'S(*x*)OR'.

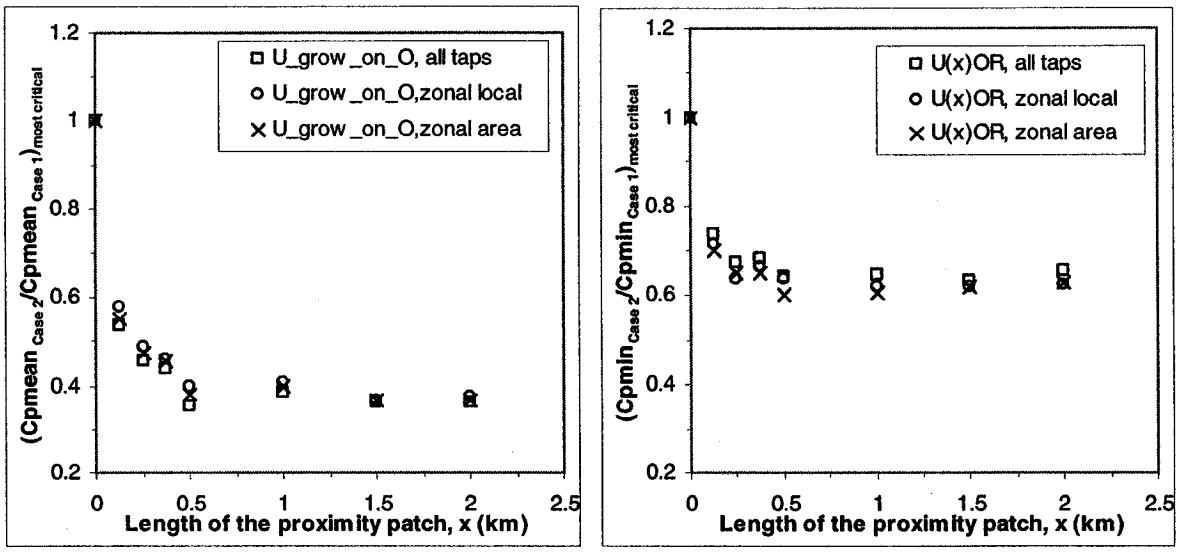

(a) Average lines, mean Cp_{Case2}/Cp_{Case1} (b) Average lines, min Cp_{Case2}/Cp_{Case1}

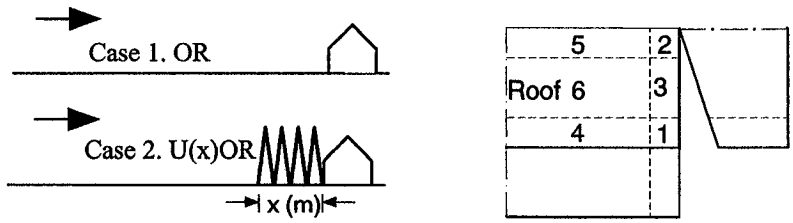

Fig. 7.18. 'Local most-critical *Cp* ratio averages', 'zonal-local most-critical *Cp* ratio averages', and 'zonal-area most-critical *Cp* ratio averages' for the test Group 'Urban patch of variable length directly upstream to the building with OC as remainder (i.e. U(*x*)OR)'.

In words, *UTF* is the ratio of wind load above local terrain to its counterpart above a reference terrain (e.g. OC), both of which can be expressed as *Cp* by reference to a same pressure. It is worth noting that the 'reference terrain' can be any terrain as long as it helps the data comparison.

An envelope line has been attempted in Fig. 7.16b. This envelope shows that the Suburban loads are about of the 75% of the OC loads, and a short OC patch (125 m – 500m) can raise the loads up to 90% of those above OC. A short OC patch directly upstream to the building can increase the loads for the building by about 15%. Such an envelope may be considered for future code update for minimum design load specification.

Figure 7.17 shows the results for the fetch group '*Suburban patch of variable length directly upstream to the building with OC as remainder* (S(*x*)OR)'. Again, Fig. 7.17 justifies the concept of UTF since the different *Cp* quantities show similar magnitudes.

Figure 7.18 gives similar findings with those of Fig. 7.17, except that the Urban peak loads are about 60% - 65% of those of OC. However, taking into account that a smaller population of low-rise buildings are associated with Urban, and some Urban loads have similar magnitudes as those of Suburban (see Fig. 7.8), it is not necessary to give separate treatment to Urban apart from Suburban. Therefore, the provisions of ASCE 7-02 that consider Suburban and Urban as one terrain class are deemed appropriate. It should be noted that the definition of NBCC-1995 on this regard is even more general than that of ASCE 7-02.

In general, the roughness characteristic and length of the patch directly upstream to the building is found very important for terrain/exposure classification from the perspective of low-rise building load estimation.

7.5 Results of wind loads above fetch with multiple roughness changes

Previous discussions have shown that the loads are mainly sensitive to the terrain roughness within in the first few hundred meters directly upstream to the building site. However, frequently there can be roughness changes inside this fetch section. The Suburban or Urban terrain with OC patches (namely large parking lots, water bodies and parks etc) can be easy found in terrain in reality. Therefore, it is of interest to study the load variation above fetch with OC patch(es) indirectly upstream from the site but within the 500 m section.

Figure 7.19 compares the *Cp* results above OC with those above the fetch case '*Suburban terrain with a 125 m long OC patch and 125 m upstream away from the building*'. As shown in this figure, although it is within the first few hundred meter fetch section, the OC patch of 125 m long and of 125 m upstream away from the building does not cause significant load changes.

Figure 7.20 shows that the OC patch of 375 m long has caused some load increase. The fetch configuration in Fig. 7.20 is the same as that of Fig. 7.19, except that the OC patch is 375 m long instead. Findings similar to those in Figs. 7.19 and 7.20 can also be found in Figs. 7.21 and 7.22.

Figure 7.23 compares, in terms of local most-critical UTF, zonal-local UTF and

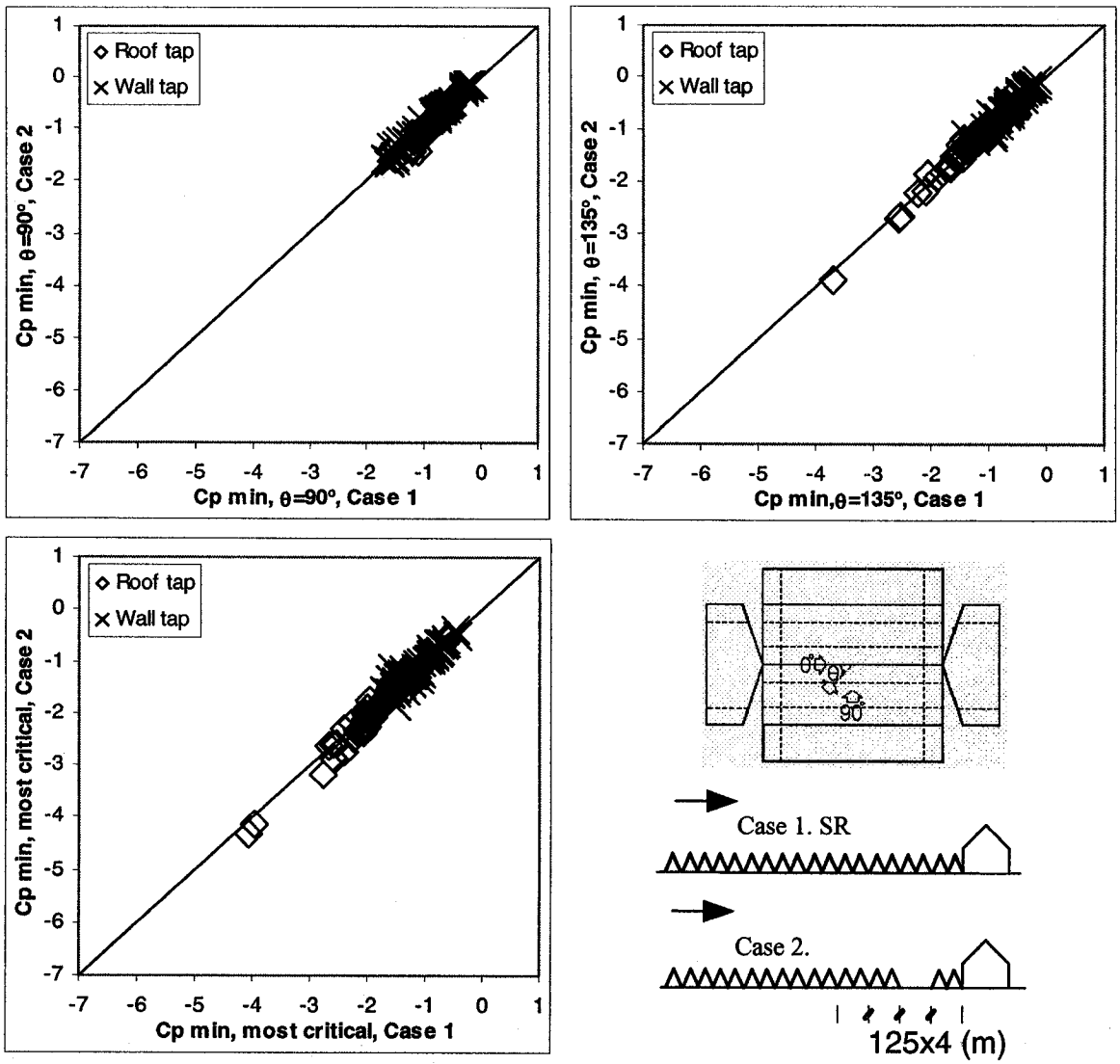

Fig. 7.19. Local *Cp* min results above Case (1) Suburban and Case (2) 'Suburban terrain with a 125 m long OC patch and 125 m upstream away from the building'.

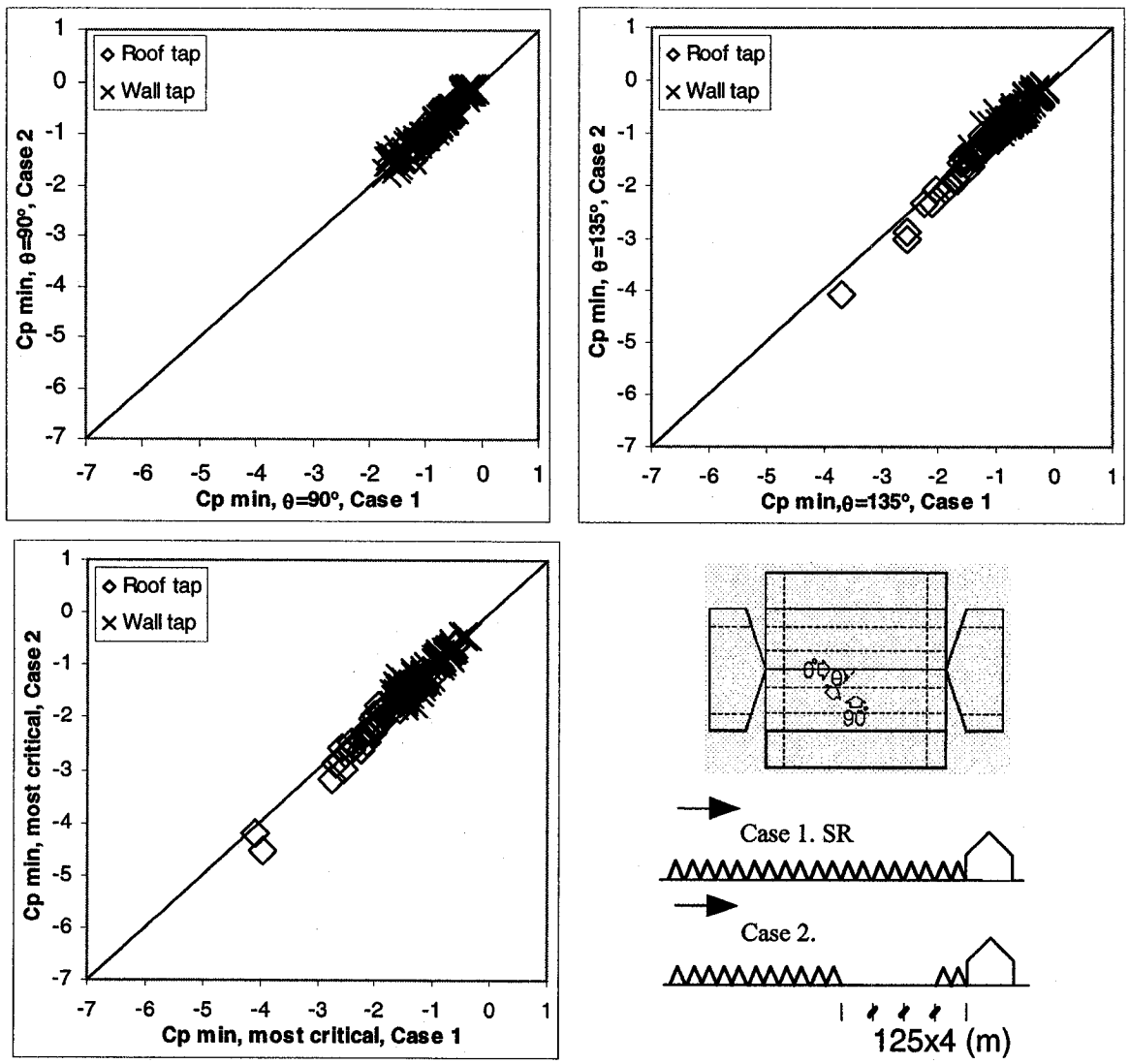

Fig. 7.20. Local *Cp* min results above Case (1) Suburban and Case (2) 'Suburban terrain with a 375 m long OC patch and 125 m upstream away from the building'.

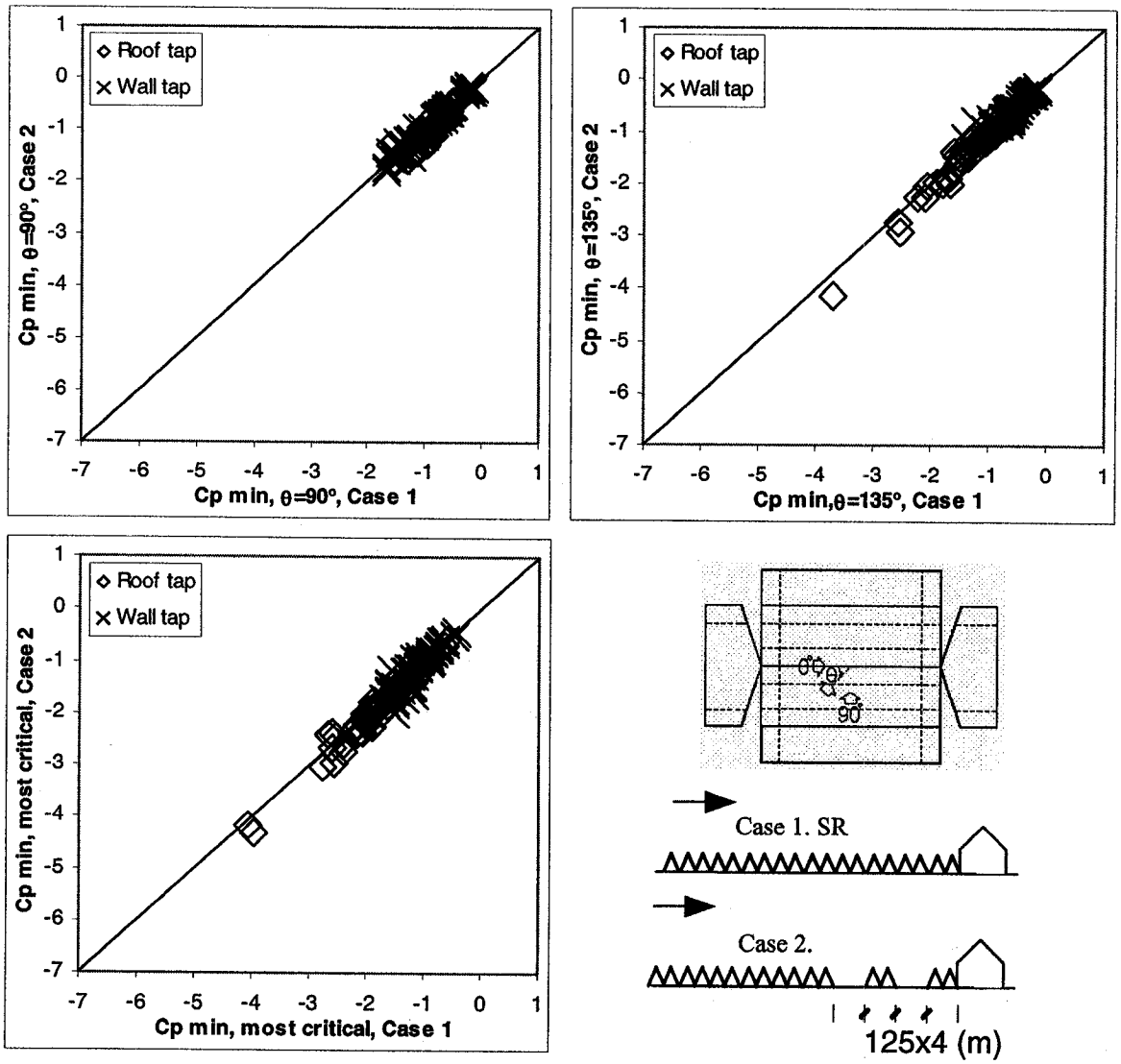

Fig. 7.21. Local *Cp* min results above Case (1) Suburban terrain and above Case (2) 'Suburban terrain with OC patches totally 250 m long and at least 125 m upstream away from the building'.

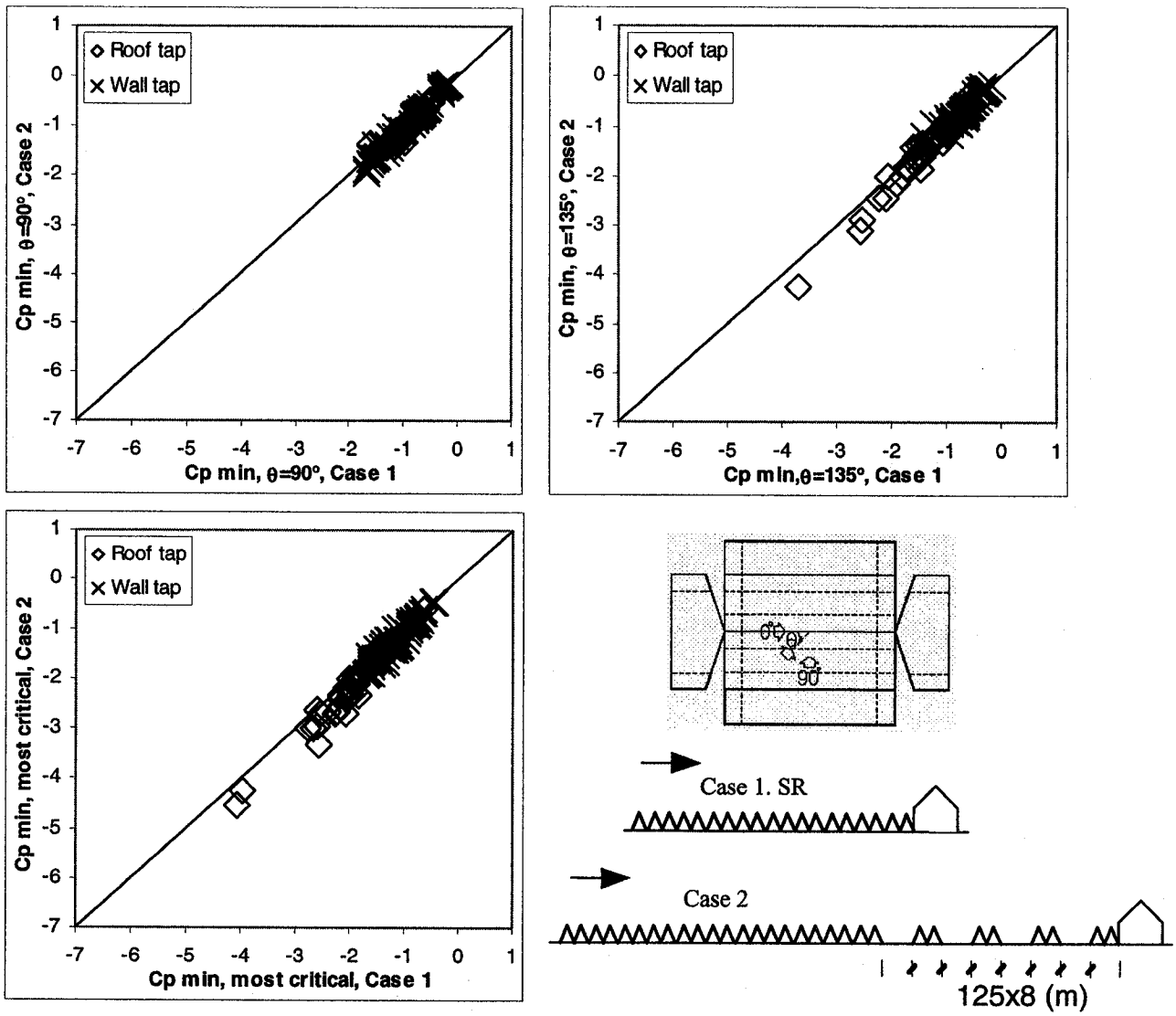

Fig. 7.22. Local *Cp* min results above Case (1) Suburban terrain and above Case (2) 'Suburban terrain with OC patches totally 500 m long and at least 125 m upstream away from the building'.

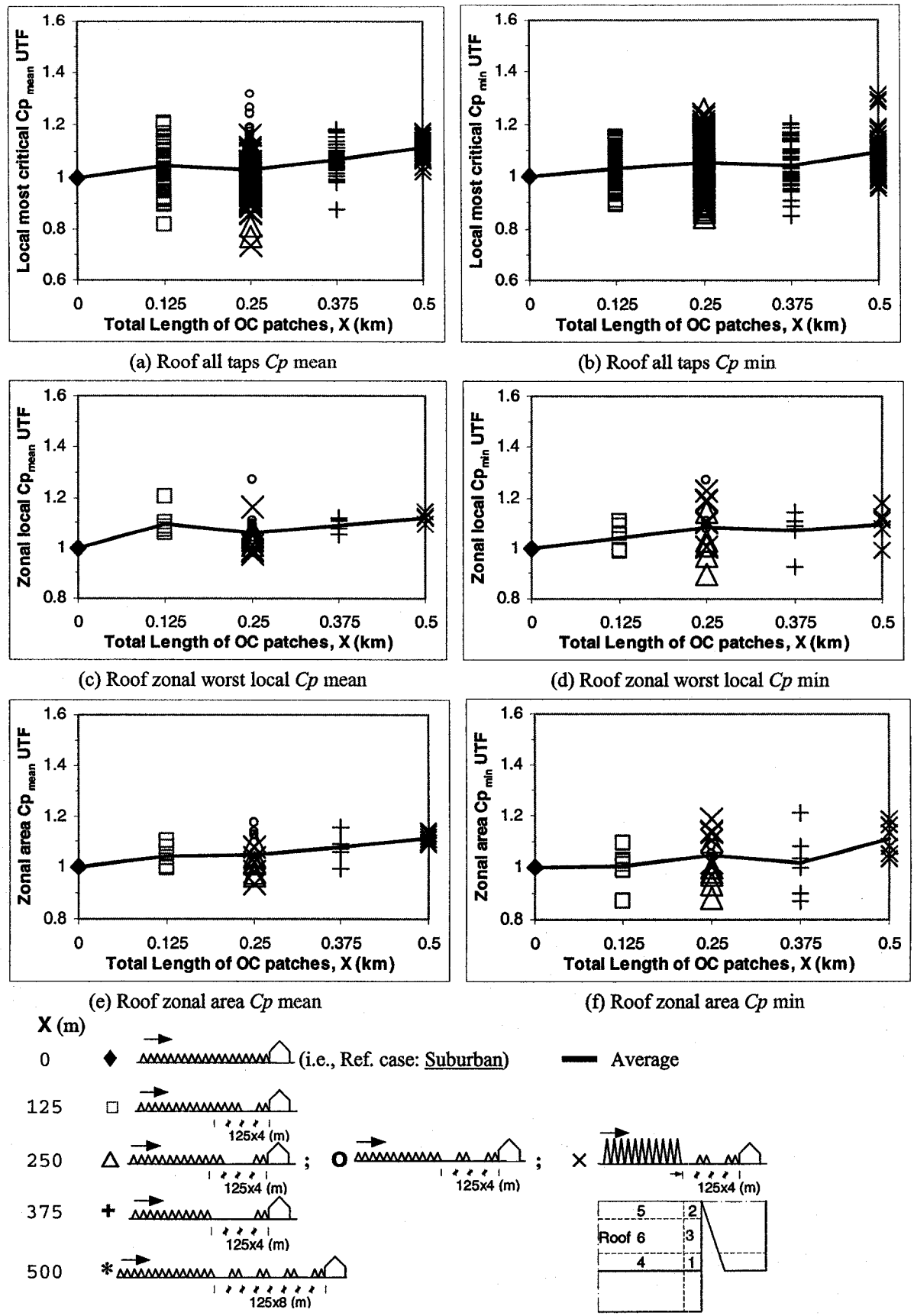

Fig. 7.23. Most-critical *Cp* ratio (i.e. UTF) of the cases that have a 125 m long Suburban patch directly upstream to the building.

zonal-area UTF, the wind load variations above the fetches that commonly have a Suburban patch of 125 m long directly upstream to the building. It should be noted that the solid lines in Figs. 7.23a - 7.23f are the overall averages of all of the data points of one fetch, or of several fetches that commonly have OC patches of the same total length. When the total length of the open patches reaches 500 m, the wind loads get about 10% higher than those of Suburban. However, by comparison to Fig. 7.16, it can be found that 500 m OC patches indirectly upstream to the building may not have effect as strong as 125 m OC patch directly upstream of the building.

Figure 7.24 compares (also in terms of local most-critical UTF, zonal-local UTF and zonal-area UTF) the wind load variations above another fetch group that commonly have a 250 m Suburban patch directly upstream to the building. The total OC patch length also varies from 0 – 500 m in these cases. The results of Fig. 7.24 are quite similar to those of Fig. 7.23, but the loads appear less sensitive to the length/location of the OC patch(es) than if the Suburban patch is just 125 m long.

The four data diagrams of Fig. 7.25 contain the same type of information as the diagrams (a) and (b) of Fig. 7.23 do, and these four diagrams of Fig. 7.26 contain the same kind of information as the diagrams (c) through (f) of Fig. 7.23 do. In other words, Figs. 7.25 and 7.26 convey the same kind of information as Fig. 7.23 does. However, the diagrams (c) and (d) of Fig. 7.25 can give a closer look on how the data of average vary with these three special terrain configurations that are common in the total OC patch length (equal to 250 m) and the closest patch distance to the building, but different in how the OC patches are located.

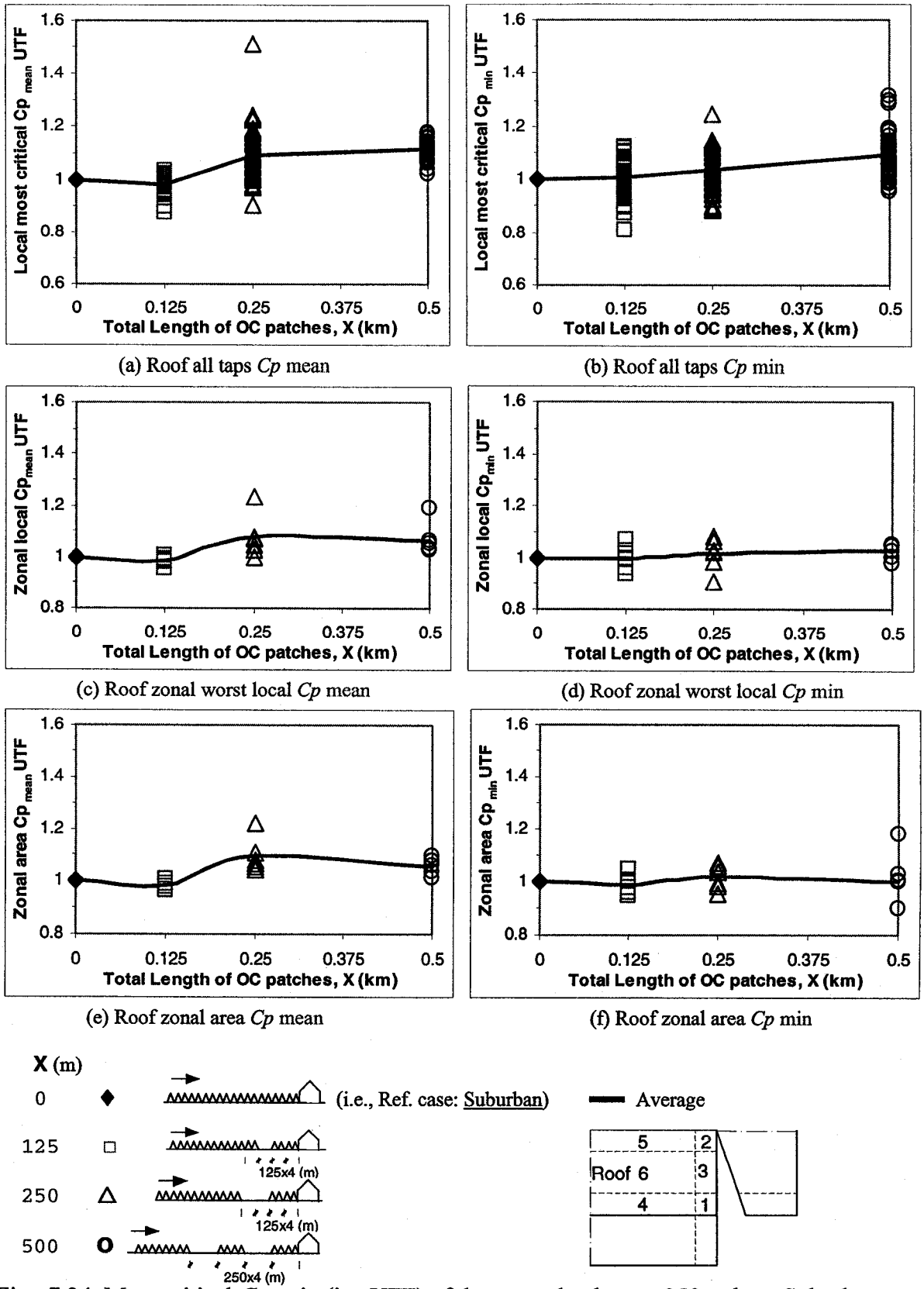

Fig. 7.24. Most-critical *Cp* ratio (i.e. UTF) of the cases that have a 250 m long Suburban patch directly upstream to the building.

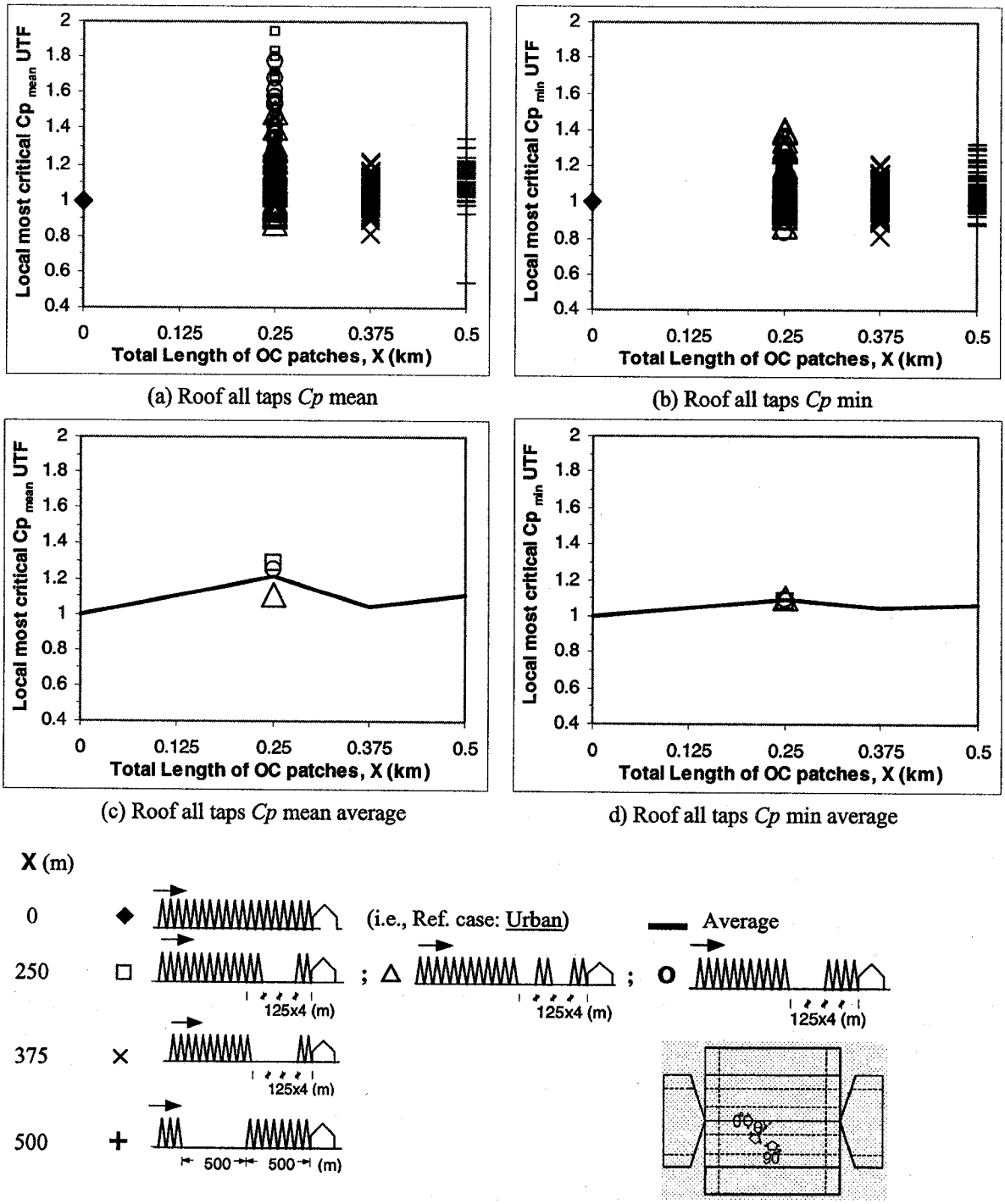

Fig. 7.25. Most-critical *Cp* ratio (i.e. UTF) of the cases that have OC patches on otherwise Urban terrain.

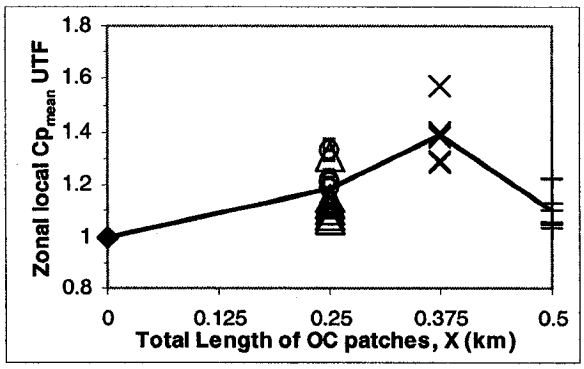

(a) Roof zonal local *Cp* mean

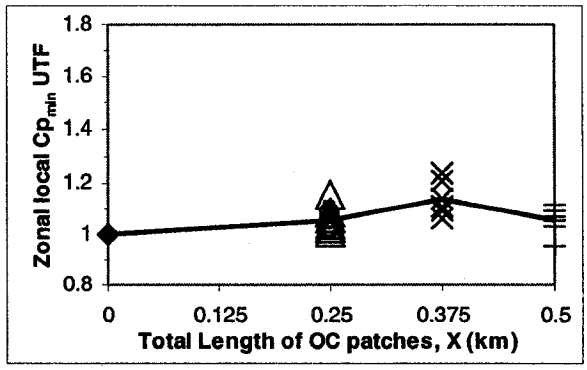

(b) Roof zonal local *Cp* mean average

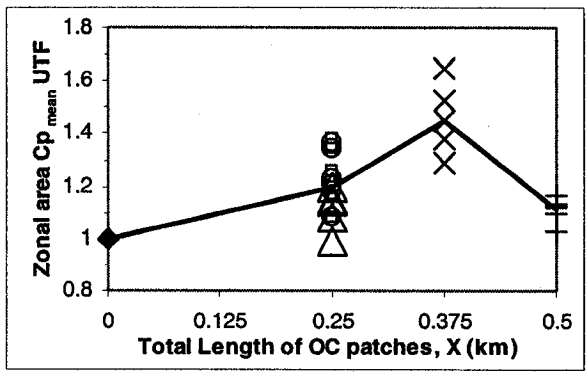

(c) Roof zonal local *Cp* min

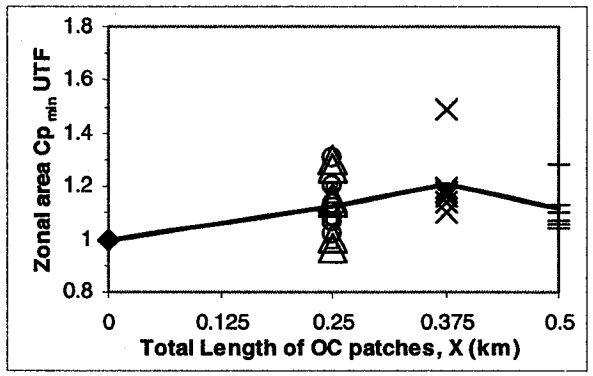

(d) Roof zonal local *Cp* min average

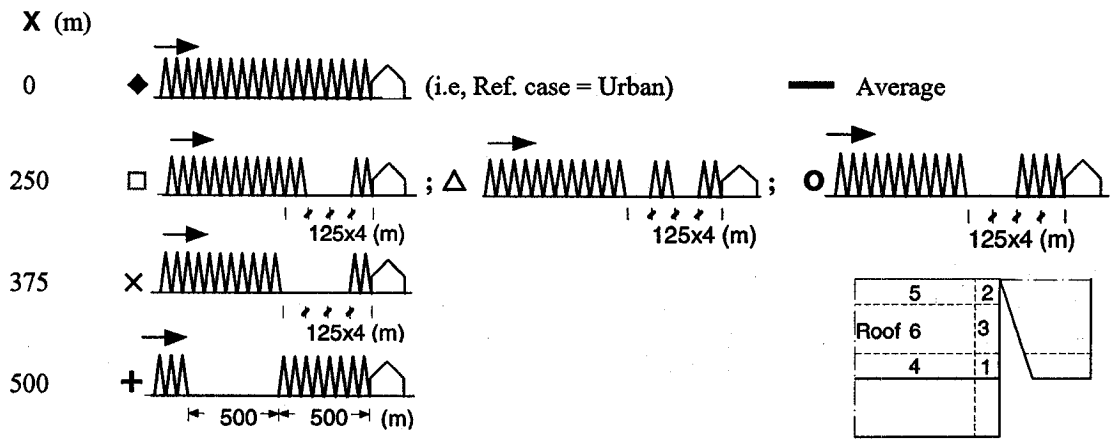

Fig. 7.26. Most-critical *Cp* ratio (i.e. UTF) of the cases that have OC patches on otherwise Urban terrain.

The three points in the diagrams (c) and (d) of Fig. 7.25 show similar values, especially for the peaks; therefore, one can say that if the total length of the OC patch(es) is the same and the closest distance of the OC patch(es) to the building is also the same, then the load effects of the OC patches are determined. That is to say, loading is a function of the total OC patch length but not the pattern of roughness configurations. Fig. 7.26 gives the similar finding.

Diagrams (a) and (c) of Fig. 7.26 show that the 375 m OC patch indirectly upstream to the building on otherwise Urban terrain increases the mean loads about 40%. This phenomenon is special but not general, since the significant mean-load increase is not found in Fig 7.23. Moreover, this phenomenon is not deemed important, since Urban terrain has been determined to merge with Suburban, thus absorbs a safety margin allowing certain load variation/increment (the Suburban average mean load is found about 1.8 times the Urban counterpart as shown in Fig. 7.12).

In general, the results of Figs. 7.23 - 7.26 suggest that, if the general terrain roughness characteristics are known, then totally 250 m - 375 m long OC patch(es) upstream to, and 125 m away from, the building on otherwise Suburban terrain can be deemed as case-sensitive depending on which load quantity is of interest; in such situation the maximum load increase is about 10% from that of Suburban terrain (cf. Fig. 7.23). It should be noted that the minimum patch length considered in this study is 125 m. On the other hand, if the general terrain roughness characteristics are known, then totally 250 m long OC patch(es) indirectly upstream to, and 250 m away from, the building on otherwise Suburban terrain can be neglected (cf. Fig. 7.24). OC patches indirectly upstream to the building in otherwise Urban terrain can be generally neglected, if Urban is classified as in

the Suburban-Urban terrain category. Furthermore, the variation of terrain roughness 500 m upstream away from the building is not considered significant.

In practice, the effects of the above-mentioned OC patch variations in otherwise Suburban terrain, which may introduce a load increase from that of Suburban up to 10%, can be accounted for by simply adding a safety margin into the Suburban design load specification. Of course, this treatment does not exclude the possibility of using the present database as reference for determining loads for special cases.

7.6 Discussion on the current code issues

On the minimum fetch length requirement

Although a number of discrepancies have been found among various wind standards and codes of practice, this study would consider that all those specifications are of certain rationale. For instance, regarding the *minimum design fetch length*, the specification of a longer length (e.g. that of NBCC-1995) may be appropriate as far as mean load is considered (see Fig.7.16a), while the shorter specification (cf. that of BS 6399-2 1997) is deemed appropriate for peak loading (see Fig. 7.16b), which is more important to design.

This study intends to unify the specification for *minimum design fetch length* as 300 – 400 m (note most of the present cases are focusing on the roughness variation in the first 500 m). Figures 7.11 - 7.12 and 7.14 - 7.18 show that the load quantities (i.e. local, zonal-local, and zonal-area) stop changing drastically when the length is within this range, especially for the roof minimum *Cp* that is considered a critical factor for low-rise building. This unification is deemed effective and conservative for any types of roughness change (i.e. OC-to-Suburban, Urban-to-OC etc.) Moreover, Figs. 7.23 – 7.26

affirm that the first terrain section directly upstream to the building dominate the loads, while further upstream roughness configurations are not considered significant. The present finding agrees well with the results of Holmes (1994) and of Young and Vickery (1998).

On Suburban design load specification

A track back has found that there is a hidden assumption in ASCE 7-02 for cladding load estimation, namely, ASCE 7-02 simplifies the following (correct) prototype equation,

$$p = q_{Suburban} Cp'_{Suburban} \tag{7.6}$$

into the equation of practice as,

$$p = q_{Suburban} Cp_{OC} \tag{7.7}$$

This simplification may cause underestimation of the Suburban design loads, if the term of practice Cp_{OC} has value (significantly) lower than that of the prototype term $Cp'_{Suburban}$. As shown in Figs. 7.3 and 7.4b, the present Cp_{OC} values are indeed considerably lower than those of $Cp'_{Suburban}$. Therefore, the ASCE 7-02 simplification should cause underestimation of the Suburban design loads.

A careful examination of the present data suggests that the Suburban-Urban exposure factor may be considered as 0.8. Figs. 7.14 and 7.17 show that the Suburban exposure factor should be between 0.75 and 0.80, i.e. the Suburban design load estimate is 75% - 80% of its OC counterpart; furthermore, if the effects of OC patch(es) indirectly upstream to the building are absorbed in the present design load formulation, the present Suburban exposure factor should be added with a safety margin. Thus this factor is specified as 0.8. Furthermore, since it is appropriate to treat Suburban and Urban as one terrain class, this

0.8 factor is considered effective for the Suburban-Urban class. This number is slightly lower than 0.85 defined in ASCE 7-95, but significantly higher than that in ASCE 7-02, which yields a design load estimate just 75% of that of ASCE 7-95. This study agrees well with Case and Isyumov (1998) who stated that an upstream suburban exposure experiences approximately 15% - 25% lower loads when compared to OC exposure.

7.7 Conclusion

This chapter has discussed the results of the low-rise building loads above fetch with roughness changes, and tackled the pertinent code issues/discrepancies. It is found that ratio of Cp value of one terrain configuration over Cp value of another terrain configuration does not vary significantly with building envelope location, so that it is possible to use a single UTF number to account for the loading level of one terrain configuration in comparison to that of OC terrain. It is also found that the patch directly upstream to the building has dominant effects on wind loading, and the minimum fetch length requirement (for OC, Suburban or Urban patch to qualify as full homogeneous terrain) may be unified as about 300 - 400 m irrespective of the type of roughness changes (either smooth-to-rough or rough-to-smooth), so that local terrain information suffices the design of local wind load. This study agrees with ASCE 7-02 that Suburban and Urban can be grouped in one class, namely, Suburban-Urban. On the other hand, it is found that the ASCE 7-02's specification on this terrain class's exposure factor is considerably low. A slight reduction of the ASCE 7-95's 0.85 factor into a 0.8 factor would be more appropriate. In the fetch section of 500 m directly upstream to the site, there may be small roughness changes in otherwise Suburban (or Urban) terrain exposure.

Such roughness changes can be neglected, especially after a safety allowance factor has been taken into account formulating the 0.8 Suburban-Urban exposure factor. It should be emphasized however, that the results of this chapter are effective just for low-rise buildings.

Chapter 8 Conclusions and recommendations of future study

Terrain exposure, which is deemed a direct factor in the design wind load estimation function (Eq. (1.1)), has not been well characterized in general, and a number of issues/discrepancies exist in the code terrain-related provisions in particular. The emphasis of this dissertation is therefore on better modeling the variations of speed and turbulence intensity (*Iu*) profiles, as well as the variation of the low-rise building wind loading, as a function of terrain roughness change. The thesis consists of five major parts: (1) introduction, theoretical background and comprehensive review (Chapters 1 and 2), (2) experimental and numerical methodology (Chapters 3 and 4), (3) development of a speed profile estimation model for inhomogeneous terrain with small-scale roughness changes (Chapter 5), (4) development of an *Iu* model for predicting speed profile above fetch with small-scale roughness changes (Chapter 6), and (5) evaluation of the low-rise building wind loads above typical homogeneous terrain and the terrain variations (Chapter 7). Summaries of findings from each chapter are collapsed here to draw the final conclusions of this study.

8.1. Concluding remarks

The results of this study can be summarized as follows:

(1) Review of the previous theory has shown that a number of assumptions developed for homogeneous terrain have been taken into the numerical studies (e.g. Deaves 1981a) whose results have been adopted into a number of wind standards and

codes of practice (e.g. ASCE 7-02) for inhomogeneous terrain. However, these numerical assumptions may be oversimplified, especially when the local small-scale roughness changes are found significant for design wind loads. Therefore, it is not surprising to find that a number of issues or discrepancies in the code terrain-related provisions (e.g. the model incompatibility, and the discrepancies on the specifications on the minimum fetch length requirement, and on the Suburban/Urban exposure factor) need solutions. This critical review points out the importance and necessity of an experimental investigation with emphasis on appropriate modeling of the small-scale roughness changes close to the site.

(2) Altogether 69 fetch configurations have been tested in the present wind tunnel experimental study and an extensive database has been constructed. An array of wind tunnel and numerical simulation techniques have been developed for this study.

(3) Following the present wind tunnel and numerical results, a wind speed model is proposed for describing the effects of upstream terrain exposure on speed profile. The model uses N sections corresponding to N different roughness patches of the upstream terrain within a range no more than 4 km from the site. Recognition of the patch type and patch roughness value (z_o and/or α) can be referenced to a recently developed roughness classification (Davenport et al 2000). The gradient height information is available from a number of ASCE standard releases. Its validation has been attempted by using a limited amount of field data available with satisfactory results.

(4) A model is also proposed and can describe the *Iu* profile above complex roughness scenarios. This model takes into account the same terrain information as the proposed speed model does, except that the *Iu* model requires the value of patch characteristic *Iu*(10) value (note the patch power law exponent is required by the proposed speed model.) Validation of this *Iu* model is attempted by utilizing a very limited amount of field data; generally speaking, the comparisons are satisfactory.

(5) For low-rise buildings, the present wind tunnel measurements are used to clarify a number of pertaining code issues. A short patch directly upstream to the building can have significant impacts on the wind loads. The code minimum fetch length requirement for OC, Suburban or Urban patch to qualify into homogeneous terrain may be unified as 300 - 400 m for low-rise buildings. It is affirmed that Suburban and Urban can be regarded as one terrain class. On the other hand, the present wind tunnel results recommend a Suburban-Urban exposure factor as 0.8, i.e. the design loads for Suburban or Urban terrain is 80% of the OC counterparts. This result is closer to the ASCE 7-95 specification of 0.85 than to the ASCE 7-02 provision that is in effect considerably lower.

8.2 Contributions

Contributions of the present research work can be summarized as follows:

(1) This is probably the first time that a speed model is developed upon data resulted from both wind tunnel testing and numerical simulation. This model accounts for the more-realistic local, small-scale patch roughness changes that have been

found of significant effects on wind loading. The present model appears to compare well with a limited amount of full-scale data with satisfactory results. Furthermore, the present model has the simple and easy –to-use power law form that is compatible to the longstanding ordinary power law model (see NBCC-1995 and ASCE 7-02). The generalized power law model is deemed as a seamless extension of the ordinary power law from applicable to homogeneous terrain to applicable for inhomogeneous terrain. This model can be applied to NBCC, the terrain-related provisions of which have not been updated for a long period of time since its 1995 edition. This model may solve the issue in ASCE 7-02 in which the power law model and the ESDU (82026) model, which do not conform to each other, coexist in this one standard.

(2) Currently, wind standards and codes of practice do not provide models for estimating *Iu* profile above inhomogeneous terrain, but simply treat inhomogeneous terrain as homogeneous for *Iu* profile estimation. This study attempts to contribute an analytical and more practical model on this regard.

(3) The present study has carried out a systematic experiment investigating the low-rise building wind load variation as function of roughness change. The data are used to clarify some discrepancies in the code terrain-related provisions applicable for low-rise buildings, which are pertaining to the minimum length requirement for a patch to qualify as fully matured terrain and to the Suburban/Urban exposure factor.

(4) A number of innovative techniques have been developed for this study. For instance, the graph-presentation function of the VBA-ACAD-Word data mapping

program post mass numerical data and text onto drawing template of any plan shape, while most current commercial software is not developed for this functionality.

8.3 Recommendation for future study

Potential improvements and possible extensions of the present study are:

(1) More full-scale evidences, whenever found, should be used to further validate or calibrate the proposed models. Due to lack of sufficient full-scale evidence, the power law exponent of -0.4 in the *Iu* model may be subject to further calibration in particular. It should be noted that a possible calibration work will not be able to change the characteristics of this original model.

(2) The present speed and *Iu* models require evaluation of the fetch length up to 4 km (upstream from the building of interest), as well as of all the distinctive patches within this fetch length. More study may help to find appropriate methods which allow a reduction of this length and simplification of the patches above this length for calculation purposes.

(3) The present wind tunnel results can be used for better understanding the wind tunnel floor modeling.

(4) A huge database has been constructed after the present wind tunnel experiments; this database may be re-visited, if promising data-mining technique has been found.

(5) The present results can suggested for future update of terrain-related provisions in wind standards and codes of practice.

References

- Antonia, R.A. and R.E. Luxton. 1971. The response of a turbulent boundary layer to a step change in surface roughness Part 1. Smooth to rough. J. Fluid Mech. 48: 721-761.

- Antonia, R.A. and R.E. Luxton. 1972. The response of a turbulent boundary layer to a step change in surface roughness Part 2. Rough to Smooth. J. Fluid Mech. 53: 737-757.

- Architectural Institute of Japan (AIJ). 1996. Recommendation for loads on buildings. Architectural Institute of Japan.

- American Society of Civil Engineers (ASCE). 1995. Minimum design loads for buildings and other structures. ASCE 7-95. American Society of Civil Engineers.

- American Society of Civil Engineers (ASCE). 1998. Minimum design loads for buildings and other structures. ASCE 7-95. American Society of Civil Engineers.

- American Society of Civil Engineers (ASCE). 1999. ASCE Standard – Wind tunnel testing for buildings and other structures. American Society of Civil Engineers.

- American Society of Civil Engineers (ASCE). 2003. Minimum design loads for buildings and other structures. SEI/ASCE 7-02. American Society of Civil Engineers.

- Baker, C.J. 2004. Wind overturning study: Full-scale and wind tunnel measurements to determine the aerodynamic force and moment parameters of Mark 3 and Class 390 vehicles – Overview report. Rail Safety and Standards Board, Evergreen House, 160 Euston Road London NW1 2DX. (Downloaded from internet address http://www.rssb.co.uk/ on August 2nd, 2004).

- Banks. D, R.N. Meroney, P.P. Sarkar, Z. Zhao and F. Wu. 2000. Flow visualization of conical vortices on flat roofs with simultaneous surface pressure measurement. J. Wind Eng. Ind. Aerodyn. 84: 65-85.

- Bottema, M. 1996. Roughness parameters over regular rough surfaces: Experimental requirements and model validation. J. Wind Eng. Ind. Aerodyn. 64: 249-265.

- Bradley, E.F. 1968. Micrometeorological study of velocity profiles and surface drag in the region modified by a change in surface roughness. Quart. J. Roy. Meteorol. Soc. 94: 361-379.

- British Standards Institution. 1997. BS 6399-2: Loading for buildings – Part 2: Code of practice for wind loads. British Standards Institution on ERC Specs and Standards.

- Case, P.C. and N. Iysumov. 1998. Wind loads on low buildings with 4:12 gable roofs in open country and suburban exposures. J. Wind Eng. Ind. Aerodyn. 77&78: 107-118.

- Cermak J.E. and L.S. Cochran. 1992. Physical Modelling of the Atmospheric Surface Layer. J. Wind Eng. Ind. Aerodyn. 41-44: 935-946.

- Cook, N.J. 1985. The designer's guide to wind loading of building structures, Part 1, Butterworths, London.

- Cook, N.J. 1997. The Deaves and Harris ABL model applied to heterogeneous terrain. J. Wind Eng. Ind. Aerodyn. 66: 197-214.

- Counihan, J. 1971. An improved method of simulating an atmospheric boundary layer in a wind tunnel. Atmos. Environ. 3: 197-214.

- Davenport, A.G., S. Grimmond, T. Oke and J. Wieringa. 2000. The revised Davenport roughness classification for cities and sheltered country. Third Symposium on the Urban Environment. Davis, California. Aug. 14-18, 2000. pp. 7-8.

- Deaves, D.M. 1981a. Computations of wind flow over changes in surface roughness. J. Wind Eng. Ind. Aerodyn. 7:65-94.

- Deaves, D.M. 1981b. Terrain-dependence of longitudinal r.m.s. velocities in the neutral atmosphere. J. Wind Eng. Ind. Aerodyn. 8:259-274.

- Deaves, D.M. and R.I. Harris. 1978. A mathematical model of the structure of strong winds. Construction Industry Research and Information Association. CIRIA Report 76. 6 Storey's Gate, London, SW1P 3AU.

- Engineering Sciences Data Unit (ESDU). Data Item 82026. Strong winds in the atmospheric boundary layer. Part 1: hourly-mean wind speeds. Engineering Sciences Data Unit.

- Engineering Sciences Data Unit (ESDU). Data Item 84030. Longitudinal turbulence intensities over terrain with roughness changes. Engineering Sciences Data Unit.

- Farrugia, R.N. 2003. The wind shear exponent in a Mediterranean island climate. Renewable Energy. 28:647-653.

- Fiedler, F. and H.A. Panofsky. 1972. The geostrophic drag coefficient and the 'effective' roughness length. Quart. J. R. Met. Soc. 98: 213-220.

- Garratt, J.R. 1990. The internal boundary layer – a review. Boundary-Layer Meteorology. 50: 171-203.

- Grimmond, C.S.B. and T.R. Oke. 1999. Aerodynamic properties of urban areas derived from analysis of surface form. J. Applied Meteorology. 38: 1262-1292.

- Ho, T.C.E. 1992. Variability of low building wind loads. Ph.D. thesis. The University of Western Ontario, Canada.

- Ho, T.C.E., D. Surry and A.G. Davenport. 1991. Variability of low building wind loads due to surroundings. J. Wind Eng. Ind. Aerodyn. 38: 297-310.

- Holmes, J.D. 1994. Wind pressure on tropical housing. J. Wind Eng. Ind. Aerodyn. 53: 105-123.

- Holmes, J.D. 2001. Wind loading of structures. Spon Press.

- Hussain, M. and B.E. Lee. 1980. A wind tunnel study of the mean pressure forces acting on large groups of low-rise buildings. J. Wind Eng. Ind. Aerodyn. 6: 207-225.

- Jia, Y. and B.L. Sill. 1998. Pressures on a cube embedded in a uniform roughness field of variable spacing density. J. Wind Eng. Ind. Aerodyn. 77&78: 491-501.

- Kato, N., T. Ohkuma, J.R. Kim, H. Marukawa and Y. Niihori. 1992. Full scale measurements of wind velocity in two urban areas using an ultrasonic anemometer. J. Wind Eng. Ind. Aerodyn. 41-44:67-78.

- Kawai, H. and G. Nishimura. 1996. Structure of conical vortices related with suction fluctuation on a flat roof in oblique flow. J. Wind Eng. Ind. Aerodyn. 60: 211-225.

- Keifer, H. and E.J. Plate. 1998. Modelling of mean and fluctuating wind loads in built-up areas. J. Wind Eng. Ind. Aerodyn. 74-76: 619-629.

- Kondo, J. and H. Yamazawa. 1986. Aerodynamic roughness over an inhomogeneous ground surface. Boundary-Layer Meteorology. 35: 331-348.

- Letchford C., A. Gardner, R. Howard and J. Schroeder. 2001. A comparison of wind prediction models for transitional flow regimes using full-scale hurricane data. J. Wind Eng. Ind. Aerodyn. 89: 925-945.

- Lettau, H. 1969. Note on aerodynamic roughness-parameter estimation on the basis of roughness-element description. J. Applied Meteorology. 8: 828-832.

- MacDonald, R.W. 2000. Modeling the mean velocity profile in the urban canopy layer. Boundary-Layer Meteorology. 97: 25-45.

- Macdonald, R.W., R.F. Griffiths and D.J. Hall. 1998. An improved method for estimation of surface roughness of obstacle arrays. Atmos. Environ. 32: 1857-1864.

- Mason, P.J. 1988. The formation of areally-averaged roughness lengths. Quart. J. R. Met. Soc. 114: 399-420.

- National Research Council of Canada (NRCC). 1996. User's guide – NBCC 1995 structural commentaries. National Research Council of Canada.

- Panofsky, H.A., D. Larko, R. Lipschutz, G. Stone, E.F. Bradley, A.J. Bowen and J. Højstrup. 1982. Spectra of velocity components over complex terrain. Quart. J. R. Met. Soc. 108: 215-230.

- Patankar, S.V. 1980. Numerical heat transfer and fluid flow. Washington: Hemisphere Pub. Corp.; New York: McGraw-Hill.

- Petersen, R.L. 1997. A wind tunnel evaluation of methods for estimating surface roughness length at industrial facilities. J. Atmospheric Environment. 31(No. 1): 45-57.

- Raupach, M.R., R.A. Antonia and S. Rajagopalan. 1991. Rough-wall turbulent boundary layers. J. Appl. Mech Rev. 44 (No. 1): 1-25.

- Richards, P.J., R.P. Hoxey and J.L. Short. 2000. Spectral models for the neutral atmospheric surface layer. J. Wind Eng. Ind. Aerodyn. 87: 167-185.

- Schmid, H.P. and B. Bunzli. 1995. The influence of surface texture on the effective roughness length. Quart. J. R. Met. Soc. 121: 1-21.

- Schroeder, J.L., D.A. Smith and R.E. Peterson. 1998. Variation of turbulence intensity and integral scales during the passage of a hurricane. J. Wind Eng. Ind. Aerodyn. 77-78: 65-72.

- Sill, B.L. and C. Fang. 1990. Effect of upstream roughness element distribution on wind loads on low rise structures. J. Wind Eng. Ind. Aerodyn. 36: 1289-1297.

- Simiu, E. and R.H. Scanlan. 1996. Wind effects on structures – Fundamentals and applications to design (3rd. Ed.). John Wiley. New York.

- Sitheeq, M.M., A.K.S. Iyengar and C. Farell. 1997. Effect of turbulence and its scales on the pressure field on the surface of a three-dimensional square prism. J. Wind Eng. Ind. Aerodyn. 69-71: 461-171.

- Smith, S.W. 1997. The Scientist and Engineer's Guide to Digital Signal Processing. California Technical Publishing.

- Standards Australia. 2002. AS/NZS 1170.2:2002 - Australian/New Zealand Standard, Structural design actions, Part 2: Wind actions. Standards Australia.

- Stathopoulos, T. 1979. Turbulent wind action on low rise buildings. Ph.D. Thesis. The University of Western Ontario, Canada.

- Stathopoulos, T. 1984. Design and fabrication of a wind tunnel for building aerodynamics. J. Wind Eng. Ind. Aerodyn. 16: 361-376.

- Stathopoulos, T. and P. Saathoff. 1994. Codification of wind-pressure coefficients for multispan gable roofs. J. Wind Eng. Ind. Aerodyn. 120: 2495-2519.

- Stathopoulos, T., K. Wang and H. Wu. 1999. Wind standard provisions for low building gable roofs revisited. Wind Engineering into the 21st Century - Proceedings of the 10th International Conference on Wind Engineering. Copenhagen, Denmark. June 21 – 24, 1999.

- Stathopoulos, T., K. Wang and H. Wu. 2000. Proposed new Canadian wind provisions for the design of gable roofs. Canadian Journal of Civil Engineering. 27: 1059 – 1072.

- Stathopoulos, T., K. Wang and H. Wu. 2001. Wind pressure provisions for gable roofs of intermediate roof slope. International Journal of Wind & Structures. 4: 119-130.

- Suresh Kumar, K. 1998. Simulation of fluctuating wind pressures on low building roofs. Ph.D. thesis. Concordia University, Canada.

- Surry, D., and D. Djakovich. 1995. Fluctuating pressures on models of tall buildings. J. Wind Eng. Ind. Aerodyn. 58: 81-112.

- Tamura, Y., K. Suda, A. Sasaki, Y. Iwatani, K. Fujii, R. Ishibashi and K. Hibi. 2001a. Simultaneous measurements of wind speed profiles at two sites using Doppler sodars. J. Wind Eng. Ind. Aerodyn. 89: 325-335.

- Tamura, Y., K. Suda, A. Sasaki, K. Miyashita, Y. Iwatani, T. Maruyama, K. Hibi and R. Ishibashi. 2001b. Simultaneous wind measurements over two sites using Doppler sodars. J. Wind Eng. Ind. Aerodyn. 89: 1647-1656.

- Taylor, P.A. 1969. On wind and shear stress profiles above a change in surface roughness. Quart. J. R. Met. Soc. 95: 71-91.

- Taylor, P.A. 1987. Comments and further analysis on effective roughness lengths for use in numerical three-dimensional models. Boundary-Layer Meteorology. 39:403-418.

- Tieleman, H.W. 1992. Problems associated with flow modeling procedures for low-rise structures. J. Wind Eng. Ind. Aerodyn. 41-44:923-934.

- Tieleman, H.W. 1996. Model/full scale comparison of pressures on the roof of the TTU experimental building. J. Wind Eng. Ind. Aerodyn. 65:133-142.

- Tieleman, H.W., D. Surry and J.X. Lin. 1994. Characteristics of mean and fluctuating pressure coefficients under corner (delta wing) vortices. J. Wind Eng. Ind. Aerodyn. 87:263-275.

- Tsutsumi, J., T. Katayama and M. Nishida. 1992. Wind tunnel tests of wind pressure on regularly aligned buildings. J. Wind Eng. Ind. Aerodyn. 41-44: 1799-1810.

- Uematsu, Y. and N. Isyumov. 1996. Wind pressures acting on the leading edge and corner regions of a low-rise building – a study of the CWC low-rise building data base. Report, The University of Western Ontario.

- Wang, K. and T. Stathopoulos. 2005a. Characterization of exposure for wind standards and codes of practice. 10th Americas Conference on Wind Engineering. Baton Rouge, Louisiana, USA. May 31-June 4, 2005.

- Wang, K. and T. Stathopoulos. 2005b. Exposure model for wind loading of buildings. 4th European-African Conference on Wind Engineering. Prague, Czech Republic. July 11-15, 2005.

- Wieringa, J. 1986. Roughness-dependent geographical interpolation of surface wind speed averages. Quart. J. R. Met. Soc. 112: 867-889.

- Wieringa, J. 1992. Updating the Davenport roughness classification. J. Wind Eng. Indus. Aerodyn., 41-44: 357-368.

- Wieringa, J. 1993. Representative roughness parameters for homogeneous terrain. Boundary-Layer Meteorology. 63: 323-363.

- Wiren, B.G. 1983. Effects of surrounding buildings on wind pressure distributions and ventilative heat losses for a single-family house. J. Wind Eng. Ind. Aerodyn. 15: 15-26.

- Wu, W. 1983. Fluid mechanics. Beijing University Publisher (in Chinese).

- Young, M.A. and B.J. Vickery. 1998. The influence of small open field on wind loads on low buildings. J. Wind Eng. Ind. Aerodyn. 77-78: 233-244.

- Zhang, X. and R.R. Zhang 2001. Actual ground-exposure determination and its influences in structural analysis and design. J. Wind Eng. Ind. Aerodyn. 89:973-985.

- Zhou, Y. and A. Kareem. 2002. Definition of wind profile in ASCE 7. J. Structural Engineering. 128 (No. 8): 1082-1086.

Appendix 1

A user's manual for the data-acquisition system DSM 3000

A1.1 Introduction

The DSM-3000 (DSM: Digital Service Module) is a pressure scanning computer. It incorporates a microprocessor, RAM memory, a hard disk drive, and other interface boards, accepts keyboard, mouse and monitor as peripheral devices, and uses Windows® 95 as an operating system. A DSM can accept pressure-inputs from up to eight ZOC-33 (ZOC: Zero, Operate, Calibrate) electronic pressure scanners. A host computer that is installed with DSMLinkC and Btel (Btel: Binary Telnet) programs can send commands to the DSM-3000 computer via Internet, and then receive the scanned data from DSM-3000 via Internet. ZOC-33 can scan up to 64 input pressure channels (Px channels) simultaneously.

A1.2 System setting and operating principle

Fig. A1.1 shows the diagram for installing the DSM-3000 system. A host computer can control the DSM computer via Internet, and the DSM computer talks to the ZOC-33 pressure scanner through local cable connection. At the same time, the DSM computer controls a device named DSM-CPM that can control the working mode of the ZOC-33 pressure scanner. Physically, DSM-CPM opens (and closes) its valves to conduit the 65 psi pneumatic pressure to two pistons in the ZOC-33 pressure scanner which dictates working mode of ZOC-33.

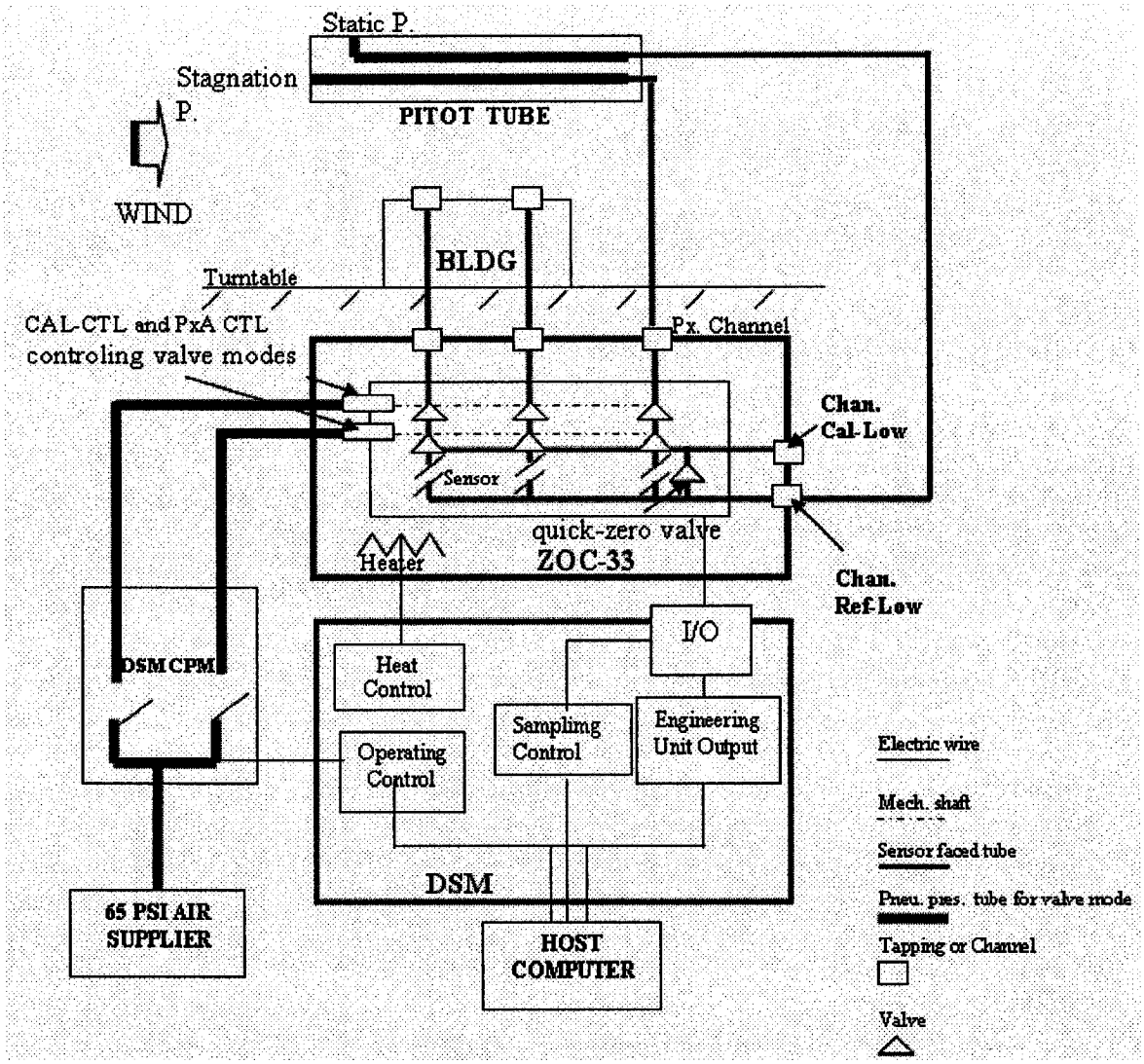

Fig. A1.1. DSM-3000 system diagram.

Fig. A1.2 shows the ZOC-33 system diagram. ZOC-33 incorporates integrated pneumatic valves that allow four working modes, namely, Purge, Calibrate, Operate and Leak-Test. These modes are controlled by two pistons respectively shown as the "Px CONTROL SOLENOID" and "CAL CONTROL SOLENOID" valves that are driven by the 65 psi pneumatic pressure as mentioned above. Fig. A1.3 shows these four modes.

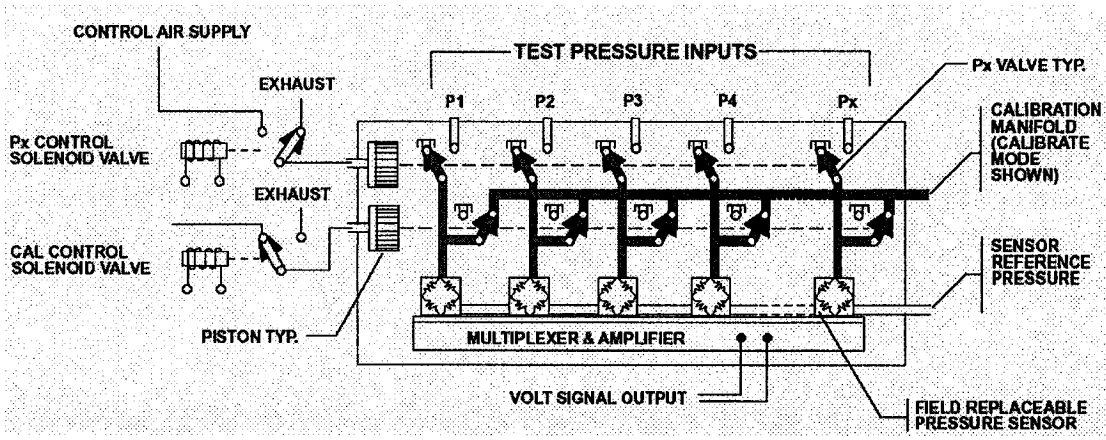

Fig. A1.2. ZOC-33 system diagram.

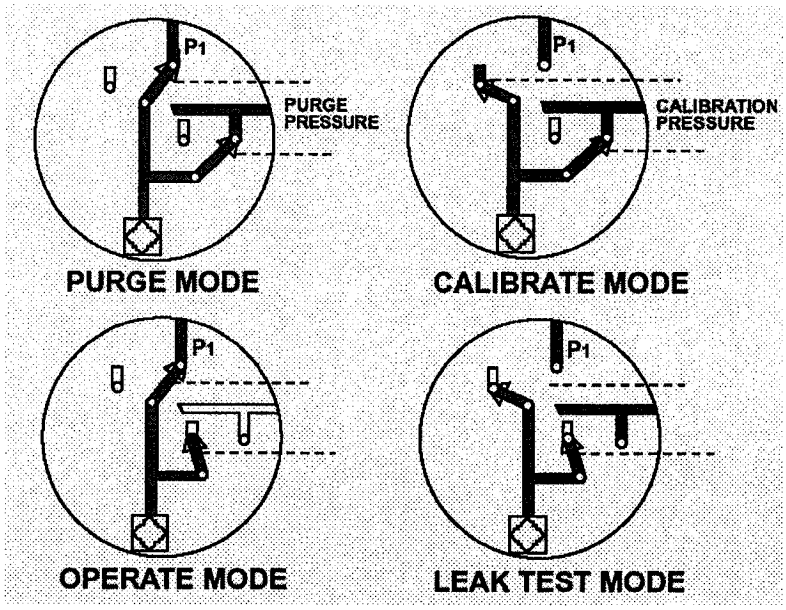

Fig. A1.3. ZOC-33 valve system and operating mode diagrams.

Purge mode

Purge mode is the default mode, and can be used to check if the system is under normal working condition. When system is under this mode, both CAL-CTR (Calibration

Control) and PxA-CTR ('A' stands for a product type) valves in the DSM-CPM are closed, i.e., the 65 psi pneumatic pressure is not supplied to push the pistons in ZOC-33.

In this mode, one side of the diaphragm of a sensor of ZOC-33 is not only open to a pressure tapping on the building model, but open also to the ambient pressure through the channel Cal-Low, and another side of the sensor diaphragm is open to the channel Ref-Low that is connected to Pitot static pressure. In rest air, both sides of the sensor diaphragm are in fact open to the ambient pressure, thus the sensor diaphragm is flat. Correspondingly, data read should be about zero. Therefore, if in Purge mode data read are far from zero (called data drift), then a temporary or permanent sensor failure should have occurred.

Purge mode can be reached in one of the three ways: (a) the entire system is power off; (b) the 65 psi pneumatic control pressure supply is off; and (c) DSMLinkC is programmed as follows: Enter DSMLinkC | DSM | Digital | Command, check 'Digital-Command-1' off, and check 'Digital-Command 2' off, with all the rest initial setting unaltered.

Calibrate Mode

In Calibrate mode, a sensor diagram has one side open to the channel Cal-Low, and another side open to the channel Ref-Low. This mode can be reached by applying the 65 psi control pressure to the piston associated with the channel PxA-CTL. Calibrate mode is useful for system's accuracy-check to be described in detail shortly.

Operate mode

In this mode, a pressure sensor has one side open to pressure applied onto pressure tapping, and another side open to Pitot static pressure via channel Ref-Low. This mode is the wind tunnel working mode.

Leak Test Mode

In this mode, both sides of the sensor diaphragm are disconnected from the outside environment. This mode can be reached by applying the 65 psi air pressure onto both valve-driving pistons. This mode can protect sensors in harsh field test.

Zero Calibrate (CALZ) mode

In addition to the four basic modes, there is a special mode, CALZ mode, for zeroing off the error caused by the diaphragm that has not been so flat as it was made in factory. In an article written by Scanivalve engineer C. Matthews, it is said, "*Each digital sensor array has an additional valve, referred to as the quick-zero valve. When commanded, this valve switches the calibration manifold to the reference manifold so that the zero offsets can be measured. This offset is then used to make a quick correction to the data.*"

In order to better understand CALZ, it is helpful to know how a sensor works. In ideal situation, a sensor can be considered as having a diaphragm absolutely flat. When a pressure is applied onto the diaphragm, it bends with its electronic resistance changing linearly with its curvature, which is sensed as volt change. The linear relationship between a pressure and a voltage signal is formulated into look-up table in factory; thus reading a voltage, the system can find an actual pressure. In real world, sensor may have

a slight bend. CALZ cuts off the error from a test data reading. The cut-off is illustrated in the following diagram.

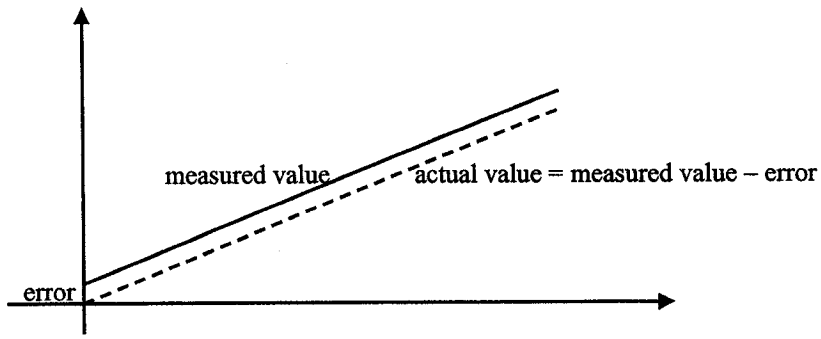

A1.3 Operation

General procedure

I) Set-up

a) Power on DSM-3000 and wait for 6+ hours for the ZOC-33 to warm up until the chamber temperature stays around 45°C. Switch on the compressed-air cylinder to supply the 65 psi pneumatic control pressure.

b) Run DsmLinkC on the host computer. Keep its initial settings unaltered, enter the following parameters:

DSM | Digital | settings: check Digital Output 1 for Out Pwr Up;

DSM | Digital | settings: check Digital Output 2 for Out CalZ;

DSM | Profile | Settings: enter the serial number of a ZOC-33 to a slot of Module-Position serial-Number;

DSM | Issue Commands: Enter "set bin 0".

c) Check DSM | Scan | Settings, and specify the scan settings.

The following settings are used in this study:

Scan Group 1: enabled;
Ports 1 through 64 for Mod1: checked;
Period-In-Microsecond = 62 μs;
Average = 1;
Frame-Per-Scan = 13500;
where 'Scan-Group' controls ZOC-33 channels/sensors (it should be noted that DSM-3000 scans all 64 channels of one ZOC-33 module before scanning another ZOC-33); Periods-in-Microseconds, which stands for the time interval between scanning two adjacent channels for scan frequency control, is set at 1000000μs/(amount of ZOC-33 modules × 64 channels × design scan frequency); 'Frame-Per-Scan' controls scan duration; 'Average' controls how many frames of scan are read and averaged before output. These settings correspond to (a) frequency per channel per scan = 250 Hz (1 sec /(duration of 1 frame of scan) = 1000000μs/(64 channels × 62μs/channel) ≈250 times), (b) total scanning duration = 54 seconds (= 250 Hz × 54 seconds).

d) Activate CALZ. Then system with unit as Pound-Square-Inch (PSI) should report data with 4-digit zeros after the decimal point.

II) Operate

A test may follow one of three testing procedures. Scan procedure 1 is useful for quick test that does not require scan frequency higher than 110 Hz. Scan procedure 2 can be used for formal test that requires scan frequency as high as 350 Hz. As a special procedure, Scan procedure 3 is useful for system accuracy-check.

III) Wrap-up

Click DSM | Purge. Turn off the 65 psi pneumatic control pressure after any test is done. Power off the entire DSM-3000 system after an experiment session is done.

<u>Scan procedure 1 (Quick test)</u>

a) Activate File | Open data log file by specifying file directory and name.

b) Click Scan (The scan process can be monitored with View Scan | Scan Group *N* on.)

c) After data scan is done, save data by File | Close data log file.

Scan procedure 2 (Formal test)

a) Go to DSM | Issue-Commands; enter "set bin 0" (This is to disable binary data transmission and enable ASCII data transmission).

b) Do CALZ, viewing data display on-line in a test-scan.

c) Go to DSM | Issue Commands; enter "set bin 1" (thus system receives binary input).

d) Disconnect DSMLinkC.

e) Open wind tunnel fan and rotate turntable to a designated azimuth.

f) If necessary, adjust parameters under DSMLinkC | DSM | settings | scan group setting.

g) Operate Btel to scan, save and convert measurements. During the first time using Btel, specify Btel parameters (the following data in *italic* are used in this study).

Local>list

Local>set DSM *64 (64 channels)*

Local>set numframes *13500 (13500 frames per scan)*

Local>set brcv *13500 (13500 frames per scan)*

Local>save

Local>blog ↵ (allocate a memory area to temporarily store the data scanned)

Local>open ↵ (connect Btel to DSM-3000 by Internet)

>scan ↵

"Ctrl+]" (return to local mode)

Local>cblog (write the data scanned into the hard disk storage)

Local>cvt (convert the binary data file into ASCII data file)

Local>quit

h) Qualify data, transfer, and rename data file. Data qualification can be made by comparison with previous results or by checking symmetry of data measured at taps symmetrical to wind direction.

Scan procedure 3 (Accuracy check)

a) Set up the U-tube manometer available in Center for Building Studies at Concordia University. Switch on the power of the U-tube manometer. Adjust the level-bolts to flatten the manometer. Open the valves of two ends of the U-tube to the ambient pressure. Zero the yard-stick, and contact the probe to the surface of the liquid inside the U-tube, which forms an electrical circuit at the moment.

b) Connect the device for positive (negative) pressure measurement. Connect one end of a three-way manifold tube to a Syringe, another end to the left (right) valve of the U-tube, the third end to the ZOC-33's Channel Cal-Low. Rotate the length-measurement bolt to lift the probe to a designated height.

c) Open DSMLinkC. Set a scan group with the following parameter values. Periods-In-Microseconds = 500, Average = 8, Frame-Per-Scan =1. Set into Calibrate mode. It can be achieved by entering DSM | Digital | Settings: Click on Digital-Output-1 for Out-Pwr-Up, Digital-Ouput-2 for Out-CalZ, and then, DSM | Digital | Command: Check off Digital-Output-1, and check on Digital-Ouput-2.

d) Calibrate. Use a Syringe to apply a known pressure to the channel Cal-Low; in Purge mode, this pressure is scanned by all Px channels. After a set of known pressures are measured, the sensor reading accuracy can be checked.

e) Resume Operate mode. Enter DSM | Digital | Command, and click on "Digital Output 1", and click off Digital Ouput 2.

A1.4 Trouble shooting

Preventing trapped air

Sensor diaphragm can be bended by the pressure of the air trapped inside the sensor chamber which cannot find a way out. Trapped air usually occurs after wind tunnel test, mostly for very thin tubes or very tight tube restrictors being employed. Trapped air may also occur when CALZ is mistakenly executed when wind tunnel fan is running.

Trapped air can find a way out of the system, if the ZOC-33 is in the Purge mode.

Preventing condensation

Air moisture may condense into the testing tubes when a huge temperature drop occurs (usually in Winter), and migrate to reach sensor diaphragm. It will damage sensor.

Two approaches may be used to prevent moisture. One way is to keep the power of DSM always on during an experiment so that the ZOC-33 chamber temperature stays around 45°C thus usually condensation cannot occur. Another way is to build a U-shape "service loop" that levitates ZOC-33 as high as possible, and sets the lower tip of the U-shape lower than the level where a ZOC-33 stays. In this way, the possible condensed moisture should stay in the "service loop" but cannot migrate uphill.

If condensation occurs, power off the system and disconnect the ZOC-33 from cable and model. Install another connector onto the ZOC-33. Purge nitrogen with total pressure

Appendix 2 A spectral analysis MATLAB program

The following source code is the implementation of the Discrete Fourier Transform concept (cf. Smith 1997) and the Fast Fourier Transform technique (using the MATLAB® built-in algorithm), for calculating a spectral density function of a given wind velocity time history for this study. The resultant spectral density function is then used to curve-fit the Von Karman equation (Simiu and Scanlan 1996) to get the present wind tunnel longitudinal scale of turbulence L_u^x that is used to determine the present wind tunnel geometrical scale (see Chapter 3).

```
X=dlmread('c:\V038.txt','\n');
u_mean=mean(X);
u_stdev=std(X);
sampleLength = 512;
NumberOfSegments = length(X)/sampleLength;
segment = zeros(sampleLength,1);
nfft = sampleLength;
Fs = 1000;
window = hann(sampleLength);
psd_collection =zeros (NumberOfSegments,(sampleLength/2+1))
for n= 1: NumberOfSegments
   segment = (X((n-1)*sampleLength+1:n*sampleLength));
   [psd, f] =  periodogram(segment, [], nfft, Fs);
   psd_collection(n,:)=psd';
end
temp_avg_psd =mean(psd_collection);
avg_psd = temp_avg_psd';
loglog(f/u_mean,f.*avg_psd/(u_stdev*u_stdev));
dlmwrite('c:\f.txt',f,'/n');
dlmwrite('c:\normalizedSpectrum.txt',f.*avg_psd/(u_stdev*u_stdev)
,'/n')
```

Appendix 3 Additional pressure coefficient conversion factors

As introduced in Chapter 3, the conversion between Cp and Cp' for one case obeys the following equation,

$$\Delta p = 0.5Cp'\rho U^2_{m-rf,localTerrain} = 0.5Cp\rho U^2_{m-rf,OC}$$

In this study, for Suburban terrain, $Cp'_{m-rf,suburban}$ is equal to $1.84\times Cp_{m-rf,OC}$, and for Urban terrain, $Cp'_{m-rf,urban}$ is equal to $2.26\times Cp_{m-rf,OC}$, i.e., the conversion coefficients are respectively equal to 1.84 and 2.26 for Suburban and Urban, both of which are respective to OC. This Appendix presents the conversion coefficients for a number of terrain cases respective to OC, which have been mentioned in Chapter 7.

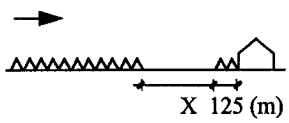

X (m)	0	125	250	375
Coeff.	1.84	1.69	1.61	1.57

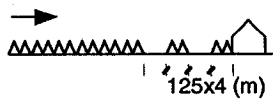

The above case's conversion coefficient = 1.87

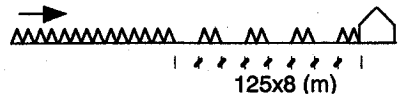

The above case's conversion coefficient = 1.49

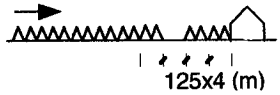

The above case's conversion coefficient = 1.8

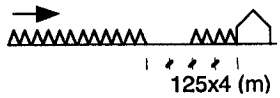

The above case's conversion coefficient = 1.8

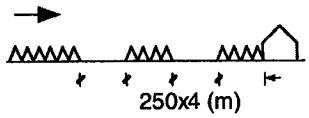

The above case's conversion coefficient = 1.61

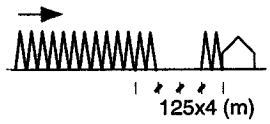

The above case's conversion coefficient = 2.0

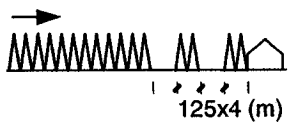

The above case's conversion coefficient = 2.2

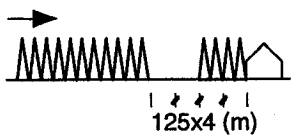

The above case's conversion coefficient = 2.2

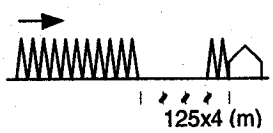

The above case's conversion coefficient = 2.0

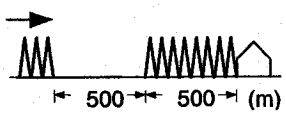

The above case's conversion coefficient = 2.0

Appendix 4 A VBA-ACAD-Word data mapping/plotting program

The following program, which is developed for this study and described herein, works in a automatic and mass-processing fashion, posting numerical and text data onto drawings of regular or irregular shapes. This program employs AutoCAD® 2002, Visual Basic® (VB) and Microsoft-Word® software, applying the Automation (including ActiveX control automation) technology. It uses VB to access and call the AutoCAD and Word class objects (their properties and methods) by virtue of the class objects' open structure and their supports on Standardization and Automation. Essentially, this program has database inquiry and graphic output functions.

In a greater detail, this program plots a standard AutoCAD drawing template, reads numerical data from data file and text from text file, then posts the data and text onto the AutoCAD drawing template. Afterwards, it copies the drawing bundle into Clipboard, and then calls Word objective functions to paste the drawing bundle from Clipboard to append to the end of the Word file. The above constitutes a complete cycle in a loop.

This program can be set up as follows. Go to AutoCAD | Tools | Macro | Visual Basic Editor | Insert | UserForm. Drag and drop a CommonButton onto UserForm and double-click the CommonButton. Go to Visual Basic Editor | Tools | References, Check Microsoft Word Object Library. If the following codes are poured in, then the program should be close to the stage of functioning.

```
Sub CommandButton1_Click()
    Const ForReading = 1, ForWriting = 2, ForAppending = 3
    Const TristateUseDefault = -2, TristateTrue = -1,
TristateFalse = 0

    Dim rfCpFilenamesFile As String
    Dim wlCpFilenamesFile As String
    Dim CaseNumbersFile As String
    Dim CasePlotFilenamesFile As String
    rfCpFilenamesFile = "H:\VBA-
ACAD\rfMostCriticalLocal_UTF_Filenames.txt"

    wlCpFilenamesFile = "H:\VBA-
ACAD\wlMostCriticalLocal_UTF_Filenames.txt"

    CaseNumbersFile = "H:\VBA-ACAD\caseNames.txt"
    CasePlotFilenamesFile = "H:\VBA-ACAD\casePlotFilenames.txt"

    Dim RfCpFilenamesFileAccess, RfCpFilenamesFileObj
    Dim WlCpFilenamesFileAccess, WlCpFilenamesFileObj
    Dim caseNumbersFileAccess, caseNumbersFileObj
    Dim caseDWGFileAccess, caseDWGFileObj

    Set RfCpFilenamesFileAccess =
CreateObject("Scripting.FileSystemObject")
    Set RfCpFilenamesFileObj =
RfCpFilenamesFileAccess.GetFile(rfCpFilenamesFile)
    Set RfCpFilenamesFileReader =
RfCpFilenamesFileObj.OpenAsTextStream(ForReading,
TristateUseDefault)
    Set WlCpFilenamesFileAccess =
CreateObject("Scripting.FileSystemObject")
    Set WlCpFilenamesFileObj =
WlCpFilenamesFileAccess.GetFile(wlCpFilenamesFile)
    Set WlCpFilenamesFileReader =
WlCpFilenamesFileObj.OpenAsTextStream(ForReading,
TristateUseDefault)
    Set caseNumbersFileAccess =
CreateObject("Scripting.FileSystemObject")
    Set caseNumbersFileObj =
caseNumbersFileAccess.GetFile(CaseNumbersFile)
    Set caseNumberReader =
caseNumbersFileObj.OpenAsTextStream(ForReading,
TristateUseDefault)
    Set caseDWGFileAccess =
CreateObject("Scripting.FileSystemObject")
    Set caseDWGFileObj =
caseDWGFileAccess.GetFile(CasePlotFilenamesFile)
    Set caseDWGFileReader =
caseDWGFileObj.OpenAsTextStream(ForReading, TristateUseDefault)

    Dim RfCpFileAccess, RfCpFileObj
    Dim WlCpFileAccess, WlCpFileObj
    Dim textObj As AcadText
    Dim textString As String
    Dim midString As String
    Dim insertionPoint(0 To 2) As Double
    Dim height As Double
```

```
    height = 2.4

    For x = 1 To 66
    ThisDrawing.Application.Documents.Open ("H:\VBA-
ACAD\template4Merged_MostCritical.dwg")
    Dim textStyle1 As AcadTextStyle
    Dim newFontFile As String

    Set textStyle1 = ThisDrawing.ActiveTextStyle

    newFontFile = "C:\Program Files\AutoCAD
2002\Fonts\romand.shx"

    textStyle1.fontFile = newFontFile

    RfCpFilename = RfCpFilenamesFileReader.ReadLine

    Set RfCpFileAccess =
CreateObject("Scripting.FileSystemObject")
    Set RfCpFileObj = RfCpFileAccess.GetFile(RfCpFilename)
    Set RfCpFileReader = RfCpFileObj.OpenAsTextStream(ForReading,
TristateUseDefault)
    'Roof Merged Tap 1

    textString = RfCpFileReader.ReadLine
    midString = Mid(textString, 7, 5)
    insertionPoint(0) = 75: insertionPoint(1) = 31:
insertionPoint(2) = 0

    Set textObj = ThisDrawing.ModelSpace.AddText(midString,
insertionPoint, height)
    (Note: the rest statements with respect to the rest roof taps
are ignored)
    WlCpFilename = WlCpFilenamesFileReader.ReadLine

    Set WlCpFileAccess =
CreateObject("Scripting.FileSystemObject")
    Set WlCpFileObj = WlCpFileAccess.GetFile(WlCpFilename)
    Set WlCpFileReader = WlCpFileObj.OpenAsTextStream(ForReading,
TristateUseDefault)

    'Wall Merged Tap 1
    textString = WlCpFileReader.ReadLine
    midString = Mid(textString, 7, 5)
    insertionPoint(0) = 75: insertionPoint(1) = 4:
insertionPoint(2) = 0

    Set textObj = ThisDrawing.ModelSpace.AddText(midString,
insertionPoint, height)
(Note: the rest statements with respect to the rest wall taps are
ignored)

    ZoomExtents

    ThisDrawing.Regen True
    ThisDrawing.SendCommand "copyclip" & vbCr
    ThisDrawing.SendCommand "all" & vbCr & vbCr
```

```
    Dim MyWord As Object
    Dim WordWasNotRunning As Boolean

    On Error Resume Next
    Set MyWord = GetObject(, "Word.Application")

    If Err.Number <> 0 Then WordWasNotRunning = True
    Err.Clear

    MyWord.Visible = True
    MyWord.Documents.Open "H:\VBA-ACAD\template.doc"
    MyWord.ShowClipboard

    Set Range2 = MyWord.Application.ActiveDocument.Content
    Range2.Collapse Direction:=wdCollapseEnd
    Range2.Paste
    Next x
End Sub
```

Appendix 5

The present numerical simulation C++ source code

The following is an exhibit of the source code of the numerical simulation described in Chapter 4. The source code with comments and explanations may be available upon request.

```
#include <iostream.h>
#include <fstream.h>
#include <stdlib.h>
#include <math.h>
#include <string.h>
#include <iomanip.h>

struct patch{  //to store patch geometric information
      int length;
      int steps;
      double zo;
      double u_star;
      int stepsInWallRegion;
};

int originizeZ(int verticalLevels, double Z[]);
int originizing_Velocities(int verticalLevels, double Z[], double
U_Initial[], double W_Initial[], double zo, double u_star, double
UG_turntable);
int arrayCopying(int verticalLevels, double targetArray[], double
sourceArray[]);
int arrayPrinting(int verticalLevels, double array[]);
int arrayPrinting(int verticalLevels, int array[]);//function
overloading
int Z_Printing(int verticalLevels, double array[]);
int velocityPrinting(int verticalLevels, double array[], double
u_star);
int velocityScrPrinting(int verticalSteps, double array[]);
int localClassicProfilePrinting(int verticalLevels, double
array[],double zo, double u_star); //printing
int localCurrentProfilePrinting(double calculatedLength, int
verticalLevels, double U_OneRowOutput[]);
int FiniteVolumeMethod(int verticalLevels,
int patch_length,double patch_zo,double patch_u_star,
int patch_stepsInWallRegion,
double preceding_patch_zo,double preceding_patch_u_star,
double Z[],
double U_OneRowInput[], double W_OneRowInput[],
double U_OneRowOutput[], double W_OneRowOutput[],
double sigma1, double sigma2, double sigma3);
```

```
int TDMA(double delta_U[],double A[],double B[],double C[],double
D[],double P[],double Q[], double U_I [], double U_O[],double W_I
[], double W_O[],  double Z[], double patch_zo, double
patch_u_star, int patch_stepsInWallRegion, double
preceding_patch_zo, double preceding_patch_u_star,
double sigma1, double sigma2, double sigma3);
double differenceFinding(double U_I[], double delta_U[], double
temp_delta_U[]);

#define karman 0.4
#define delta_Z 2
#define verticalSteps 120
#define delta_X 0.01
#define calStepsForOutput 2500
#define mu 0.49
#define checkLevel 3
#define epsilon 0.00001
#define tempLength1 50
#define tempLength2 200
#define tempLength3 150

//================================================================
//main()
//================================================================

int main(){
      fstream fileCleaner;
      fileCleaner.open("output.txt",ios::trunc);
      fileCleaner.close();

      //=========================================================
      //Define the initial and boundary conditions
      //=========================================================
      patch patch[100]; //100 is the max number of patches
allowed

      for(int max=0;max<10;max++){
            patch[max].length=-1000;
      }

      patch[0].length=0.00; patch[0].zo=0.00;
      patch[0].u_star = 0.00;
      patch[0].steps=0.00;
      patch[1].length=1*500;
      patch[1].zo=0.42; patch[1].u_star = 2.13;
      patch[1].steps=patch[1].length/delta_X;
      patch[2].length=500;  patch[2].zo=0.024;
      patch[2].u_star = 1.52;
      patch[2].steps=patch[2].length/delta_X;
      patch[3].length=5.5*500;
      patch[3].zo=0.42; patch[3].u_star = 2.13;
      patch[3].steps=patch[3].length/delta_X;
      double UG_turntable = 35.94;//for suburban
      int totalPatchNumber;

      for(max=0; max<100; max++){
            if(patch[max].length<0){
                  totalPatchNumber=max-1;
```

```
                    break;
               }
          }

          for(int i=1; i<=totalPatchNumber; i++){
               patch[i].stepsInWallRegion = 1;
          }

          double sigma1 = 0.125;
          double sigma2 = 0.75;
          double sigma3 = 0.125;

          double Z[verticalSteps]={0};
          double U_patchInitial[verticalSteps]={0};
          double W_patchInitial[verticalSteps]={0};\

          originizeZ(verticalSteps, Z);
          originizing_Velocities(verticalSteps, Z, U_patchInitial,
W_patchInitial, patch[1].zo, patch[1].u_star, UG_turntable );

          double U_OneRowInput[verticalSteps]={0};
          double W_OneRowInput[verticalSteps]={0};
          double U_OneRowOutput[verticalSteps]={0};
          double W_OneRowOutput[verticalSteps]={0};

          int patchCount =0;
          int stepCount =0;
          double calculatedLength=0;

          Z_Printing(verticalSteps,Z);
          velocityPrinting(verticalSteps,U_patchInitial,patch[1].u_st
ar);

          //=========================================================
          // Calculate for a whole terrain
          // If not all patches have been calculated, continue
          //=========================================================
          for (patchCount=1; patchCount<=totalPatchNumber;
patchCount++){
               cout<<"This is calculating for Patch
"<<patchCount<<endl;
               arrayCopying(verticalSteps, U_OneRowInput,
U_patchInitial);
               arrayCopying(verticalSteps, W_OneRowInput,
W_patchInitial);

          //=========================================================
          //Calculate for a whole patch
          //=========================================================
               for (stepCount=0; stepCount<=patch[patchCount].steps;
stepCount++){
                    cout<<"\nThis is calculating for Grid
"<<stepCount+1<<endl;

          //=========================================================
          //Calculate for a grid
          //=========================================================
```

```
                        double
variable_u_star=patch[patchCount].u_star;
                    if
(patchCount>1&&patch[patchCount].zo>patch[patchCount-
1].zo&&2*pow((calculatedLength+1),-
0.1)*patch[patchCount].u_star>patch[patchCount].u_star)

      variable_u_star=2*pow((calculatedLength+1),-
0.1)*patch[patchCount].u_star;

      if(patchCount>1&&patch[patchCount].zo<patch[patchCount-
1].zo&&0.4*pow((calculatedLength+1),0.1)*patch[patchCount].u_star
<patch[patchCount].u_star)
                    {
      variable_u_star=0.4*pow((calculatedLength+1),0.1)*patch[pat
chCount].u_star;
                    }

                    FiniteVolumeMethod(verticalSteps,
                                patch[patchCount].length,
patch[patchCount].zo, variable_u_star,
      patch[patchCount].stepsInWallRegion,
      patch[patchCount-1].zo, patch[patchCount-1].u_star,
      Z,
      U_OneRowInput, W_OneRowInput,
      U_OneRowOutput, W_OneRowOutput,
      sigma1, sigma2, sigma3);

                    //For debug
                    if(stepCount%calStepsForOutput==0 || stepCount ==
patch[0].steps){
                          cout<<"Patch "<<patchCount<<" Step
"<<stepCount<<" Length\t"<<calculatedLength<<endl;
                          velocityScrPrinting(verticalSteps,
U_OneRowOutput);
                          cout<<"in comparison with the local patch's
classic profile\n";

                          localCurrentProfilePrinting
(calculatedLength, verticalSteps, U_OneRowOutput);
                          localClassicProfilePrinting (verticalSteps,
Z, patch[patchCount].zo, patch[patchCount].u_star);
                    }

                    arrayCopying(verticalSteps, U_OneRowInput,
U_OneRowOutput);
                    arrayCopying(verticalSteps, W_OneRowInput,
W_OneRowOutput);
                    calculatedLength=calculatedLength+delta_X;
              }

              arrayCopying(verticalSteps, U_patchInitial,
U_OneRowOutput);
              arrayCopying(verticalSteps, W_patchInitial,
W_OneRowOutput);
              calculatedLength=0;
      }
```

```
      cout<<"Program sucessfully ends. Press return to exit...";

      return 0;
}

//=================================================================
//FiniteVolumeMethod()
//=================================================================
      int FiniteVolumeMethod(int verticalLevels,
      int patch_length,double patch_zo, double patch_u_star,
      int patch_stepsInWallRegion,
      double preceding_patch_zo, double preceding_patch_u_star,
      double Z[],
      double U_Input[], double W_Input[],
      double U_Output[], double W_Output[],
      double sigma1, double sigma2, double sigma3){
      double stepSize=delta_X;
      double U_I[verticalSteps]={0};
      double W_I[verticalSteps]={0};
      double delta_U [verticalSteps]={0};
      double temp_delta_U [verticalSteps]={0};
      double U_O [verticalSteps]={0};
      double W_O [verticalSteps]={0};

      arrayCopying(verticalLevels, U_I, U_Input);
      arrayCopying(verticalLevels, temp_delta_U, U_Input);
      arrayCopying(verticalLevels, W_I, W_Input);

      //    U calculation
      double B[verticalSteps]={0};
      double C[verticalSteps]={0};
      double D[verticalSteps]={0};
      double P[verticalSteps]={0};
      double Q[verticalSteps]={0};
      int numberOfCalculation =0;

      while (differenceFinding (U_I, delta_U,
temp_delta_U)>epsilon){
            arrayCopying(verticalSteps, temp_delta_U, delta_U);
            numberOfCalculation++;

            //For debug
      cout<<"Solve linear equation system. Iteration No.
"<<numberOfCalculation<<endl;

      //TDMA to calculate delta
      U_i+1[j]

      TDMA(delta_U,A,B,C,D,P,Q,U_I,U_O, W_I, W_O, Z,
patch_zo,patch_u_star, patch_stepsInWallRegion,
preceding_patch_zo, preceding_patch_u_star,
                  sigma1, sigma2, sigma3);
      }

      W_O[0]=0;
      W_O[2]=W_O[0]-2/delta_X*
            (sigma1*(U_O[0]-U_I[0])+sigma2*(U_O[1]-
U_I[1])+sigma3*(U_O[2]-U_I[2]));
```

```
      W_O[1]=0.5*(W_O[0]+W_O[2]);

      for (int j=2; j<verticalSteps-1; j++){
            W_O[j+1]=W_O[j-1]-2/delta_X*
            (sigma1*(U_O[j-1]-U_I[j-1])+sigma2*(U_O[j]-
U_I[j])+sigma3*(U_O[j+1]-U_I[j+1]));
      }
      W_O[verticalSteps-1]=0;

      arrayCopying(verticalLevels, U_Output, U_O);
      arrayCopying(verticalLevels, W_Output, W_O);

      return 0;
}

//==========================differenceFinding()==================
double differenceFinding(double U_I[], double delta_U[], double
temp_delta_U[]){
      double diff=-10000000;
      int count=-100;
      double temp=0;

      for (int i=1; i<verticalSteps; i++){
            //find the largest value
            temp=fabs((temp_delta_U[i]-delta_U[i])/U_I[i]);
            if(diff<temp){
                  diff=temp;
                  count=i;
            }
      }

      cout<<"The normalized delta_U at check level "<<count<<" =
"<<diff*100<<"%, if<0.1%, convergence reaches...\n";

      return diff;
}

//==========================originizeZ()=========================
int originizeZ(int verticalLevels, double Z[]){
      for (int j=0; j<verticalLevels;j++){
            if(j==0)
                  Z[j]=0;
            else
                  Z[j]=Z[j-1]+delta_Z;
            cout<<Z[j]<<' ';
      }
      cout<<endl;

      return 0;
}

//==========================originizing_Velocities()=============
int originizing_Velocities(int verticalLevels, double Z[], double
U_Initial[], double W_Initial[], double zo, double u_star, double
UG_turntable){
      if (zo==0.024)
      {
            for (int j=80; j<=verticalSteps-1;j++){
```

```
                U_Initial[j]=UG_turntable*pow(Z[j]/360, 0.05);
                W_Initial[j]=0;
        }

        for (j=30; j<=80;j++){
                U_Initial[j]=U_Initial[80]*pow(Z[j]/160, 0.12);
                W_Initial[j]=0;
        }

        for (j=0; j<=30;j++){
                U_Initial[j]= U_Initial[30]*pow(Z[j]/60, 0.15);
                W_Initial[j]=0;
        }
    }
    else
    {
        for (int j=100; j<=verticalSteps-1;j++){
                U_Initial[j]=UG_turntable*pow(Z[j]/360, 0.05);
                W_Initial[j]=0;
        }
        for (j=0; j<=100;j++){
                U_Initial[j]= U_Initial[100]*pow(Z[j]/200, 0.25);
                W_Initial[j]=0;
        }
    }

    return 0;
}

//=========================arrayCopying()=======================
int arrayCopying(int verticalLevels, double targetArray[], double
array[]){
    for(int i=0;i<verticalLevels;i++){
        targetArray[i]=array[i];
    }

    return 0;
}

//=========================Z_Printing()=========================
int Z_Printing(int verticalLevels, double array[]){
    int k=999;
    ofstream fout;
    fout.open("output.txt", ios::out|ios::app);
    fout<<k<<'\t';

    for (int i=0;i<10; i++){
        fout<<array[i]<<'\t';
    }

    for (i=10;i<verticalLevels; i=i+5){
        fout<<array[i]<<'\t';
    }

    fout<<array[verticalLevels-1]<<'\t';
    fout<<endl;
    fout.close();
```

```
	return 0;
}

//=========================velocityPrinting()==================
int velocityPrinting(int verticalLevels, double array[], double
u_star){
	int k=999;
	ofstream fout;
	fout<<k<<'\t';
	fout.open("output.txt", ios::out|ios::app);

	for (int j=0; j<10; j++){
		fout<<array[j]*u_star<<'\t';
	}

	for (j=10; j<verticalLevels; j=j+5){
		fout<<array[j]*u_star<<'\t';
	}

	fout<<array[verticalLevels-1]*u_star<<'\t';
	fout<<endl;

	fout.close();

	return 0;
}

//=========================velocityScrPrinting()================
int velocityScrPrinting(int verticalLevels, double array[]){
	cout<<array[1]
		<<'\t'<<array[3]
		<<'\t'<<array[5]
		<<'\t'<<array[10]
		<<'\t'<<array[50]
		<<'\t'<<array[verticalLevels-10]
		<<'\t'<<array[verticalLevels-1]<<endl;

	return 0;
}

//=========================localClassicProfilePrinting()========
int localClassicProfilePrinting(int verticalLevels, double
array[],double zo, double u_star){
	ofstream fout;

	fout.open("output.txt", ios::out|ios::app);
	double outArray[verticalSteps];
	int k = 000;

	fout<<k<<'\t';

	for (int j=0; j<10; j++){
		outArray[j]=u_star/karman*log((array[j]+zo)/zo);
		fout<<outArray[j]<<'\t';
	}

	for (j=10; j<verticalLevels; j=j+5){
		outArray[j]=u_star/karman*log((array[j]+zo)/zo);
```

```
            fout<<outArray[j]<<'\t';
      }

      outArray[verticalLevels-
1]=u_star/karman*log((array[verticalLevels-1]+zo)/zo);

      fout<<outArray[verticalLevels-1]<<'\t';
      cout<<endl;
      fout<<endl;
      cout<<outArray[1]
            <<'\t'<<outArray[3]
            <<'\t'<<outArray[5]
            <<'\t'<<outArray[10]
            <<'\t'<<outArray[50]
            <<'\t'<<outArray[verticalLevels-10]
            <<'\t'<<outArray[verticalLevels-1]<<endl;
      fout.close();

      return 0;
}

//=========================localCurrentProfilePrinting()========
int localCurrentProfilePrinting(double calculatedLength, int
verticalLevels, double U_OneRowOutput[]){
      ofstream fout;
      fout.open("output.txt", ios::out|ios::app);
            fout<<calculatedLength<<'\t';

      for (int j=0; j<10; j++){
            fout<<U_OneRowOutput[j]<<'\t';
      }
      for (j=10; j<verticalLevels; j=j+5){
            fout<<U_OneRowOutput[j]<<'\t';
      }
      fout<<U_OneRowOutput[verticalLevels-1]<<'\t';
      fout<<endl;
      fout.close();

      return 0;
}

//=========================TDMA()================================
int TDMA(double delta_U[],double A[],double B[],double C[],double
D[],double P[],double Q[],
                  double U_I [], double U_O[],double W_I [], double
                  W_O[],
                  double Z[],
                  double patch_zo, double patch_u_star,
                  int patch_stepsInWallRegion,
                  double preceding_patch_zo, double
                        preceding_patch_u_star,
                  double sigma1, double sigma2, double sigma3){

      for(int j=0; j<=patch_stepsInWallRegion;j++){
            delta_U[j]=0;
      U_I[j]=patch_u_star/karman*log((Z[j]+patch_zo)/patch_zo);
            W_I[j]=0;
      }
```

```
     for (j=patch_stepsInWallRegion+1; j<verticalSteps-1; j++){
          A[j]=sigma2*delta_Z*(delta_U[j]+2*U_I[j]);

          B[j]=-sigma3*delta_Z*(delta_U[j+1]+2*U_I[j+1]);

          C[j]=-sigma1*delta_Z*(delta_U[j-1]+2*U_I[j-1]);

          D[j]=-((1-mu)*delta_X*U_I[j+1]*W_I[j+1]+
                (2*mu-1)*delta_X*U_I[j]*W_I[j]-
               mu*delta_X*U_I[j-1]*W_I[j-1])
               +
               karman*karman*delta_X/(delta_Z*delta_Z)*
               (
     ((Z[j]+Z[j+1])/2)*((Z[j]+Z[j+1])/2)*(U_I[j+1]*U_I[j+1]-
2*U_I[j]*U_I[j+1]+U_I[j]*U_I[j])-
               ((Z[j-1]+Z[j])/2)*((Z[j-
1]+Z[j])/2)*(U_I[j]*U_I[j]-2*U_I[j]*U_I[j-1]+U_I[j-1]*U_I[j-1])
               );
          }

          P[patch_stepsInWallRegion+1]
               =
B[patch_stepsInWallRegion+1]/A[patch_stepsInWallRegion+1];

          Q[patch_stepsInWallRegion+1]
          =
D[patch_stepsInWallRegion+1]/A[patch_stepsInWallRegion+1];

        for (j=patch_stepsInWallRegion+1; j<=(verticalSteps-2);
j++){
               P[j]=B[j]/(A[j]-C[j]*P[j-1]);
               Q[j]=(D[j]+C[j]*Q[j-1])/(A[j]-C[j]*P[j-1]);
          }

          delta_U[verticalSteps-1]=0;
          delta_U[verticalSteps-2]=0;

          //Back-substitution
          for (j=(verticalSteps-
3);j>=patch_stepsInWallRegion+1;j--){
               delta_U[j]=P[j]*delta_U[j+1]+Q[j];
          }

     //   Calculate U upon delta_U
     U_O[0]=0;
     for (j=1; j<=verticalSteps-1; j++){
          U_O[j]=U_I[j]+delta_U[j];
     }
     return 0;
}
```

```
      for (j=patch_stepsInWallRegion+1; j<verticalSteps-1; j++){
            A[j]=sigma2*delta_Z*(delta_U[j]+2*U_I[j]);

            B[j]=-sigma3*delta_Z*(delta_U[j+1]+2*U_I[j+1]);

            C[j]=-sigma1*delta_Z*(delta_U[j-1]+2*U_I[j-1]);

            D[j]=-((1-mu)*delta_X*U_I[j+1]*W_I[j+1]+
                  (2*mu-1)*delta_X*U_I[j]*W_I[j]-
                  mu*delta_X*U_I[j-1]*W_I[j-1])
                  +
                  karman*karman*delta_X/(delta_Z*delta_Z)*
                  (
      ((Z[j]+Z[j+1])/2)*((Z[j]+Z[j+1])/2)*(U_I[j+1]*U_I[j+1]-
2*U_I[j]*U_I[j+1]+U_I[j]*U_I[j])-
                  ((Z[j-1]+Z[j])/2)*((Z[j-
1]+Z[j])/2)*(U_I[j]*U_I[j]-2*U_I[j]*U_I[j-1]+U_I[j-1]*U_I[j-1])
                  );
            }

            P[patch_stepsInWallRegion+1]
                  =
B[patch_stepsInWallRegion+1]/A[patch_stepsInWallRegion+1];

            Q[patch_stepsInWallRegion+1]
            =
D[patch_stepsInWallRegion+1]/A[patch_stepsInWallRegion+1];

          for (j=patch_stepsInWallRegion+1; j<=(verticalSteps-2);
j++){
                  P[j]=B[j]/(A[j]-C[j]*P[j-1]);
                  Q[j]=(D[j]+C[j]*Q[j-1])/(A[j]-C[j]*P[j-1]);
            }

            delta_U[verticalSteps-1]=0;
            delta_U[verticalSteps-2]=0;

            //Back-substitution
            for (j=(verticalSteps-
3);j>=patch_stepsInWallRegion+1;j--){
                  delta_U[j]=P[j]*delta_U[j+1]+Q[j];
            }

      //    Calculate U upon delta_U
      U_O[0]=0;
      for (j=1; j<=verticalSteps-1; j++){
            U_O[j]=U_I[j]+delta_U[j];
      }
      return 0;
}
```